Icarus 314 (2018) 400–433

Contents lists available at ScienceDirect

Icarus

journal homepage: www.elsevier.com/locate/icarus

Basins, fractures and volcanoes: Global cartography and topography of Pluto from New Horizons

Paul Michael Schenk[a,*], Ross A. Beyer[b,c], William B. McKinnon[d], Jeffrey M. Moore[b], John R. Spencer[e], Oliver L. White[b], Kelsi Singer[e], Francis Nimmo[f], Carver Thomason[f], Tod R. Lauer[g], Stuart Robbins[e], Orkan M. Umurhan[b], William M. Grundy[h], S. Alan Stern[e], Harold A. Weaver[i], Leslie A. Young[e], K. Ennico Smith[b], Cathy Olkin[e], the New Horizons Geology and Geophysics Investigation Team

[a] Lunar and Planetary Institute, 3600 Bay Area Blvd., Houston, TX 77058, USA
[b] NASA Ames Research Center, Moffett Field, CA, USA
[c] Sagan Center at the SETI Institute, Mountain View, CA, USA
[d] Department Earth and Planetary Sciences, Washington University, St. Louis, MO, USA
[e] Southwest Research Inst., 1050 Walnut St., Suite 300, Boulder, CO, USA
[f] University of California at Santa Cruz, Santa Cruz, CA, USA
[g] National Optical Astronomy Observatory, Tucson, AZ, USA
[h] Lowell Observatory, Flagstaff, AZ, USA
[i] Johns Hopkins University Applied Physics Laboratory, Laurel, MD, USA

ARTICLE INFO

Keywords:
Pluto
Topography
Icy satellite
Impact

ABSTRACT

The 2015 New Horizons flyby has produced the first high-resolution maps of morphology and topography of Pluto and Charon, the most distant objects so mapped. Global integrated mosaics of Pluto were produced using both LORRI framing camera and MVIC line scan camera data, showing the best resolution data obtained for all areas of the illuminated surface, ~78% of the body. A unique feature of the Pluto imaging data set is the observation of terrains illuminated only by light scattered from atmospheric haze, allowing us to map terrains in the southern hemisphere that would otherwise have been in darkness. MVIC 4-color data were combined with the panchromatic map to produce full color global maps. Digital elevation models (DEMs) over ~42% of Pluto were produced using combinations of MVIC hemispheric scans and LORRI mosaics, from which slopes at scales of ~1 km can be determined. Pluto can be divided into regions each with distinct topographic signatures, corresponding with major physiographic terrain types. Large areas of Pluto are comprised of low-relief moderately cratered plains units. Deeply pitted and glaciated plains east of Sputnik Planitia are elevated ~0.7 km. The most dominant topographic feature on Pluto is the 1200-by-2000-km wide depression enclosing the bright Sputnik Planitia ice sheet, the surface of which is 2.5-to-3.5 km deep (relative to the rim) and ~2 km deep relative to the mean radius. The partial ring of steep-sided massifs, several of which are more than 5 km high, along the western margins of Sputnik Planitia produce some of the locally highest and steepest relief on Pluto, with slopes of 40–50°. The second major topographic feature is a complex, eroded, ridge-trough system ~300–400 km wide and at least 3200 km long extending north-to-south along the 155° meridian. This enormous structure has several kilometers of relief. It may predate the large impact event forming the basin, though some post-Sputnik Planitia deformation is evident. The large depressed, partially walled plain, Hyecho Palus, lies due southwest of Sputnik Planitia. Near the center of Hyecho Palus lie the circular constructional edifices Wright and Piccard Montes. Wright Mons rises 4.5 km above these plains, with a central depression ~4.5 km deep, whereas Piccard Mons, best observed in haze-light, rises ~5.5 km above the plains but has a bowl-shaped central depression ~5.5 km below the plains for a total relief of up to 11 km, the greatest observed on Pluto. Both of these features are interpreted as constructional (volcanic?) in nature. Additional prominent topographic features include a 2–3 km high and ~600 km wide dome centered on the illuminated IAU pole and the amoeboidal plateaus of "bladed" terrains in the equatorial region, which rise 2–5 km above local terrains and are the highest standing geologic units on the encounter hemisphere. The mean elevations in the integrated DEM for the two radio occultation areas are consistent with the 5–6 km difference in elevation as determined independently by

* Corresponding author.
E-mail address: schenk@lpi.usra.edu (P.M. Schenk).

https://doi.org/10.1016/j.icarus.2018.06.008
Received 20 August 2017; Received in revised form 5 June 2018; Accepted 6 June 2018
Available online 11 June 2018
0019-1035/ © 2018 Elsevier Inc. All rights reserved.

the radio experiment, and a limb profile near the egress point confirms the presence of elevated bladed terrains in that area. Local relief of 3–5 km at massifs, troughs and pits supports conclusions that the icy shell of Pluto is relatively rigid. Numerous examples of topographic control of ice or frost deposition occur across Pluto, including the distinct coloration of the polar dome, the elevated terrains of eastern Tombaugh Regio, and along the ridge-trough system, where ridge tops and fossae rims are covered in different ices than at lower elevations. The topographic hypsogram of Pluto's encounter hemisphere is strongly bimodal due to the large Sputnik Planitia depression. Otherwise the topographic signature of Pluto is controlled by deviations from the otherwise dominant low plains, including elevated bladed terrain plateaus and the depressed volcanic province including Wright and Piccard Montes.

1. Introduction

The New Horizons spacecraft passed through the Pluto system on 14 July 2015, and executed a series of observations designed to map the surface morphology, color, and topography of both Pluto and its largest moon, Charon (Stern et al., 2015; Moore et al., 2016; Grundy et al., 2016). The acquired imaging data represent our first detailed mapping of large Kuiper Belt objects, which showed them to be geologically and morphologically complex worlds (Stern et al., 2015; Moore et al., 2016). Pluto's large moon, Charon, is comparable in size, density and composition to the 11 classical midsize satellites of Saturn and Uranus, and is discussed in a separate report (Schenk et al., 2018a). Volatile-rich Pluto, on the other hand, is comparable in size and density to Triton; both bodies are transitional between the smaller midsize icy moons and the larger ice-rich worlds of Ganymede, Callisto and Titan. Impact cratering and other geologic processes on these large icy bodies are influenced by higher surface gravity and higher heat budgets than typically observed on the midsize icy moons. Triton likely being a massively heated captured object (McKinnon, 1984), the New Horizons encounter data provide the first opportunity to examine the physical properties of large icy bodies in solar orbit, i.e., not embedded within a satellites system and influenced by a large primary body such as Neptune. Mapping of these two bodies (Figs. 1–3) presents unique challenges related to the required mapping strategy and the peculiarities of the two main mapping cameras and their image products. Here we describe the cartographic and topographic mapping data from New Horizons and the regional and global topographic characteristics of Pluto revealed by these maps.

2. Cartographic mapping

2.1. Global mapping coverage and base map production

The best mapping and stereo imaging of Pluto covered the illuminated anti-Charon hemisphere (Fig. 1), the hemisphere observed during closest approach on July 14, 2015. Due to the high encounter velocity ($\sim$14 km/s) and the slow rotation of the two bodies (6.4 days), imaging scale varied with longitude from $\sim$35 to 0.07 km/pixel (Fig. 2), while terrains south of − 38° were in darkness at the time of encounter. We define longitude and latitude on Pluto according to the right hand rule and follow the recommendations of Zangari (2015). Pluto's positive pole is defined by Archinal et al. (2011a,b) and points in the direction of the angular momentum vector. Pluto's prime or 0° meridian is the sub-Charon longitude. Informally, we refer to the positive pole direction as "north," and to the direction of increasing longitude as "east".

The cartographic and stereo imaging campaign was conducted by the Long-Range Reconnaissance Imager (LORRI, Cheng et al., 2008) and the Multi-spectral Visible Imaging Camera (MVIC) of the Ralph instrument (Reuter et al., 2008). During the final 12 h before closest approach, Pluto overfilled the LORRI image frame and mosaics were required. The last global framing-camera mosaic to cover the illuminated disk is a 20-frame mosaic (P_LORRI) at $\sim$0.85 km/pixel resolution. Due to time constraints near closest approach, all subsequent LORRI mosaics were more limited in scope and covered either the

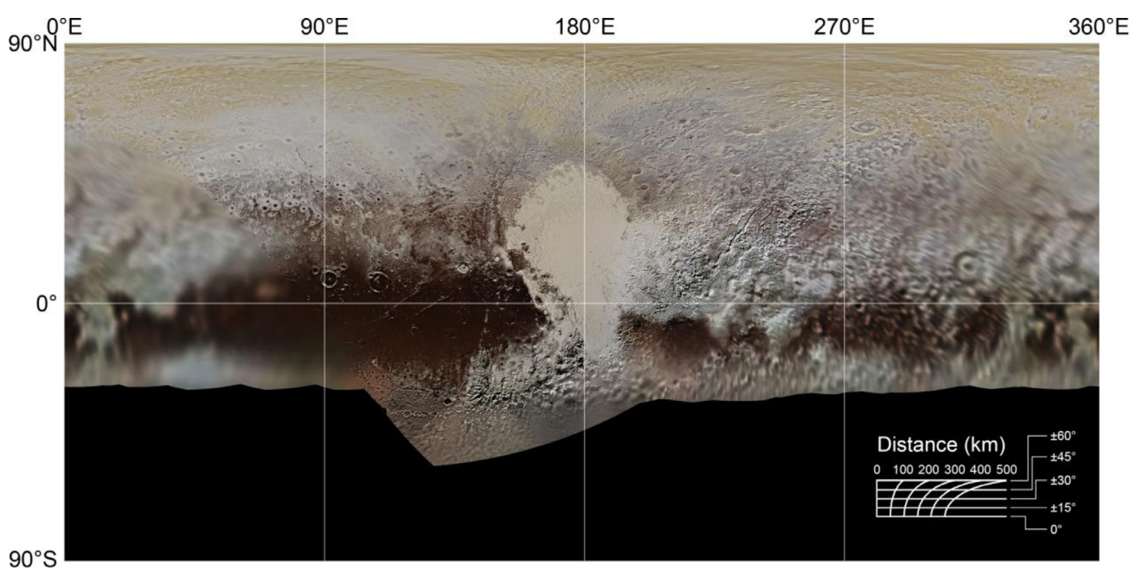

Fig. 1. Global image mosaic of Pluto produced at 300 m/pixel. Cylindrical map projection centered on 180° longitude. Black areas in all global map products were unilluminated during the 2015 encounter. The encounter hemisphere is in map center, with approach imaging to the left starting at $\sim$35 km/pixel resolution and increasing in quality to the west. Area extending downward from the general east-west boundary between the illuminated and unilluminated areas are those illuminated by light scattered by atmospheric haze, processed to have similar brightness properties as areas illuminated by sunlight. The online color version uses MVIC filters "blue", "red" and "CH_4," which provided the greatest color contrast. (For interpretation of the references to color in this figure legend, the reader is referred to the web version of this article.).

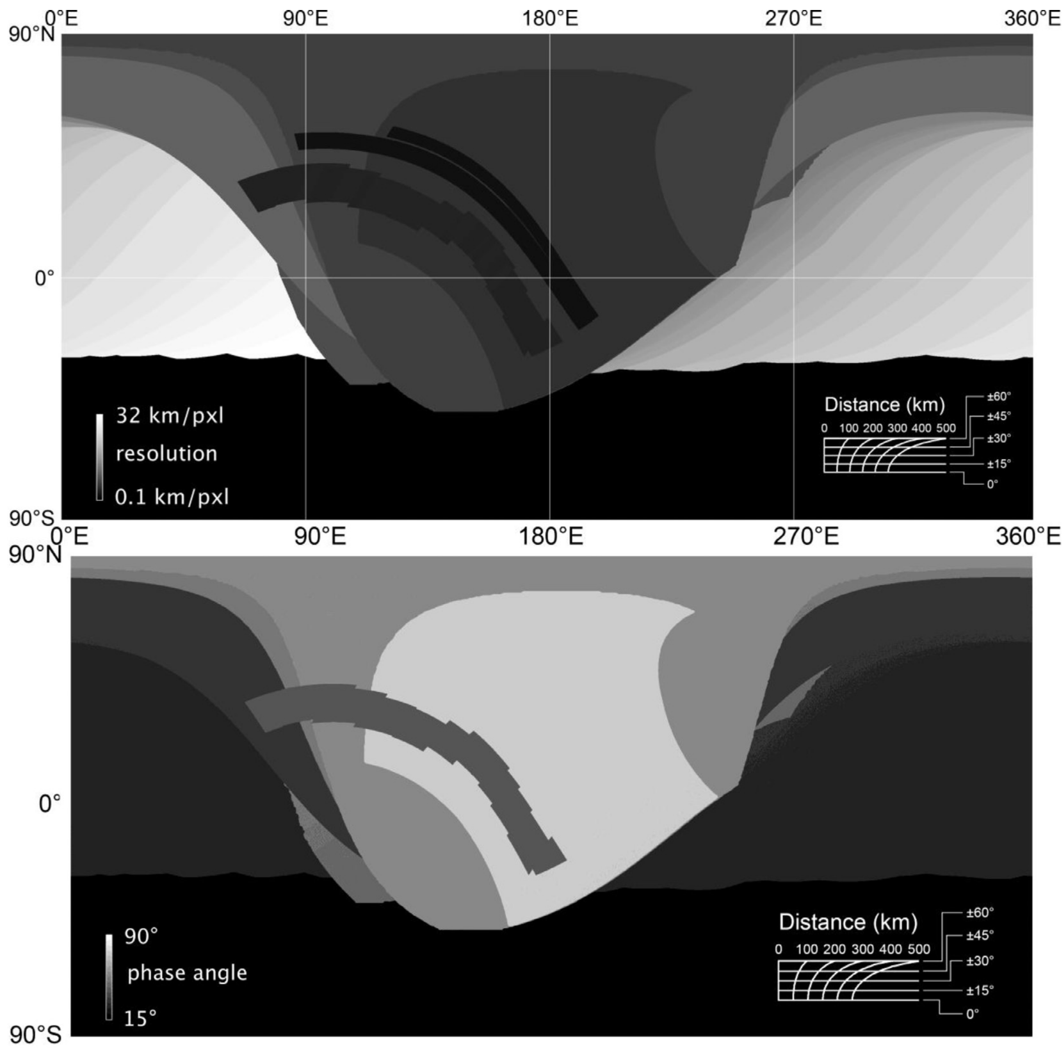

137

138

Fig. 2. Global cylindrical maps illustrating the pixel scale, phase angle, incidence angle, and emission angle. Maps are centered on 180°E longitude. Note that mappable regions illuminated by scattered light from haze are included.

center of the disk or three longitudinal strip mosaics, or "noodles" (P_LORRI_STEREO_MOSAIC, P_LEISA_HIRES, P_MPAN_1, P_MVIC_LORRI_CA).

The best imaging in 4 colors, with bands centered at 895, 870, 625 and 475 nm, was obtained on approach by MVIC were at pixel scales of ~0.65 km/pixel at phase angles of ~38°, with approach imaging at coarser resolutions and normally at lower phase angles. The last full-disc panchromatic MVIC scan was obtained at 0.45 km/pixel (P_MPAN1). The highest resolution scan was obtained at ~0.315 km/pixel (P_MVIC_LORRI_CA) but covered only two-thirds of the illuminated disk at ~70° phase angle.

An important characteristic of the Pluto encounter was that the phase angle remained essentially constant at ~15° until the final hours, facilitating production of a global map with generally uniform illumination quality (Fig. 1). During approach, LORRI imaging of Pluto (and Charon) was acquired every ~15° of longitude during the last Pluto rotation before encounter, thereby providing continuous longitudinal mapping at increasing resolution as the two bodies rotated under the approaching spacecraft (Fig. 2). In order to produce a global map with minimal distortion and best resolution at each point on the surface, all imaging data at emission angles > 75° (and > 70° for low resolution images) and all data at incidence angles > 88° (and > 85° for low resolution images) were ignored. The resulting global map product shows the illuminated surface of Pluto down to ~35°S.

Two resolved crescent images were acquired with MVIC over roughly two-thirds of the illuminated surface shortly after encounter. These were acquired at resolutions of 360 and 448 m pixel scales and phase angles of 151° and 161°, respectively. While important for investigating photometric properties and surface changes, the crescent images are not directly applicable to mapping as they do not add to the mapping coverage and feature extensive foreshortening of the illuminated surface. Additional high phase angle images were acquired later but are significantly lower in resolution and at higher phase angles and are not useful for mapping.

An unexpected bonus of the encounter was that scattering of light by atmospheric haze illuminated areas on Pluto otherwise in darkness (Fig. 3). This illumination permits mapping of haze-lit terrains in the three highest resolution MVIC scans at 0.650, 0.475 and 0.315 km/pixel resolutions and in stereo. Haze-illuminated imaging near longitude 150° extends down to – 56° latitude, the southernmost imaging obtained of Pluto, and extend useful imaging 200–250 km into what would have been dark regions at the time of closest approach on the encounter hemisphere. The northern half of the haze-lit areas covers areas seen in the base map but at higher resolution (Fig. 3). The southern half of the haze-lit zone observes terrains not illuminated by the Sun at all in 2015 and not otherwise observable by New Horizons (Figs. 1b and 3). Ridges on the surface of bladed terrain (see below), fractures, craters, and smooth glacier deposits are easily resolved

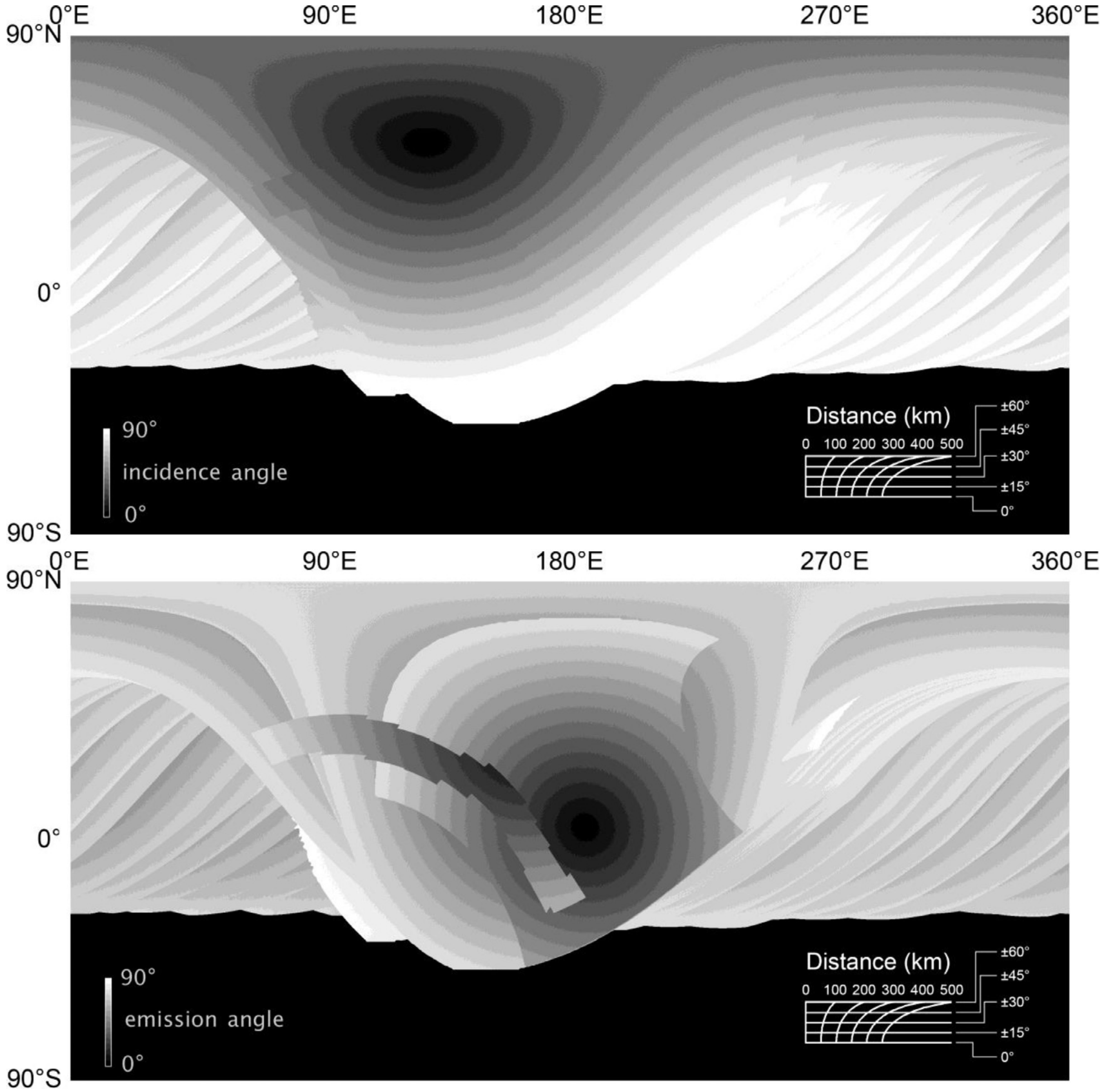

Fig. 2. (*continued*)

(Fig. 3), for example. However, the brightness of haze illuminated areas was $< 1\%$ that of solar illuminated terrains, and the dynamic range and signal-to-noise quality were significantly poorer than in the sun-lit regions. Some of these haze-lit features are also seen in LORRI images, but these images were at shorter exposures and the signal-to-noise quality in haze-illuminated areas is even poorer in LORRI data.

The global base map in Fig. 1 was assembled from individual map-projected geometrically and radio metrically calibrated monochromatic LORRI and 4-color MVIC images. Until a few hours before closest approach, the best images of any location on the surface were obtained by the LORRI framing camera at resolutions of 0.825 to 32 km/pixel. In the final few hours before encounter, however, the visible hemisphere was more completely covered in MVIC images, which could scan the visible disk more rapidly, and these provide the best resolutions over the majority of the encounter hemisphere.

To produce photo metrically uniform maps of the normal reflectance of the surface, wherein the brightness of different regions can be compared at least in a relative sense, a simplified photometric correction is applied to each image or mosaic to correct for emission and incidence angle variations across the surface (Fig. 2) before they are assembled into the global map (Fig. 1). We used the simplified combined lunar-Lambert Ian photometric function formulated by McEwen (1991) and encoded in the ISIS (Integrated Software for Imagers and Spectrometers; USGS, 2017) software, wherein the relative degree of lunar and Lambertian photometric qualities, L, is a function of phase angle. This empirical function is used here to produce maps of the approximate bidirectional reflectance maps of the surface of Pluto and Charon, normalized to common viewing conditions across the surface, in this case (Fig. 1), the approach phase angle of 15°. For Pluto, the optimal value of $L(15)$ was empirically derived (through comparisons of overlapping images) to be ~ 0.65. The lower resolution 4-color global mosaic was created separately using the same procedures and then merged with the panchromatic base map using the technique of McEwen and Soderblom (1984) to produce a global 4-color full-resolution map of Pluto (Fig. 1b).

Images used for mapping in the non-encounter hemisphere were obtained with LORRI. The LORRI point spread function has a full width at half maximum (FWHM) of ~ 2 pixels, which meets its specifications (Cheng et al., 2008), but can cause noticeable blurring. This can be improved through Lucy (1974)–Richardson (1972) deconvolution, and the images on this hemisphere were processed in this way in order to improve sharpness.

The default pixel scale of the Pluto base maps at the equator was chosen to be 300 m (based on the 0.315-km/pixel MVIC scans rather than the more spatially limited high-resolution LORRI noodles), and the projection chosen was simple cylindrical. The two highest-resolution

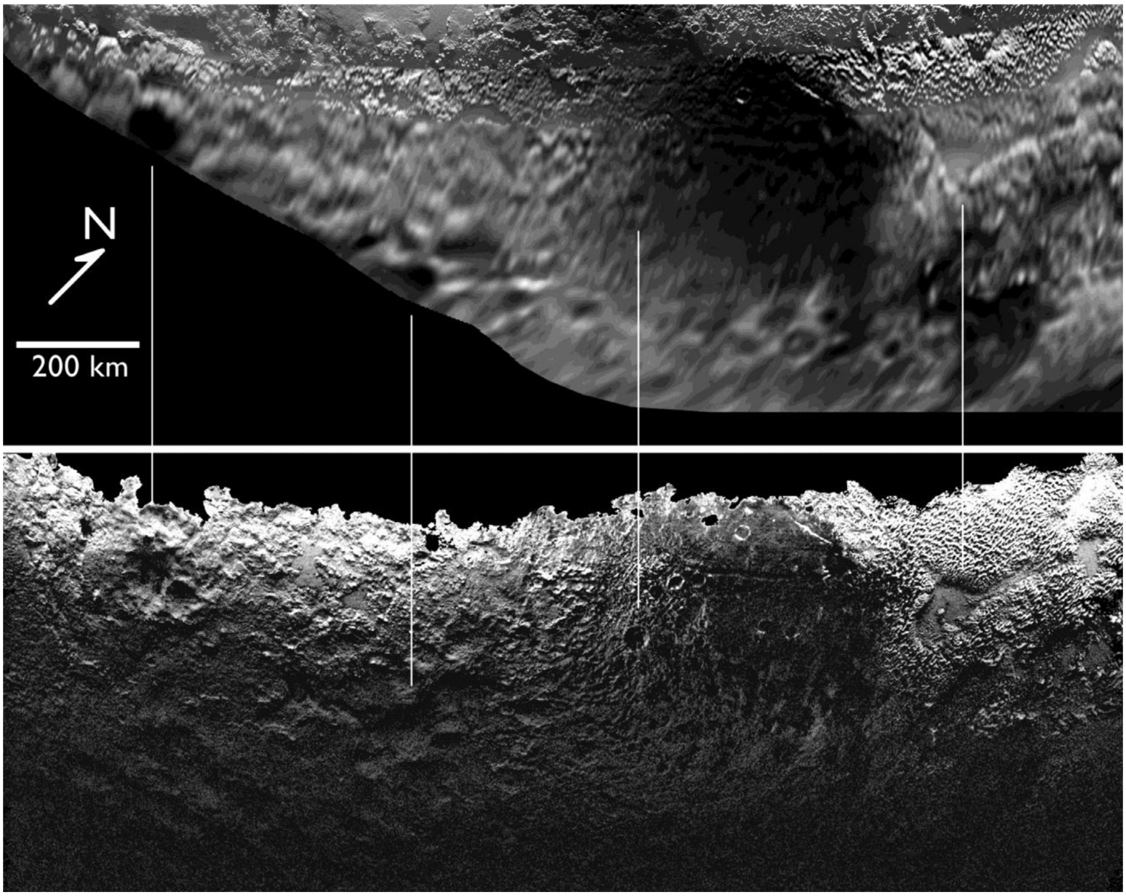

Fig. 3. A portion of the New Horizons mapping imaging illuminated by haze-scattered sunlight in MVIC images. Top view is from the LORRI mosaic illuminated by direct sunlight, the bottom the same region except using only the haze-illuminated portion of the highest resolution (315 m/pixel) MVIC imaging. Vertical lines highlight major features visible in both views. Observed brightness and contrast in the haze-lit region are several orders of magnitude poorer, requiring significant processing of those regions to present both in the same map. Region shown is centered on − 20°, 190°E just south of Sputnik Planitia. Visible in the haze-lit view are numerous irregular scarp-enclosed depressions of unknown origin and other irregular topography. These terrains are not characteristic of other regions on Pluto, suggesting that at least parts of the southern hemisphere have their own distinct geologic evolution.

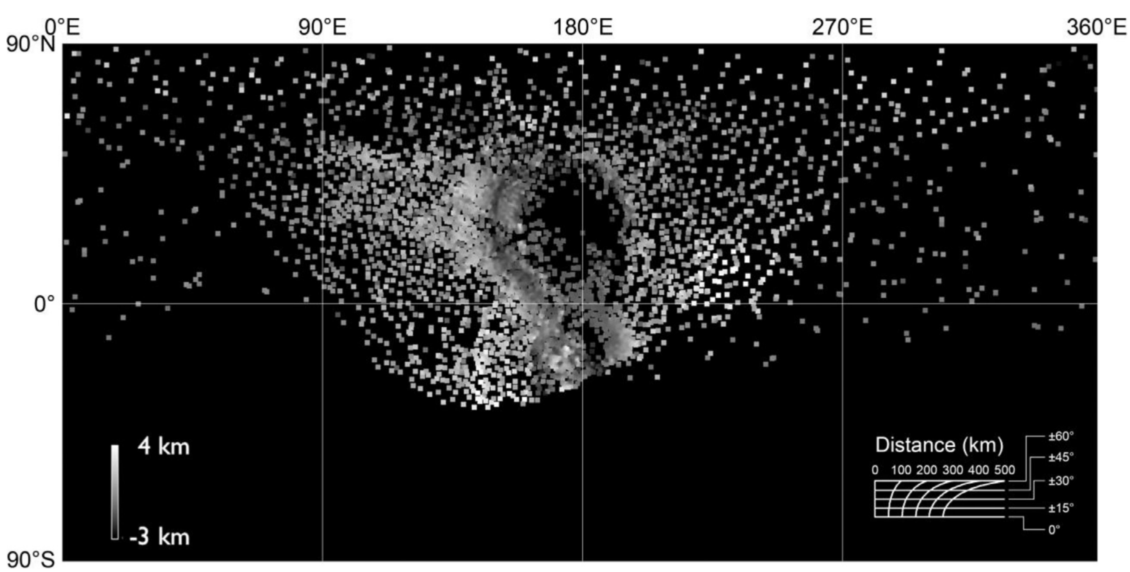

Fig. 4. Global cylindrical map of control points on Pluto, shaded to show elevation. The dense band of points arching across the map is the track of the high-resolution LORRI noodle mosaics that pan across Sputnik Planitia. The low density of points to left and right are in the low-resolution approach imaging areas.

LORRI image strips at 0.120–0.07 km/pixel were not included as they cover only a small fraction of the global map and would have resulted in an excessively large Pluto image file. With haze-lit imaging included, the global color and panchromatic maps from New Horizons (Figs. 1 and 2) cover ~78% of the surface of Pluto at inherent pixel scales of ~35 to 0.07 km, with better than 2-km pixel resolutions for ~50% of the surface that can be interpreted in a geologically meaningful way.

2.2. Control network for Pluto

To facilitate geologic investigation of the Pluto system and meet the mission objectives (Stern et al., 2008; Weaver et al., 2008), imaging strategies were designed to optimize cartographic and topographic mapping products for Pluto (Young et al., 2008; Beyer et al., 2013). Accurate positional referencing of surface features and derivations of topography from stereo images require precision knowledge of camera pointing and spacecraft position. Spacecraft position data were supplied by the New Horizons navigation team (https://naif.jpl.nasa.gov/pub/naif/pds/data/nh-j_p_ss-spice-6-v1.0/nhsp_1000/). Authors PS and RB updated camera pointing SPICE kernels for the entire New Horizons image library over the final Pluto 6-day rotation approach and encounter phase.

Cartographic control of the Pluto images utilized ISIS3 (USGS, 2017) software. The method requires selection of tie (or control) points linking all resolvable images at widely scattered points on the surface (Fig. 4), and then performing bundle adjustment (via the ISIS jigsaw program) to the camera pointing vectors for all images to minimize the differences in the computed surface coordinates. Images were reprojected to common map formats and blink compared to identify image misalignments. The tie-point solutions were reexamined and all points with high solution errors or low confidence are either corrected or deleted from the network. This process was repeated until the cartographic team was satisfied that all erroneous or poorly defined points are removed and all images were aligned.

Control point selection strategy was driven mostly by feature definition and the desire to have as widely dispersed a distribution of control points as practical given changes in feature resolutions and distortions near the edges of the visible disk. The first objective was to align images for georeferenced mosaic construction and second to produce registered stereo image pairs for DEM construction (see below). To preserve stereographic information between images, the camera pointing vector bundle adjustment was solved for both position and radius from planet center, otherwise the stereo parallax inherent in the image library would be distorted.

Existing ISIS software did not permit the use of framing camera images (LORRI) and line-scan (MVIC) images in the same bundle adjustment solution, and so we implemented a "two-solution" control network strategy. The vast majority of MVIC images of Pluto were acquired in line-scan mode, and line scan images must interpolate the camera vectors for each scan line individually, rather than for the entire image at one time as is done for framing camera images. Therefore, for the purpose of producing a cartographically reliable base map, we use only LORRI framing camera images in the official final global control network. These images are stable in the image plane and the camera distortion is well understood. Stereo pairs utilizing LORRI-only mosaics produce DEMs free of any image-boundary artifacts (whereby incorrect camera distortion models would create offsets that would be interpreted as topographic displacements), confirming that the camera distortion model in ISIS is correct and reliable.

The control network solution in the jigsaw program allows for the solution of the radii of each point, relative to the center of the body. A total of 5001 control points have been mapped on Pluto (Fig. 4) at variable density across the surface. Of these, 4312 control points mostly on the encounter hemisphere were deemed to have sufficient parallax to estimate the radius of these locations.

To rapidly cover the visible disc at high resolution during the hours of closest approach, it was necessary to scan the visible disc of Pluto using MVIC (concurrent linear LORRI strip mosaics or "noodles" covering smaller areas of the visible disk were acquired during this period as ride-along observations with other instruments). The key MVIC scans for cartographic and stereo work for Pluto are the 650-m resolution 4-color scan (P_COLOR2) (using the "red" channel for stereo, which has the best signal-to-noise), the 475-m panchromatic scan (P_MPAN1) and the 315-m resolution closest approach panchromatic scan (P_MVIC_LORRI_CA).

As with all line-scan planetary imaging, each line in the image must be treated as an individual exposure with its own camera pointing and spacecraft position kernels. In principle this may be knowable but in practice must be interpolated line-to-line. The stereo algorithm will interpret any uncontrolled or unknown deviation in the pointing knowledge during the MVIC scans as topography.

Several hemispheric-scale stereogrammetric DEMs are possible using the final 3 MVIC scans and the final LORRI global mosaic (P_LORRI at 0.85 km/pixel), in various combinations (Table 1). Stereogrammetric analysis using MVIC scans shows that the local heights of geologic features are reliably determined but long-wavelength hemispheric scale distortions are introduced due to the interpolation of pointing knowledge associated with these scans. MVIC-based DEMs across Pluto revealed wave-like 'rumpling' of the topography parallel to the lines in the original scan (Fig. 5), typical of terrain models created from line scan imagers. Some of these rumples are subtle, others are more pronounced and clearly non-geological, with amplitudes of up to 500 m in some areas.

To avoid distorting the global control network with unresolved or unknown deviations or fluctuations in the pointing knowledge during each MVIC scan, these images were controlled separately of the stable LORRI-based global control network by assigning control points in the MVIC scans to have fixed locations determined from a LORRI-only basemap. In this independent MVIC-only control solution, which included more than 450 points, both spacecraft position and camera orientation vectors for all MVIC images from P-6 days to encounter were solved. Although concurrent LORRI imaging acquired during the last

Table 1
Stereo observations of Pluto[a].

Left image	Right image	Left image resolution (m)	Right image resolution (m)	DEM vertical precision (m)	Stereo parallax angle
PELR_P_LORRI	PEMV_P_MPAN1	835	475	405	23
PEMV_P_COLOR2	PEMV_P_MPAN1	650	475	405	23
PELR_P_LORRI_STEREO_MOSAIC	PELR_P_LEISA_HIRES	400	235	1120	5
PEMV_P_MPAN1	PEMV_P_MVIC_LORRI_CA	475	315	230	23
PELR_P_LORRI	PELR_P_MPAN_1	835	120	400	23
PELR_P_LORRI	PELR_P_MVIC_LORRI_CA	835	80	195	46
PELR_P_LORRI_STEREO_MOSAIC	PELR_P_MPAN_1	400	120	225	20
PELR_P_LORRI_STEREO_MOSAIC	PELR_P_MVIC_LORRI_CA	400	80	100	43
PELR_P_LORRI_STEREO_MOSAIC	PEMV_P_MVIC_LORRI_CA	400	315	100	43
PELR_P_LEISA_HIRES	PEMV_P_MVIC_LORRI_CA	315	235	90	38.5

[a] PELR refers to a LORRI observation, PEMV to MVIC observation.

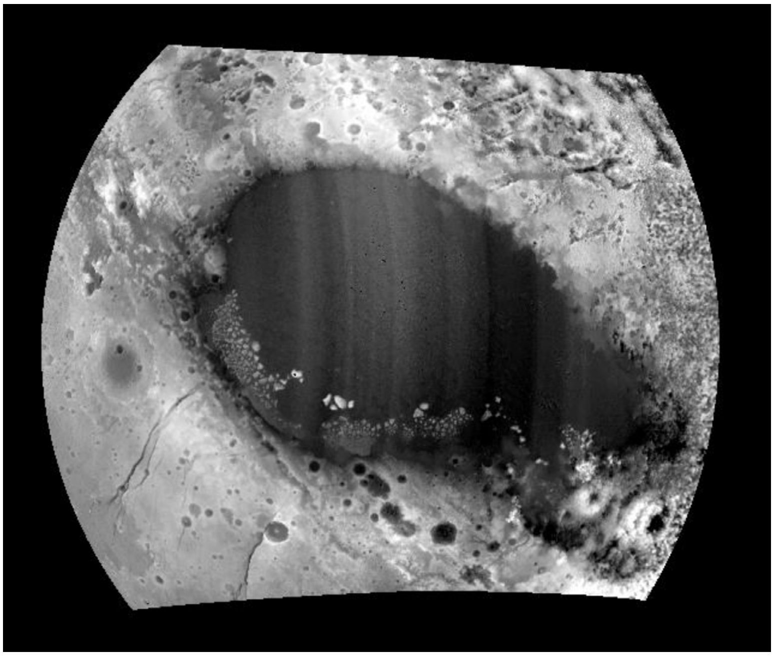

Fig. 5. An example of a “rumpled” distortion across an MVIC-derived DEM of Pluto, prior to distortion removal. This map uses the two best MVIC scans of Pluto as input stereo pairs (Table 1). The fold-like topographic distortions within the large SP depression at center are of amplitudes of ~500 m and are not geologically real, but are also difficult to identify in the rugged elevated terrains to the top and bottom. North is to upper left. Relief shown is from + 4 to − 4 km.

two MVIC scans shows that there was minimal drift or displacement along the scan direction during these scans, the distortions within MVIC-derived DEMs (Fig. 5) show that the precision required for deriving reliable absolute regional- and hemispheric-scale topographic information from MVIC data is not achievable until more advanced ISIS bundle adjustment software becomes available. Local-scale features are very well resolved, however, and entirely consistent with LORRI-derived elevation values.

Differences in image resolution across the surface of Pluto (Figs. 1 and 2) also complicate the task of image control. During the 6.4-day Pluto rotation approach period, the best imaging resolutions on the approach hemisphere are from LORRI framing camera images. In these low-resolution areas, control point quality standards were necessarily lower in order to accumulate sufficient points to register these images and integrate the network across the full 360° of longitude. The resolution contrast between the images from one Pluto rotation before closest approach (at ~15–32 km/pixel) and the overlapping high-resolution (< 1 km/pixel) data at closest approach (Figs. 1 and 2) makes the correlation of control points between the low- and high-resolution data sets challenging. Definable high-contrast features are not abundant in the approach images, where even large craters are impossible to identify. Hence we rely on bright spots and other ‘fuzzy’ albedo features. The iterative approach to editing of control points, described above, was relied upon here as well. The resulting updated camera vectors for both LORRI and MVIC resolved images of Pluto form the basis of the cartographic control network, and can be obtained from the authors (PS or RB) and will be archived in the near future.

We note that Voyager 2 framing camera imaging catalog of Triton shares similar characteristics with the Pluto data set in terms of variable resolution with longitude and high solar obliquity during the encounters. The Triton images were controlled and mapped into a new global mosaic (http://www.into.usra.edu/icy_moons) in essentially the

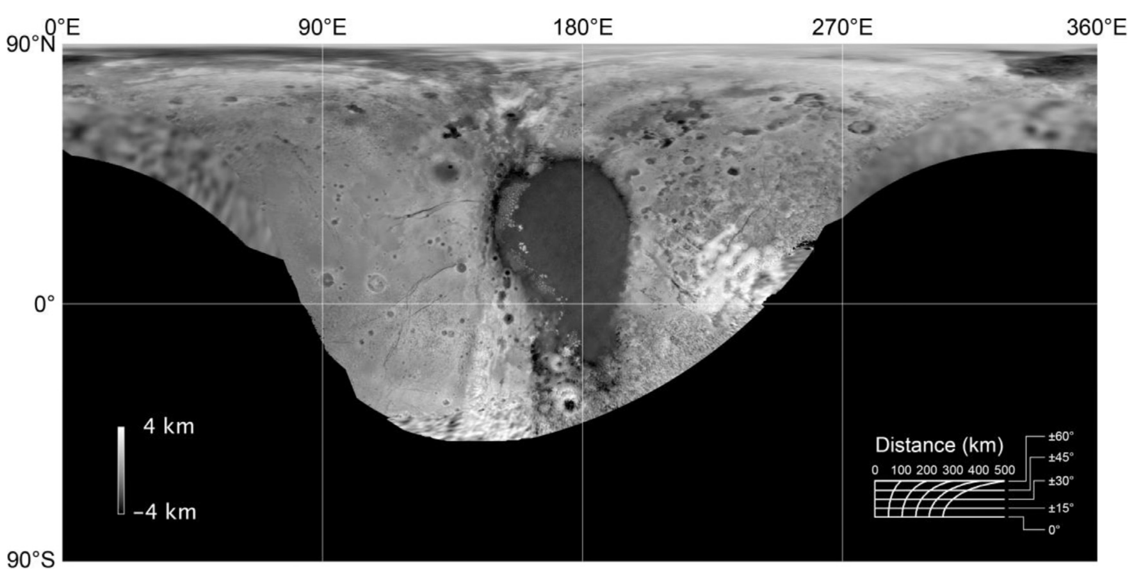

Fig. 6. Global digital elevation model (DEM) of Pluto. Cylindrical map projection centered on 180° longitude. Dark areas were unilluminated or do not have resolvable stereogrammetric data from the 2015 encounter. Note the low resolution and in some areas noisy DEM data sets at upper left and right, derived from imaging data acquires 5–10 hours prior to encounter.

same way as described here, except that Voyager used only framing cameras, had a UV but no IR filter, and vidicon distortions of the image plane required additional corrections. Overall, the mapping coverage is very similar on the two bodies due to similar viewing conditions but effective imaging and mapping resolutions are on the order of 2–3 times better on Pluto than on Triton.

3. Topographic mapping of pluto

The most comprehensive topographic data for Pluto comes from two main sources: bundle adjustments of the control network solution for the determination of radii of widely dispersed control points (described above), and DEM production from stereogrammetric analysis of New Horizons stereo images. Supplemental topographic data from limb profiles, shadow length measurements, and shape-from-shading will be addressed in a future report.

3.1. Control point radii

As described above, control point locations can also be solved for the radius of many points (Fig. 3). If the images associated with any given point were obtained with very low resolution or small or negligible degrees of angular parallax, the jigsaw software will produce a non-useful radius estimate close to or at the mean radius of the body. On approach, image resolutions and parallax were too poor to resolve highs and lows or obtain robust radii for most control points on the sub-Charon hemisphere (Fig. 4). In the high-resolution mapping areas, radii estimates depend on parallax and these values are more robust where the high-resolution mosaics overlap. These mosaics were obtained at phase angles of 15° to 90° and therefore feature significant inherent parallax. Outside the high-resolution mapping zones, parallax is weaker (Table 1) but still sufficient to obtain useful radius estimates for discrete well-resolved features. Control points useful for radius estimation cover an area subtending ~45% of the surface (Fig. 4) but are sparser than obtained from stereogrammetry, requiring extrapolation to form a low-resolution map of Pluto's topography. Significantly denser spacing of control points was achieved in the high-resolution mapping areas were parallax was greater.

3.2. Stereogrammetry

Multiple useful stereo combinations are possible from the New Horizons imaging data (Table 1), permitting construction of topographic DEMs (digital elevation models) of the surface capable of resolving features with estimated vertical precisions of as low as ~100 m in height in many areas (Fig. 6). The precisions quoted in Table 1 for each stereo pair are estimated using the formulation of Cook et al. (1996) and are approximate. The ability of stereogrammetry software to achieve these levels of precisions has been demonstrated on other planetary bodies (e.g., Schenk and Bulmer, 1998; Schenk and Pappalardo, 2004; Schenk, 2009; Schenk and McKinnon, 2009). Contiguous DEM mapping of the encounter hemisphere required use of at least one MVIC scan. A total of 6 regional DEMs with a range of characteristic vertical precisions and resolutions (Fig. 7) were constructed from the best stereo combinations (Table 1), which were then integrated into a final topographic map (Fig. 6) covering ~42% of Pluto's surface.

To derive true elevation maps of Pluto using stereo imaging we use digital stereogrammetry mapping tools (e.g., Schenk and Bulmer, 1998; Schenk and Pappalardo, 2004) designed at the Lunar & Planetary Institute from ISIS code for use on Voyager, Galileo, and Cassini images of icy bodies. Like other similar stereogrammetric tools, the process involves sampling each point in the stereo image pair using areal scene recognition algorithms. Typically these use 5 × 5 pixel patches centered on each pixel in the map (though 3 × 3 patches are sometimes used if data quality allow). The scene recognition searches for the best match to this patch in the second image and derives the parallax from the shift in position of the best match, from which elevation is computed using standard parallax equations. Stereo-DEMs for the best stereo combinations (e.g., Table 1) were then combined to produce a partial global elevation map over all areas where reliable stereo data were available.

Like control point radii maps (Fig. 4), resolvable stereoscopic mapping of Pluto topography (Fig. 6) is limited to the encounter hemispheres centered on 180° longitude, and is variable in quality from ~1000 to 100 m vertical precision. Resolutions and parallax are insufficient to resolve topographic features on the approach (sub-Charon) hemisphere, except where high-resolution imaging on the encounter hemisphere extends beyond the illuminated pole down to ~65°. Hence, useable topographic coverage is restricted to the areas covered by multiple observations on the day of encounter.

The quality of stereogrammetric mapping parameters on Pluto is variable (Fig. 7; Table 1) depending on the stereo sequences used. Due to the nested nature of the LORRI + MVIC mapping coverage, horizontal and vertical precision of resulting DEMs are best along the central section of the encounter hemisphere. The best predicted vertical

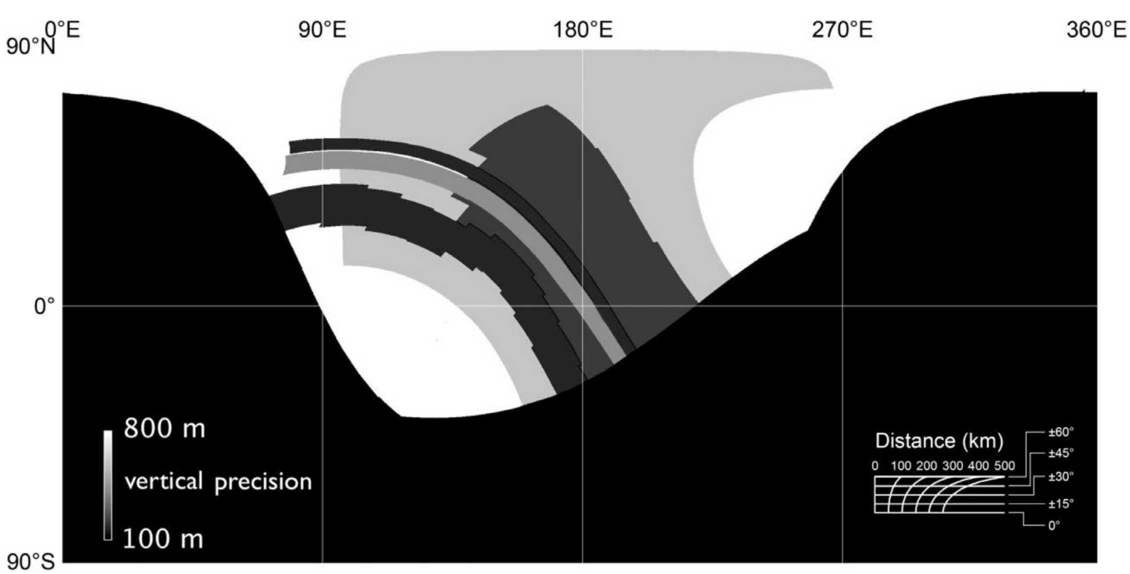

Fig. 7. Map of calculated vertical precision corresponding to Pluto global topographic map in Fig. 6.

precisions are as good as 100 m in some areas (Fig. 7), significantly better than were acquired for Triton (Schenk et al., in preparation), and comparable to most areas on Enceladus (e.g., Schenk and McKinnon, 2009), though not quite as good as was achieved globally on Ceres (Preusker et al., 2016). Stereo DEMs based on MVIC line-scanner images (Fig. 5) are of very high quality but are complicated by the method of image acquisition, resulting in uncertainties or imprecision in cartographic control of the scans. Any distortion or 'rumpling' in the derived MVIC-related DEMs (Fig. 5) must be removed after production, in this case through a low-pass high-pass filtering combination, holding the values of the least distorted LORRI-based DEMs as fixed.

The quality of the DEM data sets for Pluto is remarkably good across the entire closest approach hemisphere (Fig. 6), resolving most geologic features larger than ~1–2 km and features as low as ~100 m in height depending on location (Fig. 7). (All the DEMs used in the global map have inherent noise, as topographic features are resolved at resolutions as least 5 times poorer than the input stereo images. Nonetheless these data do not contain any significant areas of elevation data dropouts, which was a common problem for the Io DEM data (White et al., 2014). Along the centerline of the encounter hemisphere scan, the best resolution DEM combinations were from the PELR_P_LORRI_STEREO_MOSAIC-to-PEMV_P_MVIC_LORRI_CA and for PEMV_P_MPAN1 to PEMV_P_MVIC_LORRI_CA (Table 1) stereo combinations, mainly because it resolved smaller features. Because PEMV_P_MVIC_LORRI_CA observation (MP2_0299179552) did not cover the entire disk of Pluto, the "wings" to either side of the scan were stereogrammetrically mapped using lower-resolution combinations of LORRI with MVIC (Fig. 7; Table 1). The best mapping in terms of resolution of individual geologic features in these areas was provided by the PEMV_P_COLOR2-to-PEMV_P_MPAN1 combination. Despite its poorer nominal vertical precision, a higher DEM quality was provided by this combination due to the better pixel resolutions available.

The only region to produce consistently noisy data in all DEMs was eastern Cthulhu Macula between + 5 and − 20° latitude and 100 and 160° longitude. This is due to the low contrast across this dark terrain, and variability in the brightness of small-scale features with changing phase angles, and the different spectral sensitivity of the LORRI and MVIC-pan imaging systems. These small-scale brightness fluctuations tend to confuse the scene matching software and produce noisy elevation data within this area that must be filtered or masked out. The best quality DEM of this area was again from the MVIC PEMV_P_COLOR2-to-PEMV_P_MPAN1 combination due to the use of similar filters on the same instrument, mainly because smaller features are resolvable, even though the vertical precision is slightly lower. Similarly the bright ice sheet within the vast Sputnik Planitia depression (Moore et al., 2016) produced noisy topography depending on which stereo combination was used, due to the low contrast and the differing appearance of the surface of the ice sheet with changing resolution and different detectors. (We note that this report uses both informal and IAU-approved names for features. The list of currently approved names can be found at the USGS Planetary Nomenclature website [https://planetarynames.wr.usgs.gov].) The only relatively noise-free DEM across the ice sheet came from the PEMV_P_MPAN1-to-PEMV_P_MVIC_LORRI_CA stereo combination (Fig. 5), but this is also the most seriously warped MVIC-related DEM, requiring destriping and adjustment of elevation values to the global base DEM.

3.3. Constructing a valid integrated global-scale topographic map

To construct an integrated topographic map of Pluto's encounter hemisphere we must rely on DEMs derived from at least one MVIC line-scan image as no LORRI-to-LORRI stereo products cover the entire hemisphere to provide us with a reliable long-wavelength topographic base. (Some MVIC-LORRI combinations may be distortion free but an independent method is required to determine if this is true). For smaller scale geologic features, individual DEM products produce identical results and are thus consistent, within the vertical precision of those observations. Hemispheric-scale elevations can vary in the different data sets by hundreds of meters, however. Examination of the three available MVIC-plus-LORRI hemispheric DEM products (Table 1)

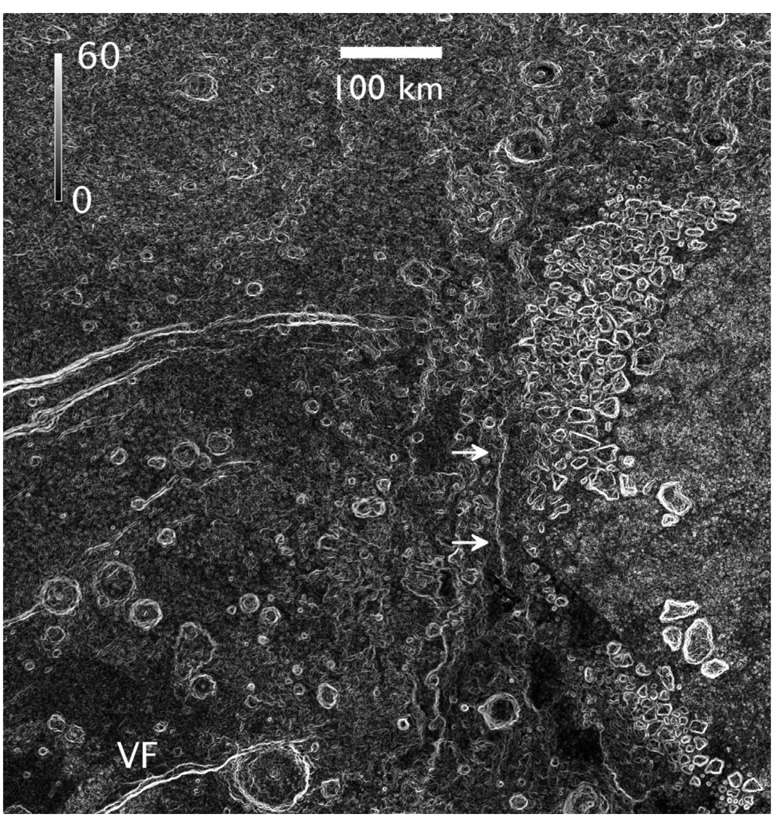

Fig. 8. Excerpt of slope map of western Sputnik Planitia (SP) region of Pluto, derived from topographic data in Fig. 3. Steep sloped sides of the broken blocks of al-Idrisi Montes of western Sputnik Planitia (SP) dominate the right side in this view, while the steep-walled fractures and crater rimwalls of the plains west of SP dominate the left side. Slope range shown here is 0–60°. The coarse appearance of SP (right side of view) is mostly a reflection of the relatively higher noise quality of the DEM there and the lack of resolvable relief of significant magnitude. Arrows highlight scarp along edge of ice sheet; VF is Virgil Fossae fractures which cross the northern rim of Elliot crater near center bottom. Global slope map is too finely detailed to show effectively in its entirety here; area shown extends from 10° to 50° latitude and 130° to 160° longitude. Cylindrical map projection; north is to top. Scene width is ~750 km across.

showed that the map created from the stereo combination of the P_LORRI 5 × 4 mosaic with the MVIC P_MPAN1 produced the least distorted DEM that is also most similar to the control point radii solutions. The remaining MVIC-DEMs for Pluto were warped to this best (i.e., least distorted) topographic map by mapping out the long-wavelength component of the base topography with a low pass filter and the high frequency component of the higher-resolution but more distorted maps. These adjusted products were then combined to produce the integrated topographic map shown in Fig. 6. Comparison of this integrated DEM product with the lower density map of control network point radii (Fig. 4) shows residuals of a few hundred meters on length scales of hundereds of kilometers, which is within the precision limits of the stereo DEMs (Fig. 7).

Two independent data sets exist with which to validate or control the global integrated Pluto DEM in Fig. 3, which is potentially subject to distortions due to limits in MVIC SPICE information. Both of these data sets are low resolution and have quality issues. The first is the map of control point radii (Fig. 4) described above. This map is derived from LORRI images only and is not affected by possible and unconstrained MVIC camera vector distortions. However, many of the points have no effective parallax (being used for image registration) and must be removed from the map product before using. Ideally, we would use lower resolution LORRI-to-LORRI hemispheric stereo products to register the higher resolution MVIC-related DEMs. The only such products we have are LORRI approach images at 2-to-4 km/pixel that form weak stereo pairs with the P_LORRI 5 × 4 mosaic (the last full disk observation by LORRI). We use the P_LORRI 5 × 4 mosaic (the last full disk observation by LORRI). We use PC_MULTI_LONG_1D2B and P_LORRI_TIMERES_4, as these provide sufficient parallax to resolve vertical features of 1–2 km and still resolve useful geologic features. The resulting DEMs are much noisier than the global map and require significant processing, but all the major geologic provinces revealed in the control point radii map and the integrated global stereogrammetric DEM are evident, if not individual geologic features. Topography within Sputnik Planitia is essentially noise in this product due to the inability to resolve small features consistently in image products of low resolution. Hence we have no reliable control over Sputnik Planitia in this data product, but do in the integrated DEM. As a result we use the control point radii map to adjust the vertical component of the integrated topography to produce a corrected-integrated-DEM for Pluto. While local and even regional elevation differences within the integrated global map are reliable (based on selected shadow length measurements and corresponding control point radii values), hemispheric scale differences in the relative elevations of different terrain types could be uncertain by as much as 500 m or more.

Both the global mosaic and topographic map of Pluto are available now at the PDS Cartography and Imaging Sciences Node (IMG) Annex: the panchromatic global mosaic in Fig. 1 is available at https://astrogeology.usgs.gov/search/map/Pluto/NewHorizons/Pluto_NewHorizons_Global_Mosaic_300m_Jul2017 and the global terrain model is available at https://astrogeology.usgs.gov/search/map/Pluto/NewHorizons/Pluto_NewHorizons_Global_DEM_300m_Jul2017. Additionally, all of the data products described in this manuscript have been submitted for long-term archiving as part of the New Horizons PDS delivery, are currently under review, and should be available soon.

As with all digital stereogrammetric topographic mapping products, it must be remembered that the process uses a scene-matching algorithm to determine feature parallax. This degrades the resolution of the features by a factor of between 3 and 5. Smaller features on this scale may or may not be resolved in the final DEM products. Areas of remaining concern are the relatively noisier topographic data in Cthulhu Macula and the partially resolved nature of the surface of the Sputnik Planitia ice sheet relative to the topographic mean.

3.4. Slopes

A map of slopes across the encounter hemisphere of Pluto (Fig. 8) at effective spatial scales of approximately 1 km was derived from the integrated DEM. The quality of the slope map is sensitive to the quality of the input DEM data. Cthulhu Macula and the western and eastern sections of the mapping area tend to have noisier elevation data and hence noisier slope maps. Slope information reported in this text are from the higher quality central sections of the data. Small geologic features such as the narrow ridge crests of the bladed terrain described below (Moore et al., 2018), and the many small round depressions across the surface of the Sputnik Planitia ice sheet (Moore et al., 2016) are not resolved in either the DEM or the derived slope maps, but most recognizable features are. The slope characteristics of Pluto can then be

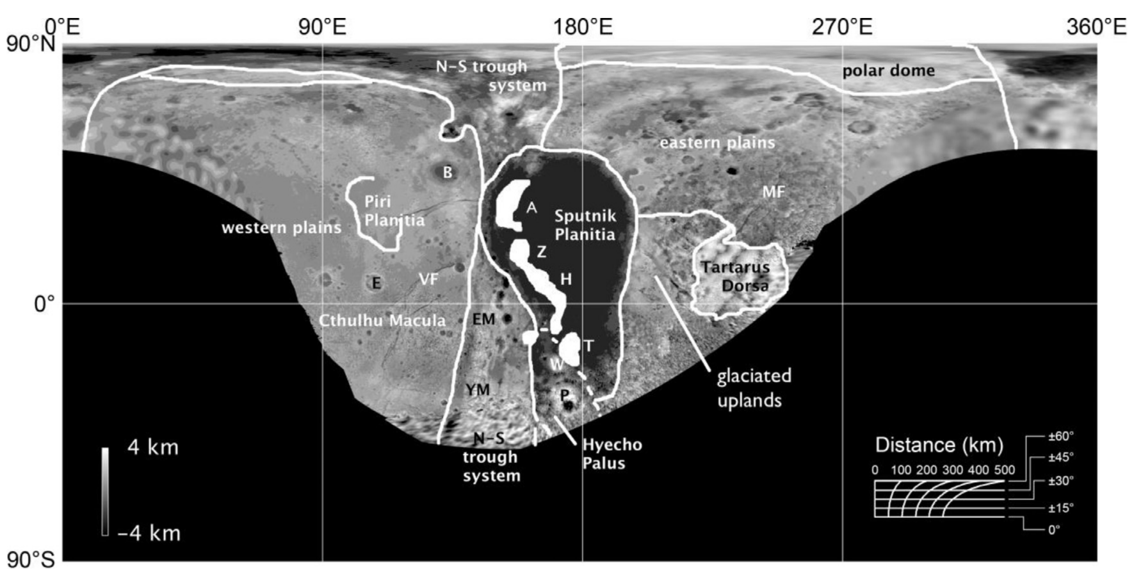

Fig. 9. Annotated map of topography on Pluto outlining major topographic and morphologic provinces discussed in text. Boundaries are approximate and intended only as a guide for the reader to place feature locations. The largest recognized impact craters Edgeworth (E) and Burney (B) are indicated, as are the centers of the most prominent younger graben systems discussed, Virgil Fossae (VF) and Mwindo Fossae (MF), and the volcanic massifs Wright Mons (W) and Piccard Mons (P). The mountainous ranges are shown in solid white, with the most prominent groups labeled (A – Al-Idrisi Montes; Z – Zheng He Montes, H – Hillary Montes and T – Tenzing Montes).

compared with slope data for geologic terrains on active Europa (Schenk, 2009; 2014) and with unpublished data for Ganymede (Schenk et al., 2014); see discussions below.

3.5. Pluto radius

We note that all elevation products and measurements described here are referenced to the estimated mean spherical radius of 1188.3 km (Nimmo et al., 2017), respectively, and are not independent estimates of this mean radius. The long-wavelength (1000-km-scale) elevations across Pluto in the control point and low-resolution LORRI-LORRI DEM are sensitive to the input mean radius of Pluto. The derived radius of Pluto has a current uncertainty of ~1.6 km, and experiments show that the shape of Pluto's surface in the derived DEMs changes curvature with assumed radius. For example, when we use a radius larger than 1188.3 km, the terrains west of SP slope up toward the rim, but for smaller radius values these terrain are flat or slope downward. Hence we urge caution in the interpretation of global-scale topographic trends in the published DEMs until the techniques used to constrain global-scale topography can be validated. All conclusions reported here are those supported by both the control point and stereographic topographic mapping products.

4. Topographic features of Pluto

Pluto shows astonishing local-scale topographic variability across the integrated DEM (Figs. 6 and 9), matching its geologic complexity (Moore et al., 2016). Detailed geologic investigations have been made into some of Pluto's distinctive terrains, notably the glaciated terrains in eastern Tombaugh Regio east of Sputnik Planitia (e.g., Howard et al., 2017b), and the sharp-peaked bladed terrain east of that (Moore et al., 2018). Here we focus on regional and hemispheric scale topographic characteristics and the major topographic provinces of Pluto.

4.1. Topography in extremis

The dominant topographic feature on Pluto is the giant depression enclosing the Sputnik Planitia (SP) ice sheet (Figs. 1, 3, 6; Stern et al., 2015; Moore et al., 2016), described below. This feature is also geographically near the center of the mapping area (Fig. 6) and for convenience other major features are described in reference to it, and are highlighted in Fig. 9. Most of Pluto's surface outside of Sputnik Planitia consists of broad plains that can be divided into 3 major types. To the west of SP the plains are relatively flat and mostly featureless (Fig. 10) aside from widely scattered craters of different sizes, and occasional tectonic scarps or fractures up to 3 km deep. The scattered craters are noteworthy for the bright annular rings flanking their rims, which are not common in other terrains. The most prominent erosional feature is a crenulated scarp 200–300 m high (Figs. 9 and 10) enclosing the irregular 300 × 600 km wide Piri Planitia (Moore et al., 2016; 2017). Piri Planitia also appears to be gently domed near the center by a few hundred meters. Doming could have induced small-scale fracturing, encouraging landform degradation and scarp retreat in this area. The integrated DEM suggests the western plains slope gently downward to the west away from SP (Fig. 10) but this conclusion is tentative pending resolution of the geodetic question.

The elongated 3000-km-long dark region between 5° and − 25° latitude referred to as Cthulhu Macula (Figs. 1, 3 and 10) is to first order topographically indistinguishable from the low plains west of Sputnik Planitia described above. Cthulhu Macula is thus essentially a southern extension of those plains with no boundary or major change in topographic character (the higher DEM noise levels within this terrain notwithstanding). Therefore the northern boundary of this distinctive albedo and color associated with this broad latitudinal feature (Fig. 1) is likely controlled by latitude (e.g., Protopapa et al., 2017; Schmitt et al., 2017) and not elevation, consistent with the gradational albedo change. The brightening along the southern margin of Cthulhu Macula (Fig. 1) does appear to correlate with a gentle rise of 1–1.5 km (Fig. 6). The eastern margin of the dark Cthulhu Macula deposit is abruptly terminated by the depressed ice sheet, although there are local areas of bright ice deposits within this area that correlated with high elevations (e.g., Enrique Montes and York Montes, discussed below). The eastern end correlates with an inferred outcrop of elevated bladed terrains. These local topographic relationships are explored further in the Tectonics sections below.

Although also of low amplitude, the lightly cratered plains to the east of SP (and north of ~23° latitude; Fig. 11) are distinctly different in character to those on the west side. These plains are scarred by numerous ovoid- to amoeboid-shaped enclosed walled depressions of apparent non-impact origin (Howard et al., 2017a, 2017b), as well as widely scattered circular depressions of more probable impact origin. The non-circular walled depressions are typically 1–3 km deep [rim-to-floor], with the deepest being 3.5 km (Fig. 11), with wall slopes of 20° to 45° common. The largest of these walled depressions are noteworthy

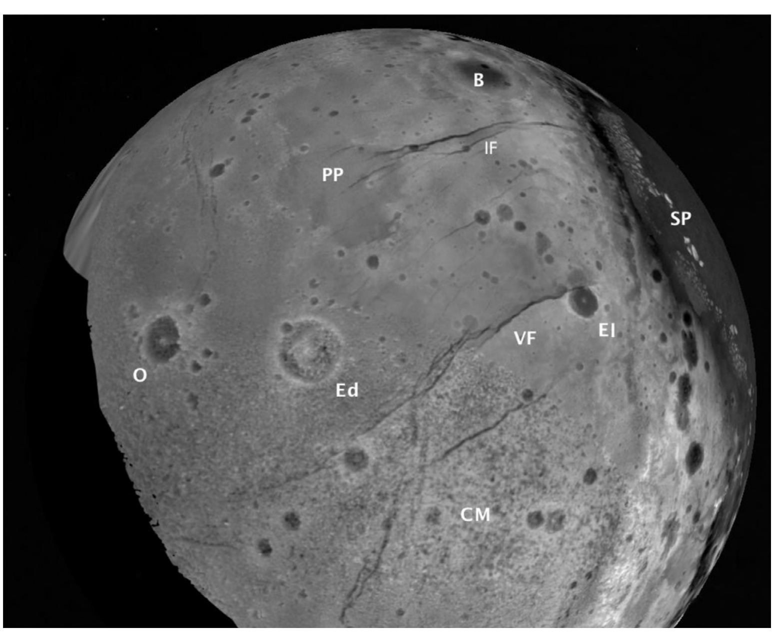

Fig. 10. Point perspective view of Pluto integrated DEM (Fig. 6) centered over smooth plains west of Sputnik Planitia (SP). Major features are Piri Planitia (PP, which is surrounded by a low scarp), 180-km-wide degraded Burney crater (B), craters Oort (O), Edgeworth (Ed), and Elliot (El), and the deep fractures Inanna Fossa (IF) and Virgil Fossae (VF). Edgeworth crater is ~145 km across. The dark region Cthulhu Macula (CM) extends along the lower part of the scene but is topographically indistinguishable except for the higher level of noise in the DEM. Dark is low in all similar figures. North is at top; relief shown is + 4 to − 4 km; view centered at 10°N, 117°E.

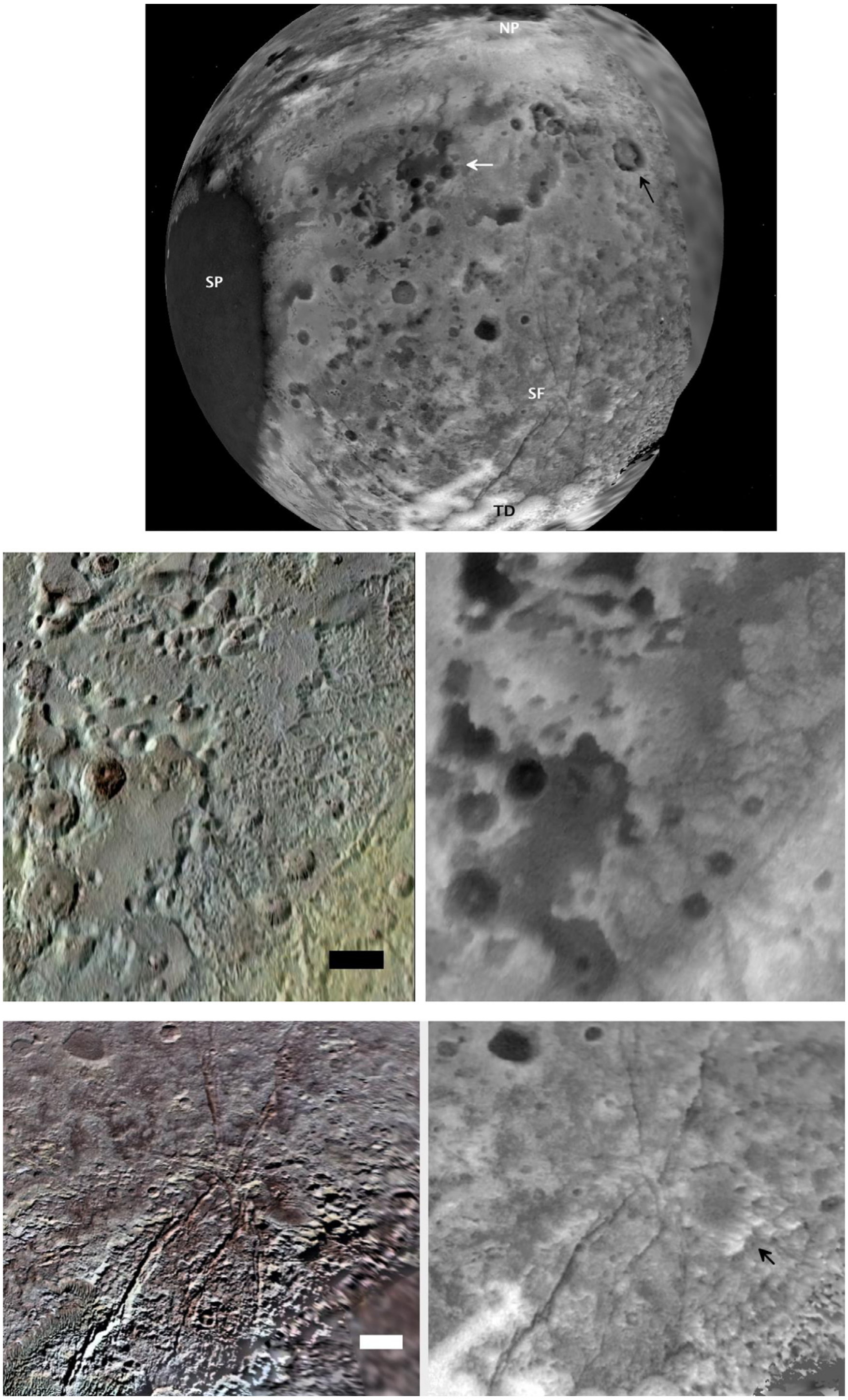

Fig. 11. Point perspective view of Pluto integrated DEM (Fig. 6) centered over eroded plains east of Sputnik Planitia (SP). Major features include the elevated plateaus of Tartarus Dorsa (TD), the radiating fracture network of Mwindo and Sleipnir Fossae (SF), and the elevated dome associated with the North Pole (NP). Black arrow highlights 110-km crater that appears to be filled with partly eroded deposits, and which may be related to Edgeworth crater (Fig. 10). White arrow indicates irregular depression associated with sinuous valley networks, which itself sits within a broader depression. Relief shown is + 4 to − 4 km; view centered at 53°N, 229°E. (b) Section of global color mosaic (left) and DEM (right) showing close-up of Fig. 11a showing sinuous channels descending into an irregular depression at bottom center. These features lie within a broader region of low topography. Black scale bar is 50 km; relief shown is + 4 to − 4 km, north is to top; centered at 67°N, 216°E. Left side is from the global digital mosaic (Fig. 1); right side from the global DEM elevation map (Fig. 6). The online color version is from the 4-color global mosaic (Fig. 1) and uses MVIC filters "blue", "red" and "CH_4," which provide the greatest color contrast. (c) Section of global color mosaic (left) and DEM (right) centered on Mwindo Fossae with Sleipnir Fossae extending to bottom left (see Fig. 6 or 9 for location). Arrow highlights disrupted massifs several km high flanking a possible eroded impact crater. High plateaus at bottom left are northern exposures of Tartarus Dorsa. Scene width is ~650 km across; relief shown is + 4 to − 4 km; white scale bar is 50 km; centered at 33°N, 244°E. The color version is from the 4-color global mosaic (Fig. 1) and uses MVIC filters "blue", "red" and "CH_4," which provide the greatest color contrast. (For interpretation of the references to color in this figure legend, the reader is referred to the web version of this article.).

for channel-like valleys that appear to drain into them (Fig. 11b), as described by Howard et al. (2017b). The deepest of these irregular enclosed depressions appear to occur between 50° and 70° latitude; whether this is coincidence or a real trend is unclear as half of this latitudinal band is not resolved in the integrated DEM. Why these plains should be so extensively eroded whereas those west of SP are not, despite occurring at similar latitudes, is unclear.

The more circular crater-like depressions in these eroded plains are in varying states of erosion. The largest of these is ~115 km across and located at + 61°, 278° (Fig. 11b). While ~3 to 3.5 km deep, it is noteworthy for the irregular raised plateau that partially fills it, possibly an erosional remnant of a deposit that may have once filled the crater (Arrow, Fig. 11a). The fractures of Mwindo and Sleipnir Fossae in the southern sections of these plains (Fig. 9) are resolved in the DEM as 1–2 km deep (Fig. 11c). To the east and southeast of Mwindo Fossae lies a small cluster of irregular knobby hills up to 3 km high (Fig. 11c). Whether these are erosional is undetermined but they are among the highest individual features outside SP on Pluto and may indicate a change in morphology into the complex albedo patterns that are unresolved to the east of the DEM coverage area (Fig. 1).

To the southeast of SP (and south of ~23° latitude), the plains are deeply and densely pitted (Fig. 12) and interpreted as glaciated (Moore et al., 2017; Howard et al., 2017b). These terrains are extremely rugged on a local scale (Fig. 12) but do not feature any broad domical

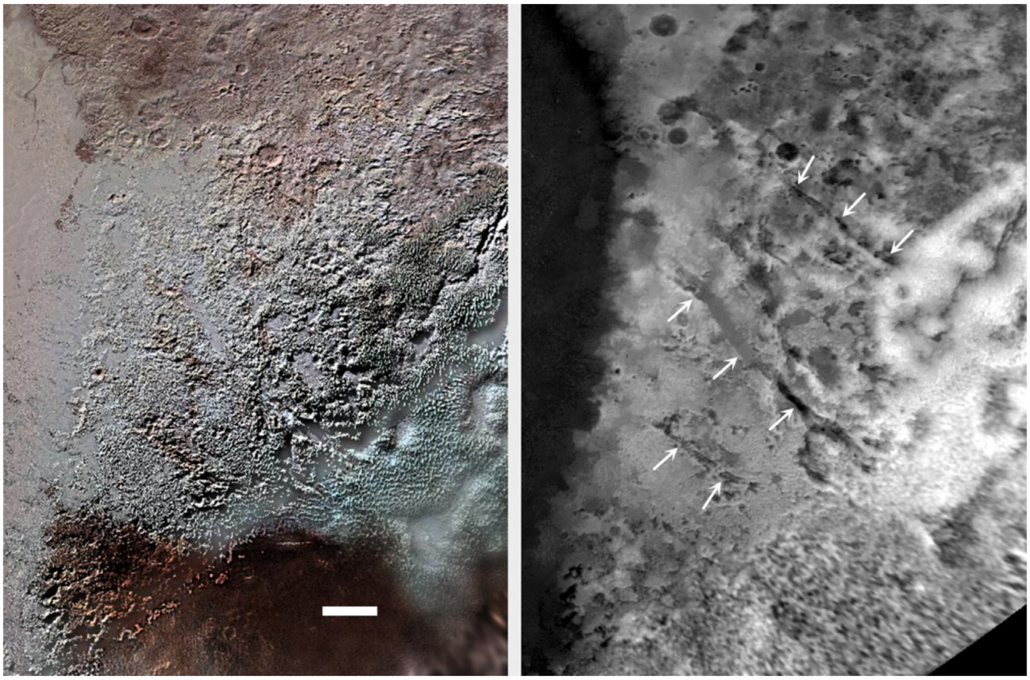

Fig. 12. Glaciated plains of eastern Tombaugh Regio, Pluto, from global color mosaic (left) and DEM (right). Plains are elevated roughly 500 m above plains to the north, and correlate with the higher reflectance terrains in the global color mosaic. Arrows highlight three through-going depressed linear NW-SE trending troughs interpreted as fault-bounded graben. Elevated plateaus of Tartarus Dorsa are to the right. Scene width is ~850 km across; relief shown is + 4 to − 4 km, white scale bar is 100 km; centered at 12°N, 212°E. The color version is from the 4-color global mosaic (Fig. 1) and uses MVIC filters "blue", "red" and "CH_4," which provide the greatest color contrast. (For interpretation of the references to color in this figure legend, the reader is referred to the web version of this article.).

or depressed deviations from the mean surface and thus are relatively consistent in elevation. The numerous pits are typically 5–10 km across and up to 4 km deep (Fig. 10), and some apparently filled by small deposits of smooth material. The abundance of similar depressions with a narrow size distribution suggests they are endogenic, and few definable impact features can be resolved (Singer et al., 2018). Three linear troughs cross this terrain (Fig. 12). The troughs are approximately radial to SP and appear to be related to those observed in the western plains (Fig. 10), but these examples are significantly eroded and appear to be partially filled with smooth material similar to that which partially fills many (but not all!) of the small pits.

These glaciated terrains southeast of SP (Fig. 12) are elevated ~720 m above Pluto mean (on average) and also the eroded plains to the north described above. This elevated region also correlates with the high albedo province referred to as eastern Tombaugh Regio that extends east from the edge of SP (Figs. 1 and 12). The higher elevation may have triggered the accumulation of ices or frosts that initiated glaciation in the region, though the degree of landform modification is so extensive that it has largely erased the signature of any putative original surface.

Table 2
Slope characteristics of basic terrain types on Pluto at 1 km scales.

Terrain name	Terrain type	Mean slope (deg)	Standard deviation
Sputnik Planitia	Ice sheet	4.4	3.1
Western plains	Smooth cratered plains	7.9	5.1
Eastern plains	Eroded plains	9.0	7.0
Eastern Tombaugh Regio	Glaciated plains	14.8	9.3
Hyecho Palus	Volcanic plains	9.8	7.6
al-Idrisi Montes	Massif range	13.6	8.9
Hillary Montes	Massif range	16.0	10.4
Zheng He Montes	Massif range	16.0	11.6
Tenzing Montes	Massif range	19.2	11.0

The region south of the glaciated highlands of eastern Tombaugh Regio, a dark area known informally as Krun Macula (Fig. 13), is best

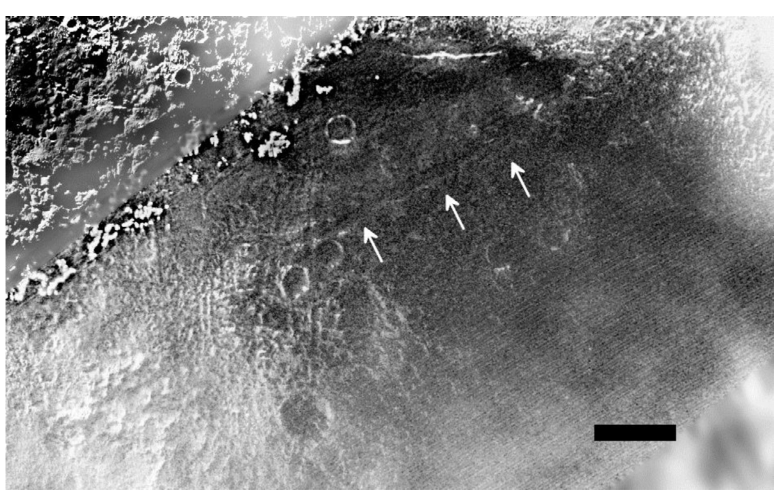

Fig. 13. Portions of Krun Macula, Pluto, from global color mosaic. Arrows indicate large fracture flanked by several craters revealed in these haze images. This dark region was best resolved in haze-light by MVIC at ~315 m/pixel. Scene width is ~700 km across; scale bar is 50 km; centered at 12°S, 213°E.

revealed in the haze-illuminated images at 0.65–0.315 km/pixel. Although the signal-to-noise in the DEM and images is lower here, several impact craters and a large double-walled trough 10-km-wide and ~200 km long are evident. The DEM, though noisy, suggests the haze-illuminated region of Krun Macula is at an elevation close to the global mean radius.

The slope characteristics of the western and eastern plains are rather similar, despite the greater degree of erosion in the eastern plains (Table 2). This is likely because the eroded irregularly shaped depressions that mark the eastern plains (Fig. 11) have steep walls and flat floors that tend to mimic the depth and slope characteristics of the circular impact craters commonly found in the western plains (Fig. 10). Except for the SP ice sheet, these plains units have the lowest mean slope characteristics (slopes and standard deviations) on Pluto, with mean slopes of 8 to 9° (Table 2). The glaciated plains of eastern Tombaugh Regio have steeper mean slopes of ~15° but these data do not yet resolve the small-scale pitted features so abundant there.

The highest standing terrains on Pluto are the “bladed terrains” of Tartarus Dorsa described by Moore et al. (2016). These units form lobate or elongate amoeboid-shaped plateaus 75 to > 450 km wide, and 2–5 km high relative to the adjacent cratered and glaciated plains on which they appear to be superposed (Figs. 12 and 14). In the high-resolution mapping area these are revealed to have a broadly arched profile (Fig. 14) and are covered with densely spaced narrow steep-sided ridges, giving rise to the name ‘bladed’. The individual ridges observed at high resolution are not resolved in the stereo DEMs, but preliminary shape-from-shading results indicate heights of hundreds of meters, up to ~1 km (e.g., Moore et al., 2018). The main grouping within the DEM area is found between − 5° and 25° latitude and between 220 and 252° longitude. No other exposures of similar materials are found within the topographic mapping area, though other exposures are suspected at similar latitudes based on color and albedo patterns (e.g., Moore et al., 2018) and inspection of limb images indicate the presence of rounded plateaus in several of these areas, particularly between − 15° and 20° latitude and 5° and 40° longitude.

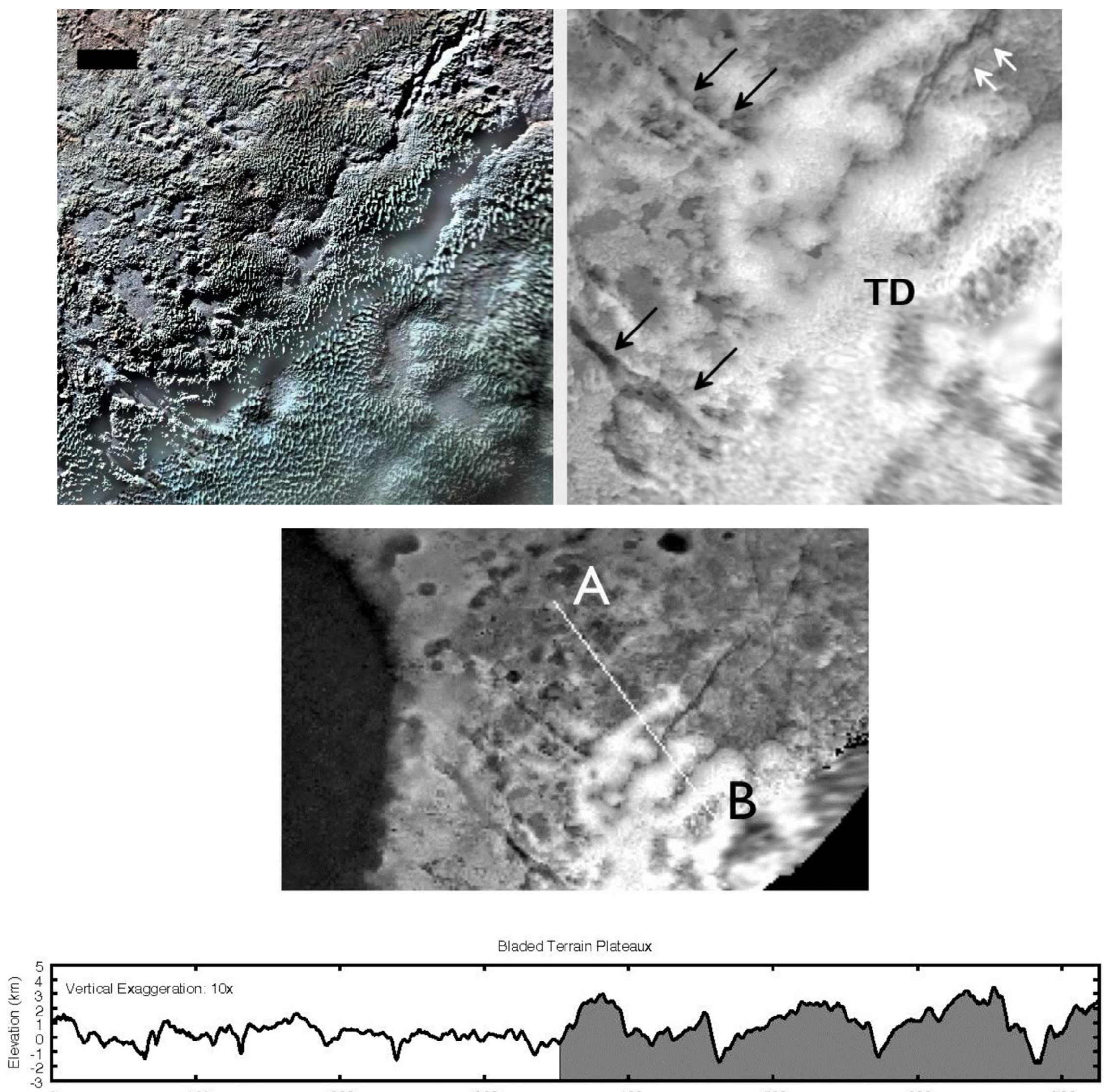

Fig. 14. (a) Best resolved portions of Tartarus Dorsa (TD), the main exposure of ‘bladed’ terrain in the mapping area, from global color mosaic (left) and DEM (right). The plateaus are typically higher in their centers. Dark arrows indicate two older graben that may be related to those seen in the western plains (Fig. 10), and white arrows indicate the southern extension of the younger troughs of Sleipnir Fossae (Fig. 11). Scene width is ~580 km across; relief shown is + 4 to − 4 km; black scale bar is 50 km; centered at 11°N, 226°E. The bottom right quadrant of the scene was illuminated by sunlight scattered by atmospheric haze. The color version is from the 4-color global mosaic (Fig. 1) and uses MVIC filters “blue”, “red” and “CH_4,” which provide the greatest color contrast. (b) Profile across bladed terrain plateaus. Inset view shows location of profile. (For interpretation of the references to color in this figure legend, the reader is referred to the web version of this article.)

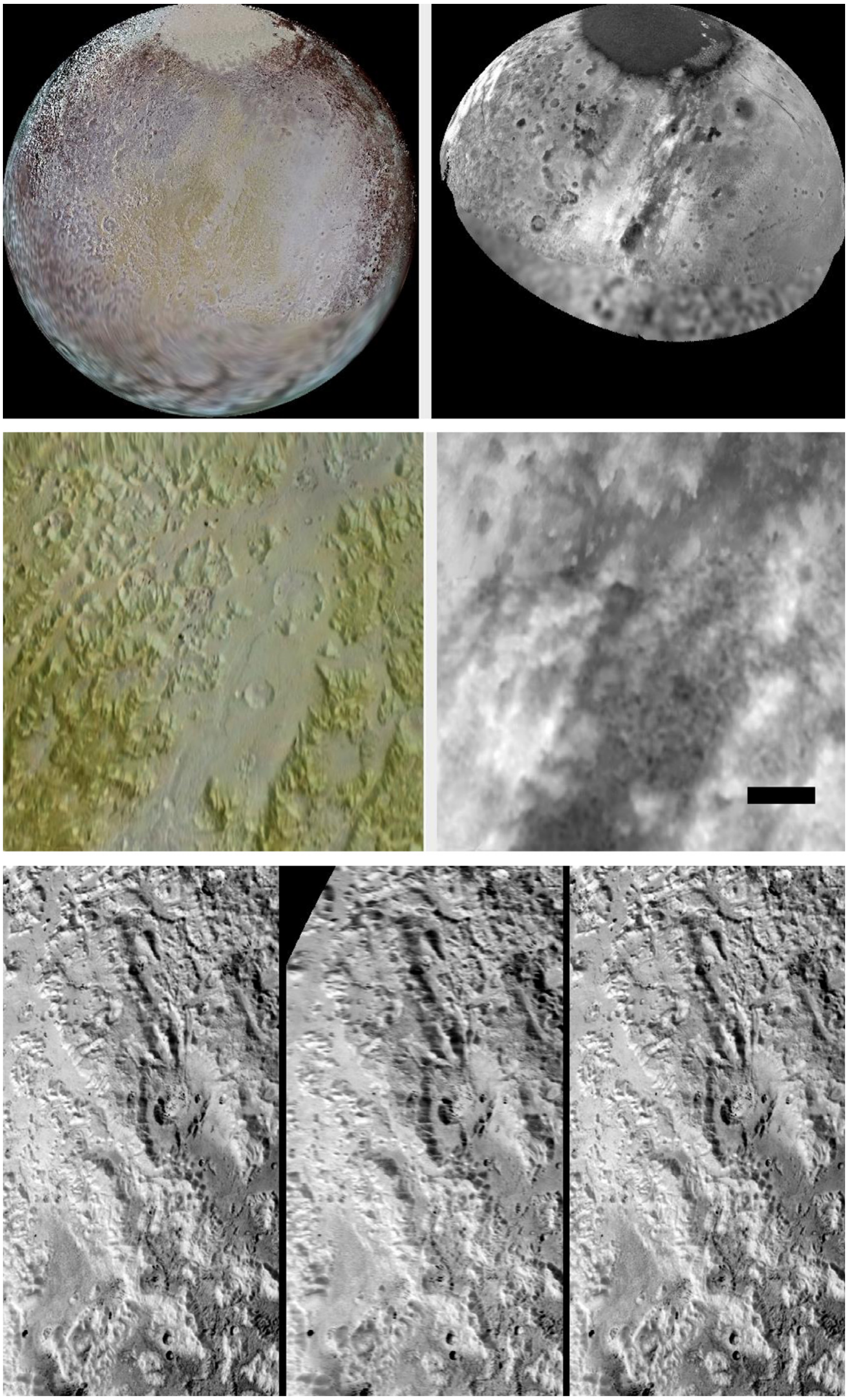

Fig. 15. (a) Global 4-color map (left) and digital elevation model (right) of Pluto, showing entire northern hemisphere in polar orthographic projection. Sputnik Planitia and 180° meridian are at top. Broad eroded 600-km-wide topographic dome at center corresponds with yellowish coloration in the base map due to methane. The dome is roughly bisected by a large trough system up to 5 km deep that extends to the upper center right. Relief shown is + 4 to − 4 km. The color version is from the 4-color global mosaic (Fig. 1) and uses MVIC filters "blue", "red" and "CH_4," which provide the greatest color contrast. (b) Crop of global color mosaic (left) and DEM (right) from Fig. 15 centered on 90° pole of Pluto. Visible diagonally across center is eroded trough cutting into polar dome. Smooth floor material in trough, punctuated by scattered impact craters, may be due to pervasive erosion of flanking trough walls. Cropped from center of Fig. 15. Scene width is ~350 km across; relief shown is + 4 to − 4 km; scale bar is 50 km. The color version of the image mosaic is from the 4-color global mosaic (Fig. 1) and uses MVIC filters "blue", "red" and "CH_4," which provide the greatest color contrast. (For interpretation of the references to color in this figure legend, the reader is referred to the web version of this article.). (c) Stereo pair of region shown in Fig. 15a, highlighting the deeply eroded troughs in the north polar region of Pluto. Image resolutions are 650 and 315 m/pixel. Note that orientation is different to align stereo pair for viewing. Figure format allows user to view in either wall-eyed mode (left-center) or cross-eyed mode (center-right). Red-blue anaglyph version of this figure is available in Supplementary Fig. 1. (For interpretation of the references to color in this figure legend, the reader is referred to the web version of this article.)

4.2. North polar dome

The north polar Lowell Regio of Pluto is highlighted by the presence of a broad deeply eroded dome ~600 km across and roughly 2 km higher than the lightly cratered plains flanking SP at lower latitudes (Fig. 15). This dome has no discreet margin but rather grades into the surrounding plains described above. A large trough system up to 5 km deep (and described in detail in the next sections) essentially bisects this dome very near the geographic pole. The global color pattern in the north (Figs. 2 and 15) correlates with the elevation pattern across this dome (Fig. 15), indicating that topographic control of colors and surface composition is important here (e.g., Grundy et al., 2016; Young et al., 2017), in contrast to the lack of topographic control of color and albedo along the northern margins of Cthulhu Macula.

4.3. The Sputnik Planitia basin

The largest unambiguous impact crater on Pluto, Edgeworth (D ~ 125 km) is only ~2 km deep and the deepest observed crater (Harrington crater, D ~ 82 km at − 6°, 155°) is ~4 km deep rim to floor. Unlike the heavily cratered icy moons of Saturn (Schenk et al., 2018b), the modest impact cratering observed on Pluto (Figs. 1 and 3) does not dominate the global topographic signature and crater morphologies are discussed in detail separately (Schenk et al., in preparation). The two exceptions to this are the eroded multiring 180-km-wide Burney crater (Figs. 6 and 8) and the giant topographic basin enclosing the smooth bright Sputnik Planitia nitrogen-methane-CO ice sheet (Stern et al., 2015: Fig. 3). This deep basin overwhelmingly dominates the topography of Pluto, and based on morphology and preliminary topographic data indicating a depression several kilometers deep, Moore et al. (2016) concluded that this basin was a large highly degraded impact structure subsequently partially filled with volatile ices. We concur with this conclusion and explore the topographic properties of this large structure in greater detail.

The bright volatile-ice-rich deposit forming SP is broadly flat lying and forms a roughly 1500 × 900-km-wide pear-shaped oval with its smaller end to the south (e.g., Moore et al., 2016; McKinnon et al., 2016). Determinations of the absolute elevation and degree of flatness of the ice sheet itself are subjects on ongoing investigations and are deferred to a subsequent report (e.g., Schenk et al., 2018c). This is due to residual uncertainties from the MVIC distortions of a few hundred meters vertically, which must be resolved using high resolution LORRI stereogrammetry.

The SP bright ice deposit is enclosed within a larger pear-shaped topographic basin, defined by an eroded and modified broadly arched raised ridge 125–175 km wide and variable in elevation, rising locally up to ~1 km above surrounding plains and 2.5–3.5 km above the surface of the Sputnik Planitia ice sheet (Figs. 6 and 16). The exact

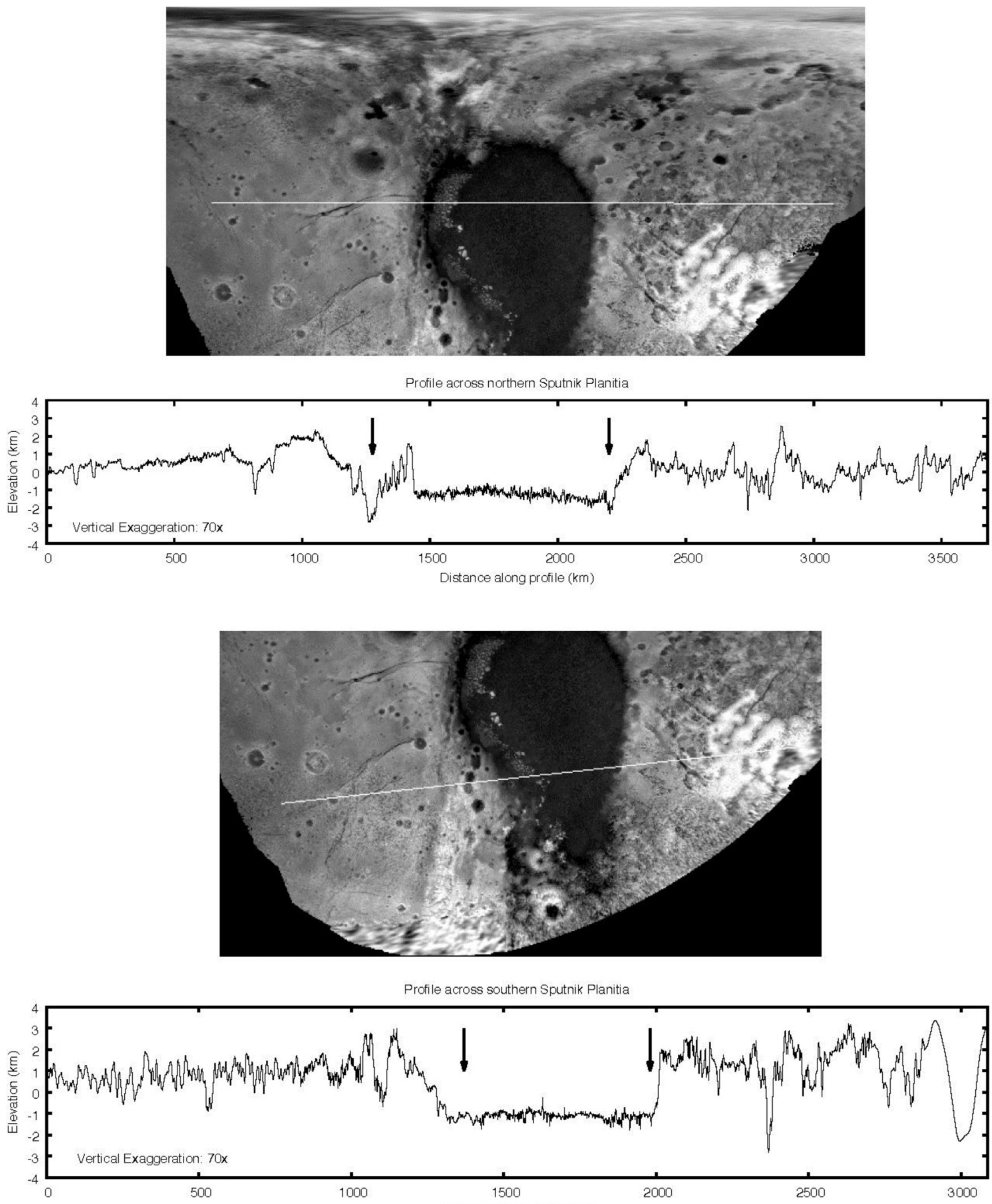

Fig. 16. Profiles across the northern (top) and southern (bottom) halves of Sputnik Planitia and surrounding terrains. Data profiled from Fig. 6. Arrows indicates depressed moats and raised margins along outer edges of the low-lying ice sheet in SP.

dimensions of this outer ridge-ring depend on how it is defined. Taking the highest elevation across the broad topographic swell, we obtain axes of ~2000 by 1200 km. With a basin-to-planet diameter ratio of ~0.67, the SP basin is among the largest in size known with respect to the host planet, larger than the Odysseus basin on Tethys, which has a ratio of ~0.4, though not as large as Rheasilvia on Vesta, which has a ratio of ~0.95.

The morphologic character of the ridge-ring surrounding SP changes with azimuth from the center. To the north and northeast the rim forms a broad arched rise referred to as Cousteau Rupes, reaching up to ~3 km above the ice sheet. This escarpment is pervasively incised by innumerable densely spaced small valleys (Fig. 17), some of which are embayed by SP ice along the interface between SP and the surrounding rim (Moore et al., 2016). The DEM also reveals that the outer 10–20 km of the ice sheet are depressed a few hundred meters relative to the interior of the ice sheet along its contact with the eroded rim escarpment (Figs. 16 and 17).

The southern margins of SP are rather different from those in the north. The southeast margin of SP between 20° and −10° latitude (Fig. 18), where it flanks the moderately elevated glaciated terrains of eastern Tombaugh Regio (see Fig. 12) do not have the shallow moat seen to the north (Fig. 17). Rather, the outer 50–75 km of SP here is

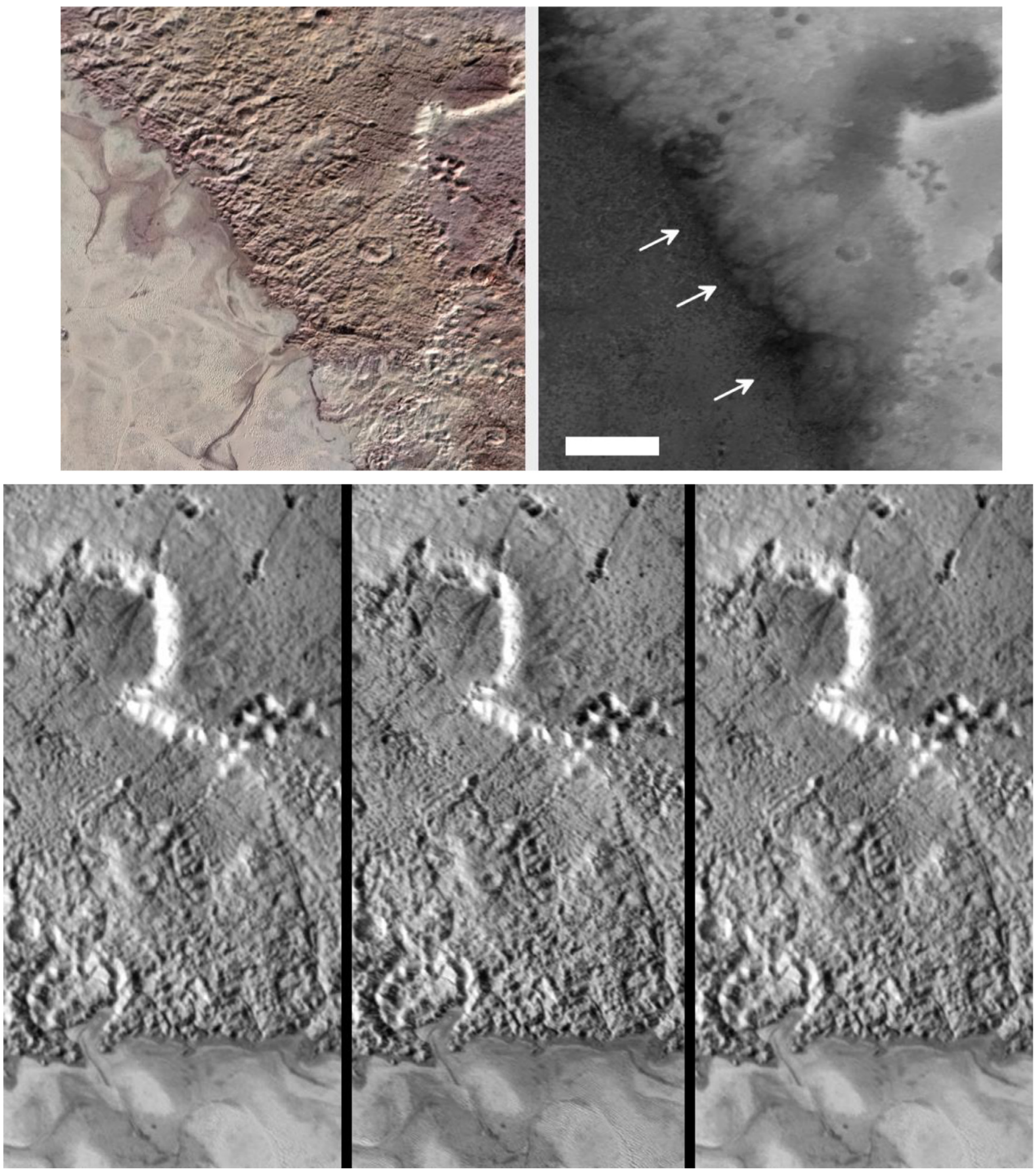

Fig. 17. (a) Section of global color mosaic (left) and DEM (right) showing the northeastern rim of the Sputnik Planitia basin. The eroded escarpment forming the outer edge of the SP ice sheet is informally known as Cousteau Rupes and is 2–3 km high. Arrows highlight depressed 'moat' along outer margin of the ice sheet in this area. Several reentrants of the ice sheet into local valleys of the rim scarp are present. Scene centered at 40° latitude. Scene width is ~220 km across; relief shown is + 4 to − 4 km; white scale bar is 50 km; centered at 40°N, 194°E. The color version is from the 4-color global mosaic (Fig. 1) and uses MVIC filters "blue", "red" and "CH_4," which provide the greatest color contrast. (b) Stereo pair of region shown in Fig. 17a, highlighting erosional valley networks along the raised rim of the Sputnik Planitia basin. Image resolutions are 650 and 315 m/pixel. Note that orientation is different to align stereo pair for viewing. Figure format allows user to view in either wall-eyed mode (left-center) or cross-eyed mode (center-right). Red-blue anaglyph version of this figure is available in Supplementary Fig. 2. (For interpretation of the references to color in this figure legend, the reader is referred to the web version of this article.)

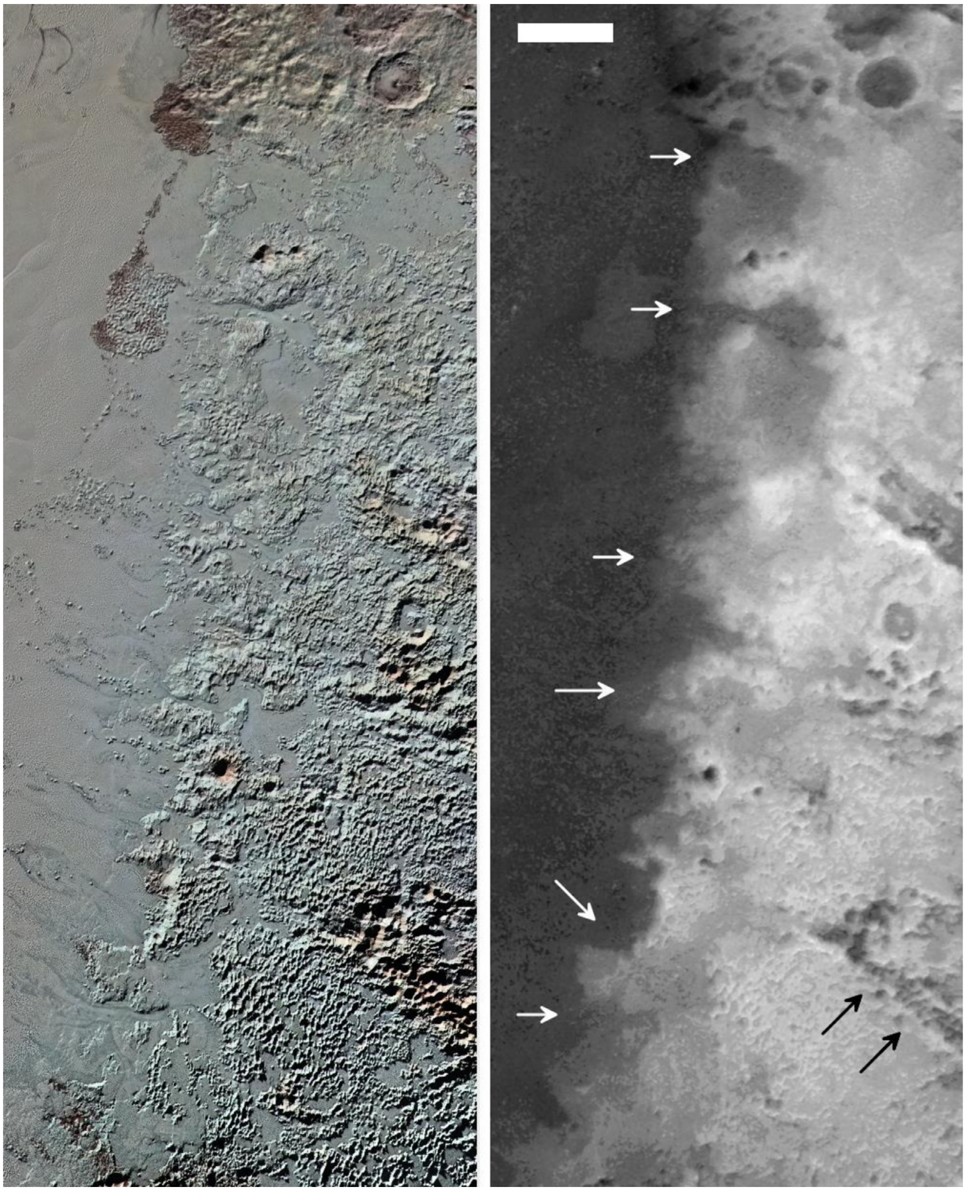

Fig. 18. Section of global color mosaic (left) and DEM (right) showing the southeastern rim of the Sputnik Planitia basin, between − 4° and 32° latitude. Dark arrows highlight an eroded trough with a reddish color in the 4-color global mosaic, suggesting local control of color in some areas. White arrows indicate prominent areas where glacier-like flows exit from the highlands downslope onto the SP ice sheet from several different topographic levels. Most of the edge of the SP ice sheet rises 100–300 m where is meets the elevated rim. Scene width is ~230 km across; relief shown is + 4 to − 4 km; scale bar is 50 km; centered at 14°N, 198°E. The color version is from the 4-color global mosaic (Fig. 1) and uses MVIC filters "blue", "red" and "CH_4," which provide the greatest color contrast. (For interpretation of the references to color in this figure legend, the reader is referred to the web version of this article.).

elevated a few hundred meters along the zone where the ice sheet contacts the rugged glaciated terrains flanking SP in this area. Within the rugged elevated rim region, numerous flow-like deposits descend topographically outward from eastern Tombaugh Regio and merge into the lower ice sheet within SP (Fig. 18) indicating that glaciers from eastern Tombaugh are feeding material into SP (Howard et al., 2017b).

To the far south (near the southern stem of the "pear"), the topographic character of the outermost edge of SP ice sheet is complex (Fig. 6). At the southernmost edge of SP, the ice sheet is 4 km below mean radius and is one of the deepest surfaces on Pluto. The edge of the ice sheet forms small lobes that embay local depressions, some of which appear to be ice-free and have dark reddish colors. Conversely, several ovoid depressions 5–35 km across occur along the southeastern margin (Fig. 19). These are 1–3 km deeper than the elevation of the ice sheet and are evidently embayed by it (Fig. 19), despite the lower apparent elevation. Thus, the SP ice sheet formed in some local depressions but not others. Whether lateral flow was involved is unclear.

Within the haze-lit areas south of the southern margin of SP proper, we observe several exposures of smooth material embedded within the rugged flanking terrains (Fig. 20). These deposits resemble SP icy materials in their smoothness and embayment of topographic lows (Fig. 20). These are interpreted to be outliers of SP ice deposits stranded outside the main ice sheet. If any continuation of SP-related deposits occurs farther south they are unobservable due to darkness.

The western margin of SP is more complex than the eastern margins and several interesting relationships are evident in the topography (Figs. 6, 8, 21 and 22). The deepest areas within SP basin, and among the deepest on Pluto, occur along the base of the arched western ridge-ring enclosing the SP depression. These surfaces are ~3.5 km deep relative to mean radius (locally reaching − 3.8 km in a few spots) and between 3.5 and 4.5 km deep with respect to the adjacent crest of the SP outer ridge-ring. Most of these low surfaces are free of the N_2-rich bright ices covering SP, and may represent exposures of the pre-ice-sheet depression floor. South of 10° latitude, the outer 20–50 km of the ice sheet rises a few hundred meters along the contact with the ridge-ring (Fig. 22, much as it does on the southeastern side (Fig. 18). The difference on the western side is that any active glaciation that may have been occurring on the rim escarpment here has ceased.

4.4. The Sputnik Planitia basin – Western Massifs

Dozens of angular massifs 5–25 km across form an incomplete

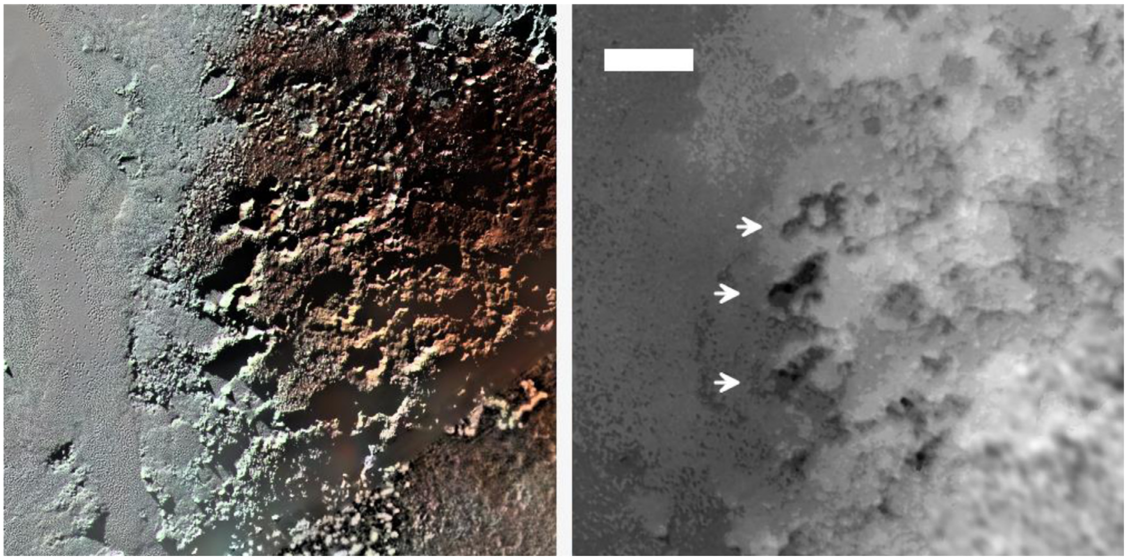

Fig. 19. Section of global color mosaic (left) and DEM (right) showing the southeastern rim of the Sputnik Planitia basin centered at − 11° latitude. White arrows highlight deep pits along the transition between the ice sheet (left) and eroded highlands (right). While the pits have smooth bright material on their floors, that have not been filled to the same level as the main ice sheet. Scene width is ~250 km across; relief shown is + 4 to − 4 km; scale bar is 50 km; centered at 11°S, 195°E. The color version is from the 4-color global mosaic (Fig. 1) and uses MVIC filters "blue", "red" and "CH_4," which provide the greatest color contrast. (For interpretation of the references to color in this figure legend, the reader is referred to the web version of this article.).

arcuate ring along the western margins of Sputnik Planitia (e.g., Moore et al., 2016; Singer et al., 2017). These massifs can occur as isolated blocks or in elongated clusters or ranges such as the Tenzing, Zheng He, Al-Idrisi, Hillary and Baré Montes ranges (Figs. 6, 9, 21–23). Topography indicates the lack of moats or ridges bounding the contacts of the ice sheet with the massifs, and the SP ice deposits embay the gaps between the massifs of Al-Idrisi and Baré Montes massif ranges (Figs. 21 and 22). Surprisingly, the SP ice deposits do not extend flush with the base of the ridge-ring in the northwestern quadrant of the basin. Rather, the ice deposits have a lobate terminal scarp 0.7–1.0 km high and just interior to the range of massifs, and do not fill the 3.5–4.5 km deep trough at the base of the high-standing ridge-ring escarpment described above. The terminal scarp of the ice sheet has a dark reddish coating. The scarp on the edge of the ice sheet is associated with a low rise of ~300 m along the edge of the ice sheet in this area, and slopes on the scarp itself are typically 20–30°, suggestive of viscous lateral flow (Fig. 21).

An interesting area is the narrow trough between the base of the ridge-ring rise and the dark elevated plateau of Baré Montes (Fig. 23). SP ice forms two lobate "fingers" that appear to have flowed in towards each other within this narrow neck but stopped short, leaving the narrowest portion incompletely filled. This trough is depressed 400–500 m relative to the two ice lobes, and would be consistent with lateral flow of SP ice into all areas except those depressions too narrow or shallow to allow a viscous ice to flow.

The base to peak heights of the angular massifs vary from immeasurable (in current DEMs) to ~6.5 km, with a mean height somewhere between 2 and 3 km. The highest peaks are tabulated in Table 3, and in the spirit of "K2" here on Earth are given alphanumeric nicknames. The highest of these, between 5.7 and 6.1 km in height, are comparable to Denali (~5.5 km), one of the highest mountains on Earth base-to-peak, and the central peak of Herschel on Mimas (~7 km). The blocks within the SP ice sheet are likely considerably thicker than observed with some unknown portion partly buried by this ice, which may have thicknesses of several kilometers near the western margins. Those massifs perched on the northwestern rim of Hyecho Palus (Figs. 6 and 9; see next section) have a maximum height of ~5 km and are not buried by SP ice, though they could have buried roots.

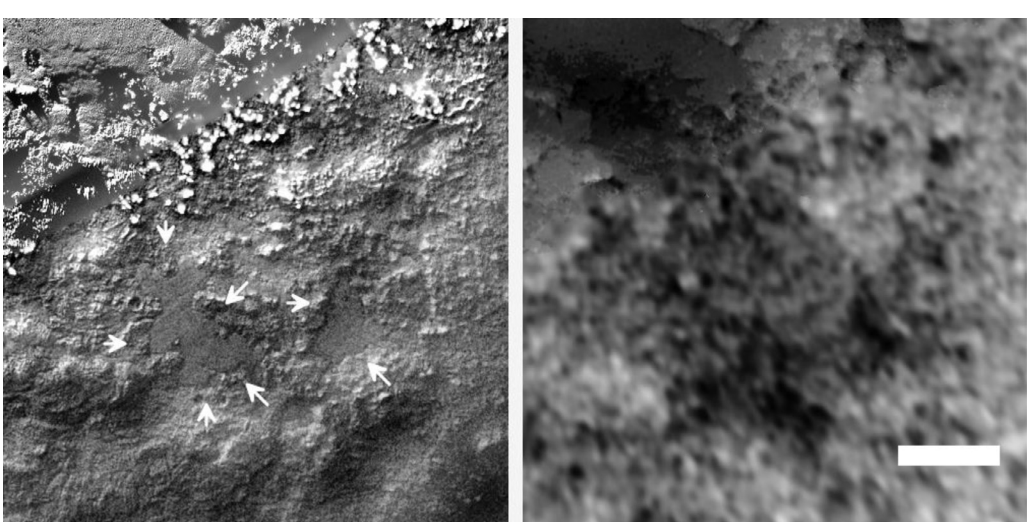

Fig. 20. Section of global color mosaic (left) and DEM (right) showing the southern rim of the Sputnik Planitia basin centered at − 28°, 189° White arrows highlight two units of smooth material (and similar in appearance to the textures of the ice sheet in SP proper to the north) with lobate edges that embay topographic lows. DEM at right shows that these deposits form in a confined topographic low adjacent to the southern edge of SP at top. Area (except upper left) was viewed at high resolution (315 m/pixel) in haze-light. Scene width is ~250 km across; relief shown is + 4 to − 4 km; scale bar is 50 km; centered at 26°S, 189°E.

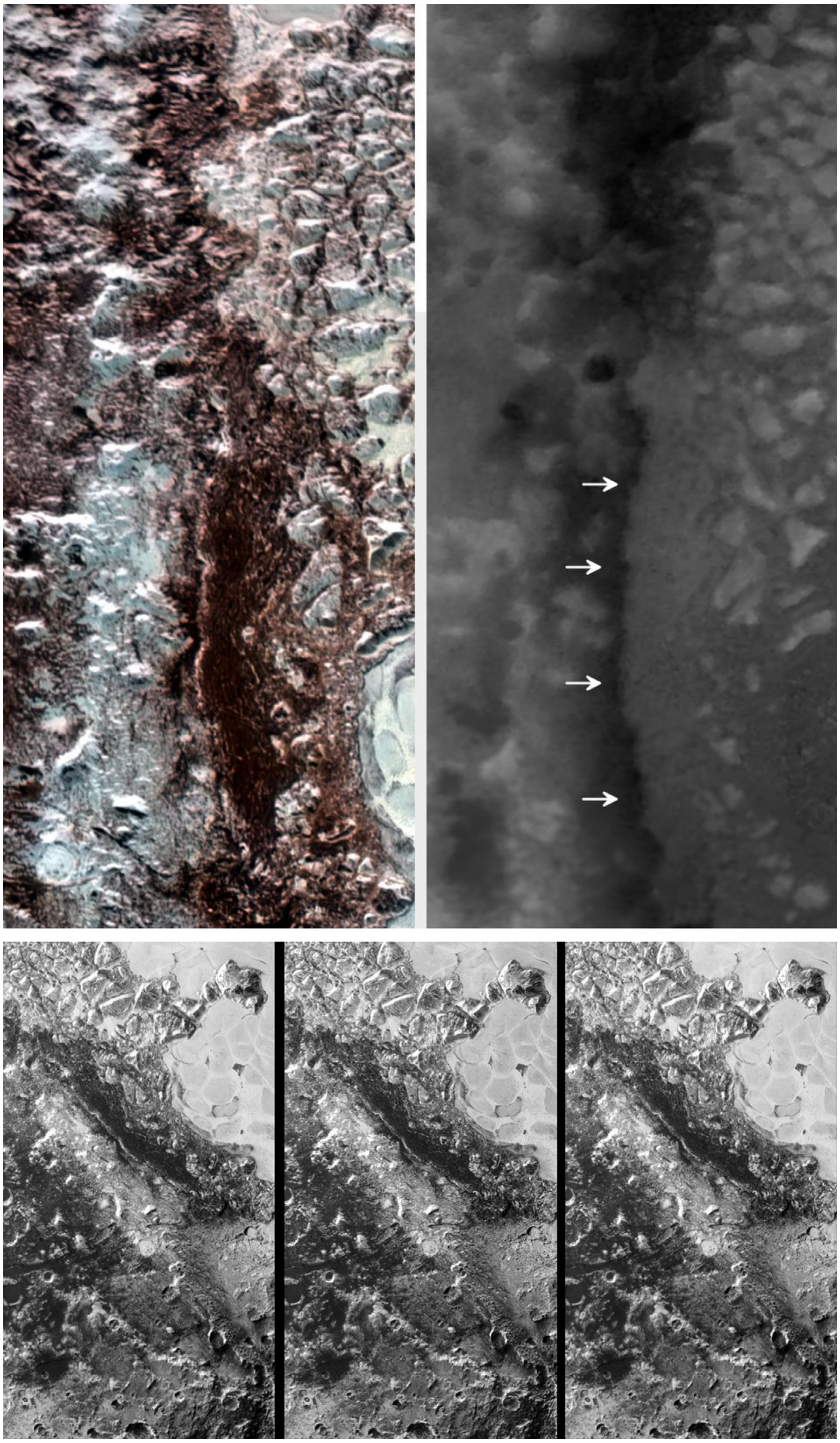

Fig. 21. (a) Section of global color mosaic (left) and DEM (right) showing the western rim of the Sputnik Planitia basin between 20° and 37° latitude. These are among the deepest areas on Pluto. This depressed quasi-linear section is also part of the north-south ridge-and-trough system described in the Tectonics section. The white arrows highlight a prominent scarp that defines the outer edge of the SP ice sheet, which, although relatively dark here, forms a continuous deposit between the angular massifs at right and the main ice sheet itself out-of-view at far right. This scarp is also evident in the slope map of Fig. 8. Scene width is ~125 km across; relief shown is + 4 to − 4 km; centered at 28°N, 151°E. The color version is from the 4-color global mosaic (Fig. 1) and uses MVIC filters "blue", "red" and "CH_4," which provide the greatest color contrast. (b) Stereo pair of region shown in Fig. 21a, highlighting elongate troughs along the edge of SP, angular blocks within SP and other features along the boundary between the ice sheet (upper left) and the elevated highlands to the west (lower right). Image resolutions are 650 and 315 m/pixel. Note that orientation is different to align stereo pair for viewing. Figure format allows user to view in either wall-eyed mode (left-center) or cross-eyed mode (center-right). Red-blue anaglyph version of this figure is available in Supplementary Fig. 3. (For interpretation of the references to color in this figure legend, the reader is referred to the web version of this article.)

Individual blocks in these mountain ranges are typically very angular with steep sides sloping 40–50°, with some exceeding 50° (Fig. 8). Many blocks crest at a point or at a craggy top, others such as the larger blocks within Zheng He and Hillary Montes crest on planar surfaces that resemble mesas (Figs. 22 and 23) which have slopes that do not greatly exceed 10°. Their angular shapes, steep side slopes and occasional flat tops suggest the break-up and mobilization of large blocks of Pluto's outer icy layers, with limited block rotation. The exact mechanism of crustal break-up is unclear but could include disruption of the ice shell during a large impact event, forming a partial inner ring, or post-impact break-up of parts of the basin floor. The angular massifs of Tenzing Montes and those on the northwest edge of Hyecho Palus are all steep-sided and do not have flat-tops, in contrast to those of Zheng He and Hillary Montes.

The mean slopes of the mountainous ranges on Pluto taken as contiguous geologic units (including large blocks and smaller scale interstitial materials) are ~13.6 to ~19°, steeper than any other Pluto terrain types measured (Table 2). These mean slopes are also somewhat

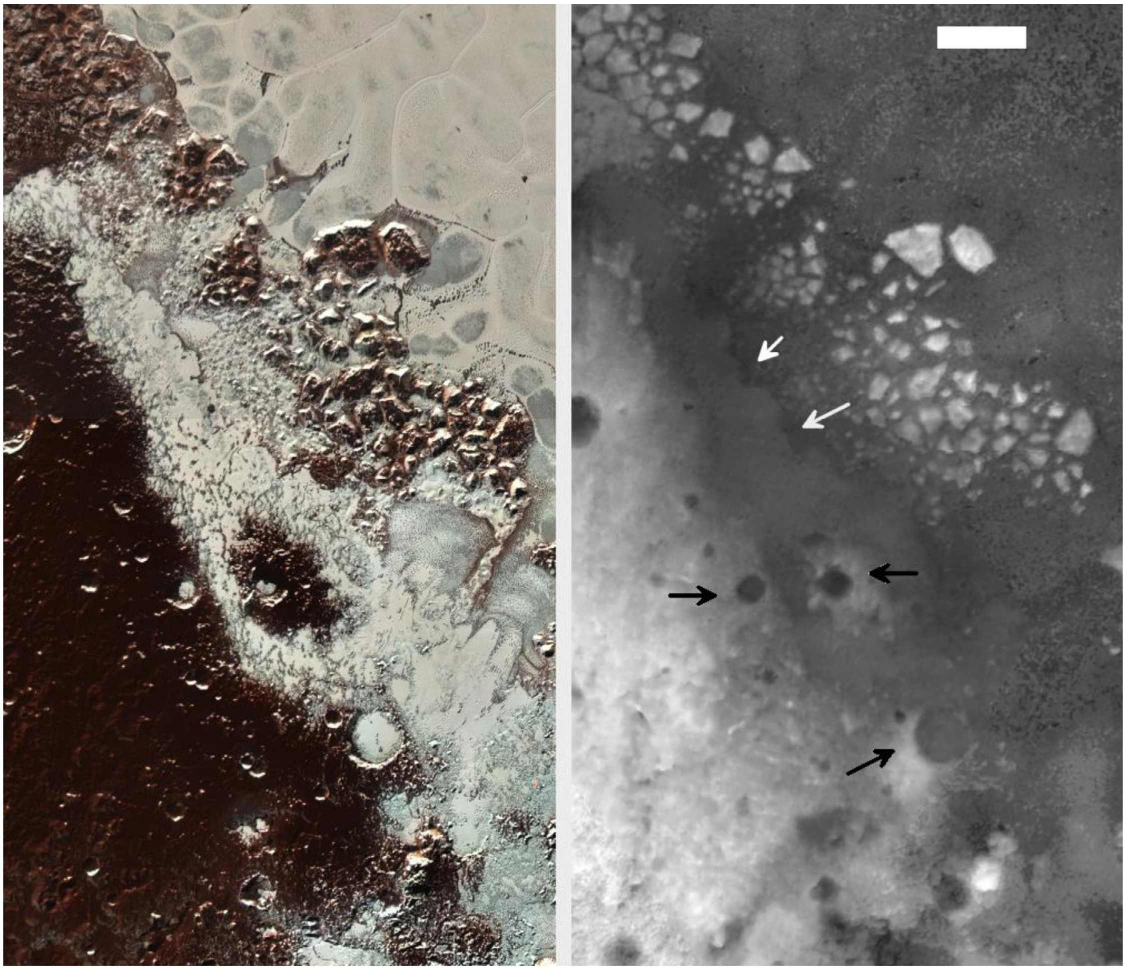

Fig. 22. Section of global color mosaic (left) and DEM (right) showing the equatorial western rim of the Sputnik Planitia basin between − 9° and 14° latitude. Dark arrows highlight several craters that are either partially filled or whose rims are breached and embayed by bright ice materials similar to SP. White arrows highlight a bright ice deposit along the western rim of SP that is elevated 100–300 m above the main ice deposit. These form at similar latitudes to the elevated margin in the southeast margin region shown in Fig. 18. Scene width is ~300 km across; relief shown is + 4 to − 4 km; scale bar is 50 km; centered at 3°N, 165°E. The color version of the image mosaic is from the 4-color global mosaic (Fig. 1) and uses MVIC filters "blue", "red" and "CH_4," which provide the greatest color contrast. (For interpretation of the references to color in this figure legend, the reader is referred to the web version of this article.).

steeper than those observed in potentially analogous chaos units on Europa (e.g., Singer et al., 2017). Schenk (2009) reported only slopes for the highly disrupted matrix material between the larger blocks of Europa chaos, but we have resampled those data here and find that the best resolved chaos units including both blocks and matrix have mean slopes of ~11° to 12.5°, several degrees lower than the values reported here for Pluto's disrupted mountain ranges (Table 2). This difference is magnified even more when it is noted that the Europa slope data were

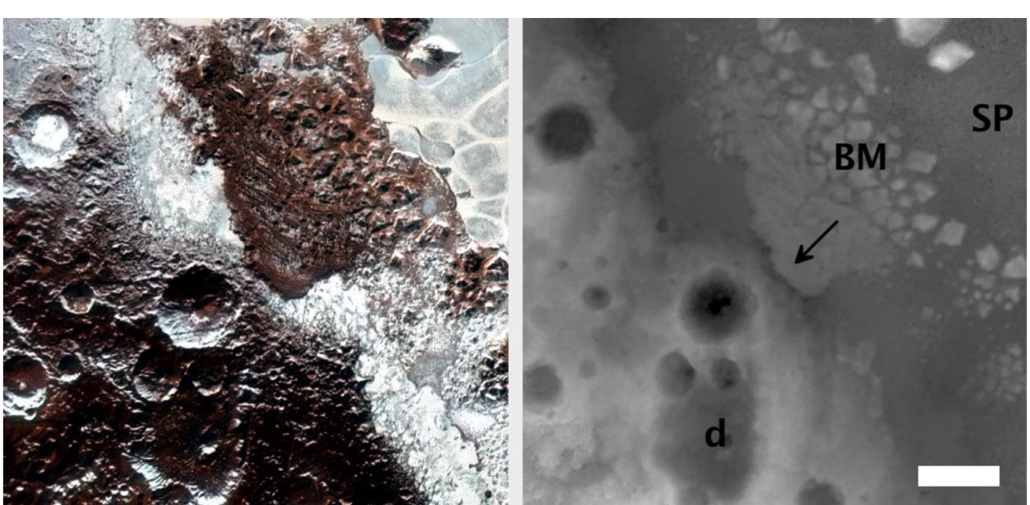

Fig. 23. Section of global color mosaic (left) and DEM (right) showing the western edge of Sputnik Planitia basin and Baré Montes, Pluto. Arrow indicates depressed gap between Baré Montes plateau and SP rim terrains. Note lack of bright material in the gap area. Scene width is ~300 km across; relief shown is + 4 to − 4 km; scale bar is 50 km; centered at 11°N, 157°E. The lower right corner of scene overlaps with upper left corner in Fig. 22. The color version is from the 4-color global mosaic (Fig. 1) and uses MVIC filters "blue", "red" and "CH_4," which provide the greatest color contrast. (For interpretation of the references to color in this figure legend, the reader is referred to the web version of this article.).

Table 3
Heights of some of the tallest massifs on Pluto.

Location	Name of range	Peak name	Height[a], km
− 16.4, 175.6	Tenzing Montes	"T2"[b]	6.2 ± 0.6
− 16.0, 174.9	Tenzing Montes	"T1"	5.7 ± 0.4
− 33.2, 174.8	Piccard Montes (maximum crest)		5.5 ± 2.0
− 16.9, 176.3	Tenzing Montes	"T3"[b]	5.3 ± 0.4
− 12.5, 163.1	NW scarp of Hyecho Palus	"H1"	5.1 ± 0.4
− 21.7, 179.7	Tenzing Montes	"T4"	5.0 ± 0.4
26.2, 159.2	al-Idrisi Montes (south)	"I1"	4.8 ± 0.4
− 22.6, 171.9	Wright Mons (maximum crest)		4.7 ± 1.0
20.5, 159.8	Zheng He Montes (north)	"Z1"	4.6 ± 0.4
− 31.5, 144.4	York Montes (highest)	"Y1"	4.5 ± 0.75
− 19.5, 179.2	Tenzing Montes (south)	"T11"	4.5 ± 0.4
− 20.3, 178.9	Tenzing Montes (south)	"T12"	4.4 ± 0.4
19.0, 160.6	Zheng He Montes (north)	"Z2"	4.4 ± 0.4
19.0, 159.2	Zheng He Montes (north)	"Z3"	4.4 ± 0.4
17.4, 161.3	Zheng He Montes (north)	"Z4"	4.1 ± 0.4
− 18.3, 176.7	Tensing Montes	"T4"	3.6 ± 0.4
− 6.3, 147.0	Enrique Montes	"E1"	3.5 ± 0.75
− 5.7, 173.1	Hillary Montes (south)	"H1"	3.5 ± 0.4

[a] Height measured base-to-crest. In some cases base elevation varied considerable around the massif and values are based on best estimates of elevation of surrounding terrains. Uncertainties reflect variations in base elevation and vertical resolution of DEMs. Only the highest massifs in each range are included in this list.

[b] Massif base unobserved due to flanking massifs; inferred from adjacent terrains.

measured at 40–55 m length-scales, not 1 km scales as on Pluto. Mean slopes on Europa chaos matrix units decrease to < 8° as length scales increase to ~1 km (Schenk, 2009), suggesting a scale difference within chaos units on the two bodies, with Europa chaos being more finely broken up. While slopes on the flanks of blocks in Europa chaos can reach 30–40°, similar to those observed on Pluto, the tops of the Europan blocks are more variable in shape, with some being flat-topped but most being steeper and more angular. Whether this indicates greater degrees of block rotation on Europa remains to be determined. Mean slopes of grooved terrains on Ganymede reach ~20° at 50–200 m scales, but also decrease to < 10° as scales increase to 1 km. Although we do not explore the implications of these data further, other than to infer that different disruption mechanisms are involved (e.g., Schmidt et al., 2011), slope characteristics of terrains on Pluto (Table 2) will be of importance for the comparison of disrupted terrains on these three bodies.

4.5. Tectonic features

The fracture systems Sleipnir and Mwindo Fossae well to the east and Djanggawul Fossae to the west of SP are resolved in the DEM and have relief of several kilometers (Figs. 10 and 11). Closer to SP several curvilinear V-shaped troughs (Moore et al., 2016) are widely distributed across the adjacent terrains east and west of the depression (Fig. 6). These steep-walled fractures are typically 400–800 km long, 10–18 km wide and up to 3 km deep. West of SP (Figs. 8 and 10) these structures are well preserved and cut most if not all features, indicating they formed late in the stratigraphic sequence (Moore et al., 2016). Prominent examples are Virgil Fossae (Fig. 24), which cuts and post-dates the northern rim of Elliot crater (which itself has pristine textures) and the Inanna and Dumuzi Fossa doublet (Fig. 10). Fracture wall scarps have slopes between 35° and 45° over most of their lengths, and locally can reach 55°. Although some mass wasting appears to have occurred along the base of these scarps, the walls of these structures are largely intact and show no indications of significant scarp retreat or failure along their rim crest (Fig. 24), despite the steep high slopes. These pristine fractures most likely post-date formation of the highly degraded SP basin by a significant duration and may be a tectonic response to mass loading or polar wander stresses induced by the ancient SP basin or the ice sheet deposited within it (Nimmo et al., 2016; Keane et al., 2016). Why there should be a significant time delay in reorientation is unclear.

Several steep-walled troughs occur within the elevated glaciated plains of eastern Tombaugh Regio (Figs. 11 and 12). These have a similar radial distribution relative to SP, and are likely part of the same tectonic regime, but have undergone a significant degree of surface modification related to the glacial style erosion across this terrain (Howard et al., 2017b). If the eastern Tombaugh Regio graben formed in the same epoch as the western examples, as seems likely, the greater degree of erosion implies that, while younger than the SP basin, this fracturing event predates the current epoch of glacial activity. Topography and mapping indicate that these bladed terrains are superposed on these eastern graben and the Mwindo and Sleipnir Fossae fractures to their north (Figs. 12 and 14), indicating that bladed terrains are younger than this putatively SP-related fracturing episode.

Several of the walled V-shaped troughs west of SP display differential relief between their opposing walls. At its widest, the walls of Virgil Fossae in Fig. 24 are ~12 km across and 2.8 km high on its southern wall but only ~1.8 km high on it northern wall, indicating up to 1.4 km of vertical displacement, or "throw," between the crustal blocks on either side. The Inanna and Dumuzi Fossa fractures to the north also show vertical offsets of 0.5 to 1.0 km (Fig. 10), also on the southern side though of less magnitude than at Virgil.

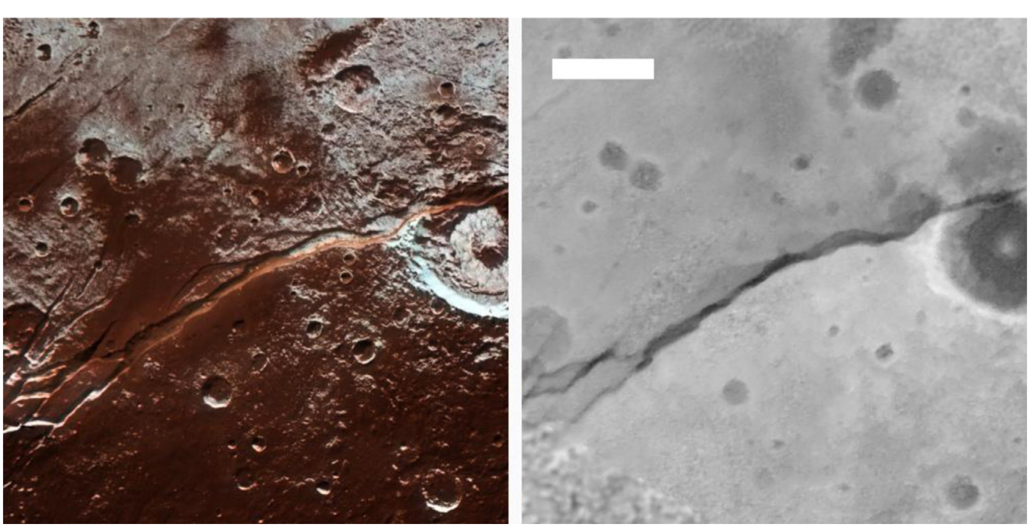

Fig. 24. Virgil Fossae, Pluto, from global color mosaic (left) and DEM (right). Note pristine morphology and relief, and higher elevation on south flank of fracture (to bottom) compared to north flank. Elliot is the 90-km crater at right edge of scene. Scene width is ~300 km across; relief shown is + 4 to − 4 km; scale bar is 50 km; centered at 11°N, 132°E. The color version is from the 4-color global mosaic (Fig. 1) and uses MVIC filters "blue", "red" and "CH_4," which provide the greatest color contrast. (For interpretation of the references to color in this figure legend, the reader is referred to the web version of this article.).

There is no apparent evidence in the topography (Fig 11c and 24), for flexural rift-flank uplifts along the sides of any of the V-shaped graben, a phenomenon frequently observed in terrestrial extensional settings (e.g. Brown and Phillips, 1999). As at the large rift valleys on Mars (Barnett and Nimmo, 2002), this absence of flank uplift as well as the vertical throw across them indicates a relatively thick elastic layer for Pluto at the time of formation. If these fractures are associated with SP-induced polar wander (Nimmo et al., 2016; Keane et al., 2016), then Pluto was likely rather cold at the time.

4.6. Tectonic features: the great north-south ridge-trough system

One of the most dramatic physiographic features on Pluto discovered in the topographic mapping (aside from Sputnik Planitia and the volcanic province associated with Hyecho Palus described in the next section) is a broad linear band of troughs, ridges, elevated plateaus and elongate depressions trending nearly north-south between the 145° − 165°E meridians (Figs. 9 and 25). Visible in the panchromatic global mosaic as isolated ridges and linear scarps, this structure is prominent in the global DEM as a broad continuous feature following a great circle. This complex structure is ~300–400 km wide over most of its length. The mapped portion extends 3200 km, or ≥ 40% of Pluto's circumference (Fig. 25), but its full length is unknown. The northern end becomes undefined in the lower-resolution imaging on the sub-Charon hemisphere. No discrete topographic features are evident in the low-resolution mapping of the equatorial regions of the sub-Charon hemisphere (Fig. 1) but the portions mapped at high resolution show few albedo signatures, suggesting that brightness patterns are insufficient at low resolution to detect this feature. The southern portion extends into the haze-lit region down to at least − 50° latitude where it fades with the illumination, indicating that this tectonic system extends well into the dark southern hemisphere for an additional unknown distance.

Although significantly eroded and modified, the basic components of this gigantic feature can be ascertained. The system is comprised of numerous parallel elements that change character as the system trends from the southern hemisphere to the north pole and beyond (Fig. 25). This complex geologic system is strongly lineated in the direction of its length and can be divided broadly into 3 somewhat different physiographic sections. Though locally modified, the section of the "ridge-trough" system (lacking a better name) between − 50° and 10° latitude may be the best preserved (Fig. 25). This section overlaps with the easternmost portion of the dark Cthulhu Macula albedo feature. It is also cut to the north by the western boundary of Sputnik Planitia north of ~10° latitude and likely extends beneath the SP ice sheet. This section is largely comprised of an elevated plateau region ~400 km wide and is characterized by several parallel components with a general north-south linear texture. The western edge is formed by an eroded linear trough ~1200 km long, up to 100 km wide and roughly 1–1.5 km deep. Several N-S trending linear ridges (Figs. 9, 25, 26 and 27) are easily recognized despite valley formation eroding their flanks. The most prominent of these linear mountain ranges are the York Montes range to the south (near − 30°, 145°; Fig. 27) and the narrow 2.5-to-3.5-km-high Enrique Montes (at − 5.5°, 147°), which is ~100 km long and ~25 km wide (Fig 26). The upper 1–1.5 km of the Enrique Montes ridge is covered in a bright CH_4 frost or ice (Grundy et al., 2016). This and related ridges are significantly eroded by glacial valley networks (e.g., Howard et al., 2017b) common at these latitudes (Figs. 26 and 27). The ridges of York Montes are deeply eroded by several east-west trending valleys 2–4 km deep. Some of these valleys appear to be carrying sediment to the lower elevations along the trough that marks the western edge of this system (Fig. 27).

The integrated DEM indicates that the plateaus of the southern section are variable in elevation (Fig. 27), with a mean height relative to Pluto mean radius of ~1.5 ± 1.0 km. To the south, parts of the plateau rises in altitude to ~4 km above the mean radius. Parts of this plateau rise to elevations nearly as high as parts of the bladed terrain to the east (Figs. 6 and 14), the highest geologic unit on Pluto. Several sinuous channels are also evident within this plateau (Fig. 27). The largest of the York Montes massifs rise up to 4.5 km above local surfaces and are among the highest standing individual features relative to Pluto mean radius. The higher standing southern section of the plateau also corresponds roughly to the southward transition from the darker reddish Cthulhu Macula to brighter and less red surfaces (Fig. 27), suggesting that while latitude is an important control on the deposition of dark material in this region, that it is modulated to some degree by

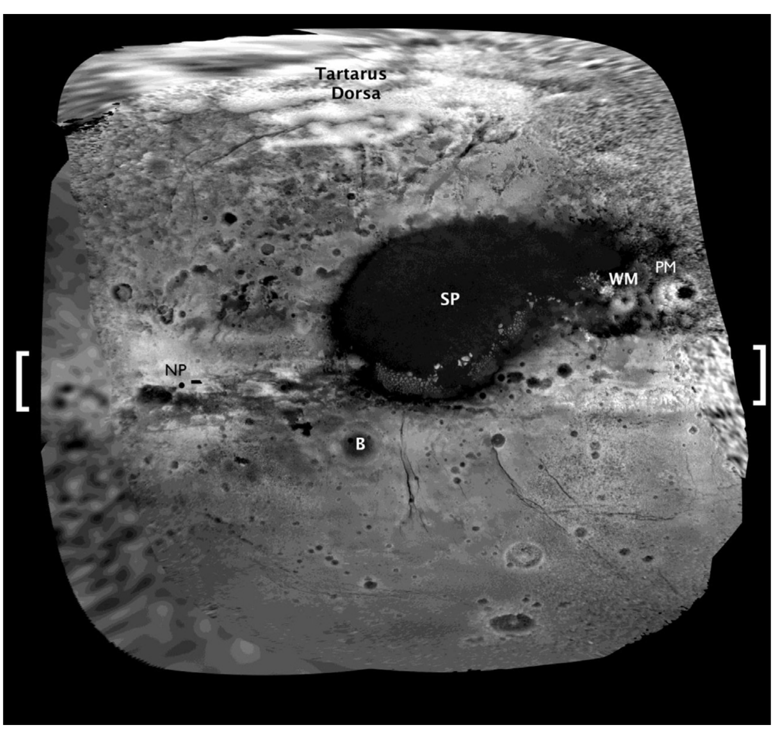

Fig. 25. Reprojection of Pluto integrated DEM in oblique simple cylindrical projection, rotated so that the north-south ridge-trough system described in text tracks horizontally across the 'paleo-equator' of the map. The map (and ridge-trough system) extends approximately one half of Pluto's circumference. The illuminated pole is at (NP). Although degraded, the ridge-trough system forms a broad band of elevated striated or ridged material along the central third of the image (between brackets), defined by a narrow flanking trough. The central section of this system is either bounded or cut by Sputnik Planitia, or the depressed plains of Hyecho Palus containing Wright (W) and Piccard Mons. The ridge-trough system thus forms a great circle, with the pole of the great circle at the top and bottom of this map projection. All features parallel to it would form horizontal lines. Note also the V-shaped trough systems extending above and below the SP basin in this projection. The elevated plateaus of Tartarus Dorsa at top are located near to one of the poles of the great circle. View is centered at + 40°, 157°E. Relief shown is + 4 to − 4 km.

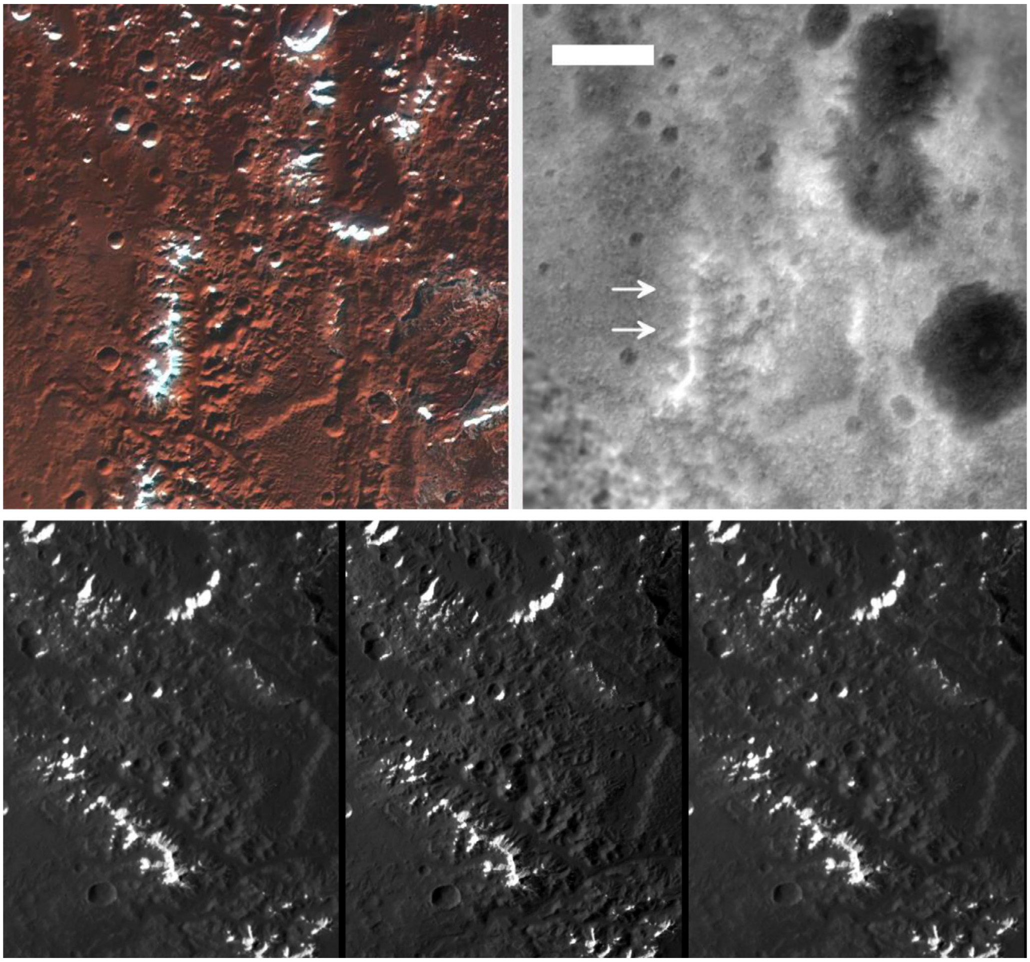

Fig. 26. (a) Section of global color mosaic (left) and DEM (right) showing the Enrique Montes. Bright ices are evident on the crest of Enrique Montes and pole-facing slopes of crater rims in this region. Note valley networks incising Enrique Montes and surrounding areas. Several shallow walled depressions and elongate deep craters are evident at center and upper right. North is to the top. Scene width is ~300 km across; relief shown is + 4 to − 4 km; scale bar is 50 km; centered at 3°S, 149°E. The color version of the image mosaic is from the 4-color global mosaic (Fig. 1) and uses MVIC filters "blue", "red" and "CH_4," which provide the greatest color contrast. (b) Stereo pair of region shown in a, highlighting valley networks and the bright methane 'frost'-covered and eroded Enrique Montes ridge. Image resolutions are 650 and 315 m/pixel. Note that orientation is different to align stereo pair for viewing. Figure format allows user to view in either wall-eyed mode (left-center) or cross-eyed mode (center-right). Red-blue anaglyph version of this figure is available in Supplementary Fig. 4. (For interpretation of the references to color in this figure legend, the reader is referred to the web version of this article.)

elevation.

Between ~0° and ~40° latitude, the ridge-trough system is narrowest (Fig. 28), with most of the system inferred to track beneath the SP ice sheet. Here we observe essentially a well-defined curvilinear walled depression, or graben, on the order of 60 km wide and 1–2 km deep (Fig. 28). In some areas the graben wall has a cuspate or sinuous margin, whether due to formation or wall collapse processes is not known. This trough is likely a continuation of the west-flanking linear depression observed to the south (Fig. 25). Topographically the graben continues across the broad raised rim surrounding SP and downward into the topographic SP depression between the outer ridge-ring and the ice sheet (Fig. 21), becoming tangent to and thus part of the inner escarpment of the depression. This sequence indicates that at least the last deformation on the trough occurred after the SP depression formed (presumably during a large impact event) but before the bright ice sheet covered this section of SP.

In the illuminated north polar region, the ridge-trough system is again 350–400 km wide and more complex in structure. A prominent trough ~70–150 km wide and 2–5 km deep (Fig. 15) cuts across the polar dome, and forms the deepest portion of the ridge-trough system. This main trough bifurcates and splits in complex fashion along its length to form several shorter irregularly shaped walled depressions. In some areas, a remnant (or eroded) parallel linear fabric of minor scarps and ridges can be ascertained (Fig. 15). The main trough has a smooth flat floor in some sections, suggesting possible sediment deposition due to the erosional desiccation of the uplifted polar plateau and valley walls prevalent throughout this region. Areas of the polar region on the sub-Charon hemisphere were also observed in stereo at low spatial resolution, and several dark-floored irregular depressions can be identified in the area centered on 63°, 243°E. These are partially resolved in the low-resolution DEM of that region as being a few kilometers deep, indicating that the trough system may continue well into the sub-Charon hemisphere but with a different, less linear character. These dark depressions suggest that other dark irregularly shaped features (Fig. 1) on the sub-Charon hemisphere in the global mosaic (centered on 0° longitude) may also be depressed. Examination of limb profiles in medium-resolution departure images indicates an unusually rugged topography near 320–340°W longitude at ~30° latitude, which could also be interpreted as an extension of the northern section of the system.

Irregular depressions are scattered along the length of north-south ridge-trough system. The southern section below the equator occurs within Cthulhu Macula where numerous ordinary looking impact craters up to ~100 km across are located, but several odd elongate depressions as well (Figs. 26 and 27). These are irregular or amoeboid in shape with lobate reentrants. The largest of these irregular walled depressions, at − 14°, 153°E and at − 29°, 163°E (Figs. 26–28), are roughly 30–125 km in size and 2.5 to 3.5 km deep and likely not of impact origin (Fig. 28). A second smaller irregular non-impact depression occurs. Both examples are elongate in the same direction as the ridge-trough system. North of these features at ~3°, 153°, are two large deep basins of ovoid shape, also elongate in the direction of the ridge-trough system (Fig. 28). These two deep depressions are more plausibly impact related, their elongate shapes possibly due to oblique or multiple impactors, but the coincidence that they lie within and are elongate in the same direction as the great north-south ridge-trough system suggests they are not necessarily impact related. Similar elongate depressions also appear within the ridge-trough system in the north polar region. The origins of these elongate and irregular depressions are not yet clear but explosive volcanism or other similar processes associated

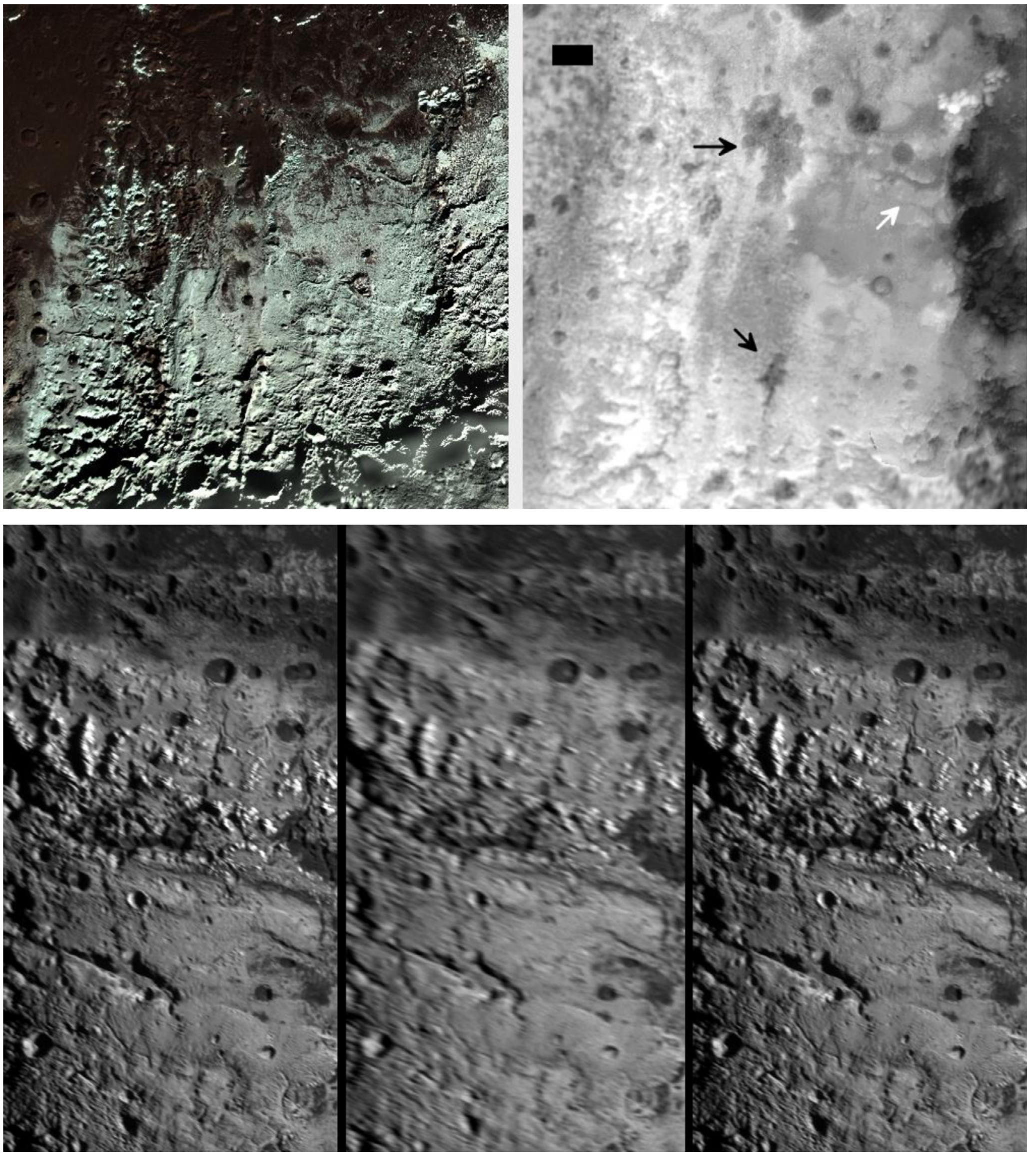

Fig. 27. (a) Section of global color mosaic (left) and DEM (right) showing the eroded ridges of York Montes (lower left), erosional valley networks (white arrow), and irregular walled depressions (dark arrows) associated with the southern most illuminated portions of the global ridge-trough system shown in Fig. 25. North is to the top. Scene width is ~500 km across; relief shown is + 4 to − 4 km; black scale bar is 50 km; centered at 21°S, 153°E. The color version is from the 4-color global mosaic (Fig. 1) and uses MVIC filters "blue", "red" and "CH_4," which provide the greatest color contrast. (b) Stereo pair of region shown in a, highlighting erosional valley networks along the southern raised plateau of the north-south ridge-trough system on Pluto. Lower-lying plains of Cthulhu Macula are at top; north is to the right. Image resolutions are 875 and 650 m/pixel. Note that orientation is different to align stereo pair for viewing, and a slight shift in solar illumination between exposures. Figure format allows user to view in either wall-eyed mode (left-center) or cross-eyed mode (center-right). Red-blue anaglyph version of this figure is available in Supplementary Fig. 5. (For interpretation of the references to color in this figure legend, the reader is referred to the web version of this article.)

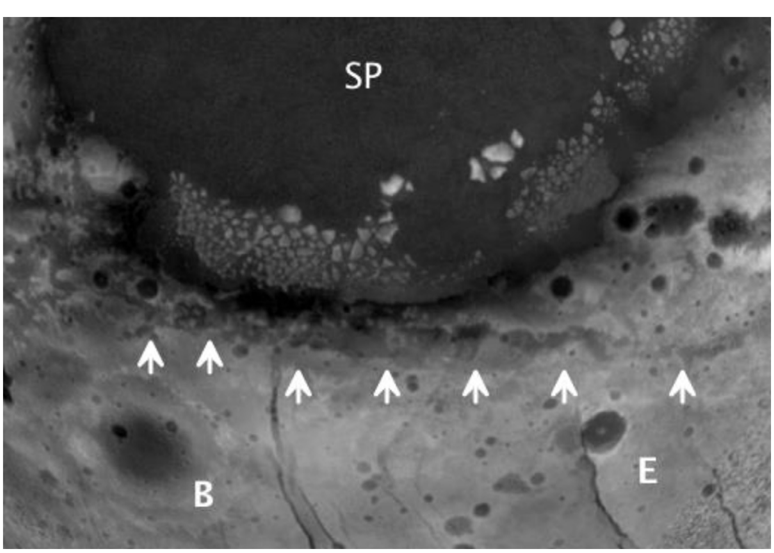

Fig. 28. Section of DEM (Fig. 6) showing the central section of the global ridge-trough system shown in Fig. 25. Arrows indicate location of complex walled trough forming the western boundary of the ridge-trough system, which continues to the left and right in this perspective. Craters Burney (B) and Elliot (E) are highlighted. North is to the left in this orthographic projection, similar to Fig. 25. Scene width is ~1000 km across; relief shown is + 4 to − 4 km; centered at 27°N, 152°E.

with a large tectonic system cannot be ruled out, nor can lateral erosion of older impact craters or other areas of weakened or damaged crust. How impact craters can be deepened by erosion is unclear unless more volatile layers than those on the surface are exposed under the floors of such craters.

4.7. Volcanic terrains

One of the most distinctive terrains identified in the high-resolution mapping area of Pluto are the annular massifs Wright and Piccard Mons (Fig. 29; e.g., Moore et al., 2016) and surrounding features. The two massifs lie within a partially enclosed 400 × 700 km-wide depression Hyecho Palus (Figs. 6, 9 and 29) flanking the southwestern edge of Sputnik Planitia. This walled plain and the features within it form a distinct topographic/physiographic province on Pluto (Fig. 9). Although other interpretations are plausible, these massifs are likely constructional and considered putative volcanic terrains (e.g., Moore et al., 2016; Singer et al., 2016) due to their positive relief, young surface ages, and distinctive morphologies. At both Wright and Piccard Mons the heights of the rim and depths of the central structures all well exceed those of impact craters elsewhere on Pluto and are clearly not of impact origin (Moore et al., 2016).

The Hyecho Palus plain is depressed 1–2 km below mean radius and is bounded by the ice sheet of SP on the east and by a scarp several kilometers high on the west (Figs. 29 and 30). This scarp also trends parallel to and may have been influenced by the linear tectonic fabric of the N-S ridge-trough system described above. The southern margin of Hyecho Palus is located in the haze-lit zone but there are indications of a possible southern rim scarp in the images. The eastern margin grades into the smooth ice sheet of SP proper and is at comparable elevations to it.

Wright Mons (− 21°, 173° E) was viewed in direct sunlight and in stereo at resolutions from ~0.84 to 0.25 km/pixels (Fig. 31). Although symmetric in planform, the eastern half of this edifice is slightly lower than the western section. The main edifice is 155-km-wide and 3.5–4.7 km high and features a steep-walled central depression ~45 km wide and 3.5–4.5 km deep with respect to the uneven annular crest of the massif (Fig. 31). The outer flanks of this annular massif slope more gently outward and are characterized by hundreds of overlapping and closely spaced smaller mounds 10–15 km wide and hundereds meters high (Fig. 31).

Piccard Mons was viewed in sunlight in several images at 2–4 km pixel scales (e.g., 0,299,127,172), which show it to be a walled depression with raised rim, giving the initial impression of a poorly resolved impact crater. Piccard Mons was in darkness at encounter but was viewed in stereo in haze-light at 0.475 and 0.315 km/pixel resolutions (Fig. 32). Although the derived stereo-DEM is relatively noisy compared to sunlit regions, these data together with the stereo images reveal that Piccard Mons is a composite structure 200 by 280 km across comprised of a 100-120-km-wide walled central depression and its

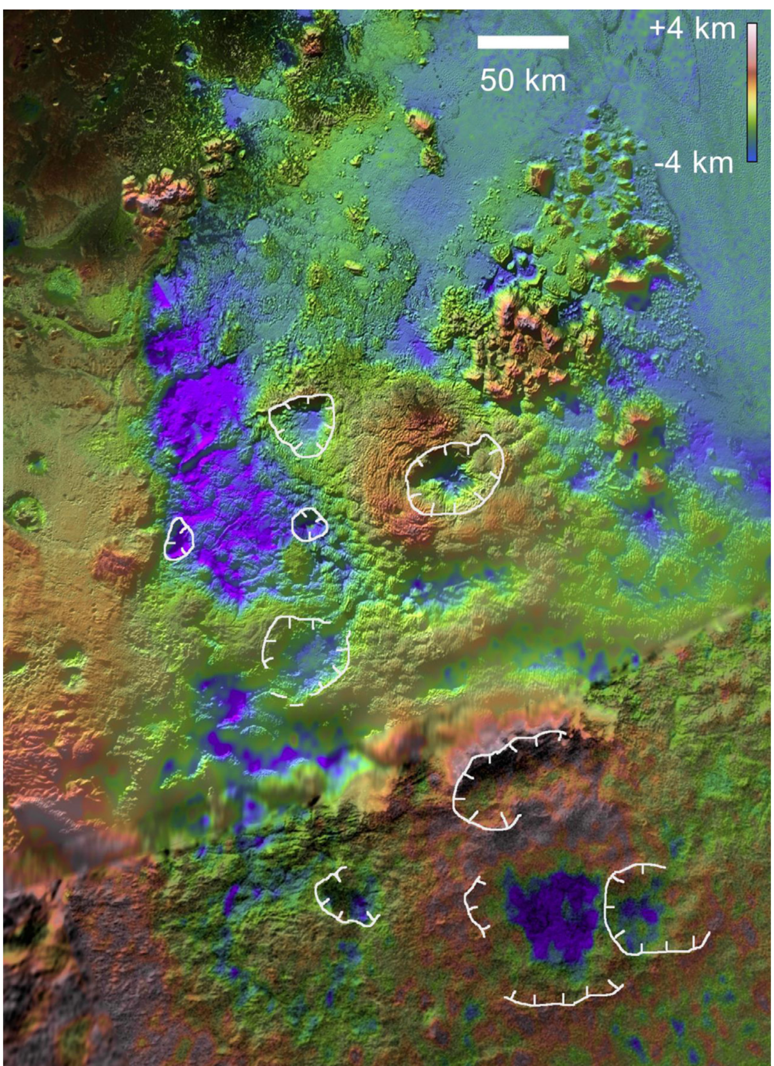

Fig. 29. Section of global basemap and DEM (Fig. 1) showing constructional edifices southwest of Sputnik Planitia (visible in upper right quadrant). Area shown includes the depressed plains informally known as Hyecho Palus. Wright and Piccard Mons are at center and bottom center. Hatched white lines show rims of major walled depressions and edifices. Various additional domes, ridges, and constructional features are evident. Scene width is ~500 km across; centered at 24°S, 171°E. The online color version is color-coded from data in Fig. 6 to show elevation. (For interpretation of the references to color in this figure legend, the reader is referred to the web version of this article.).

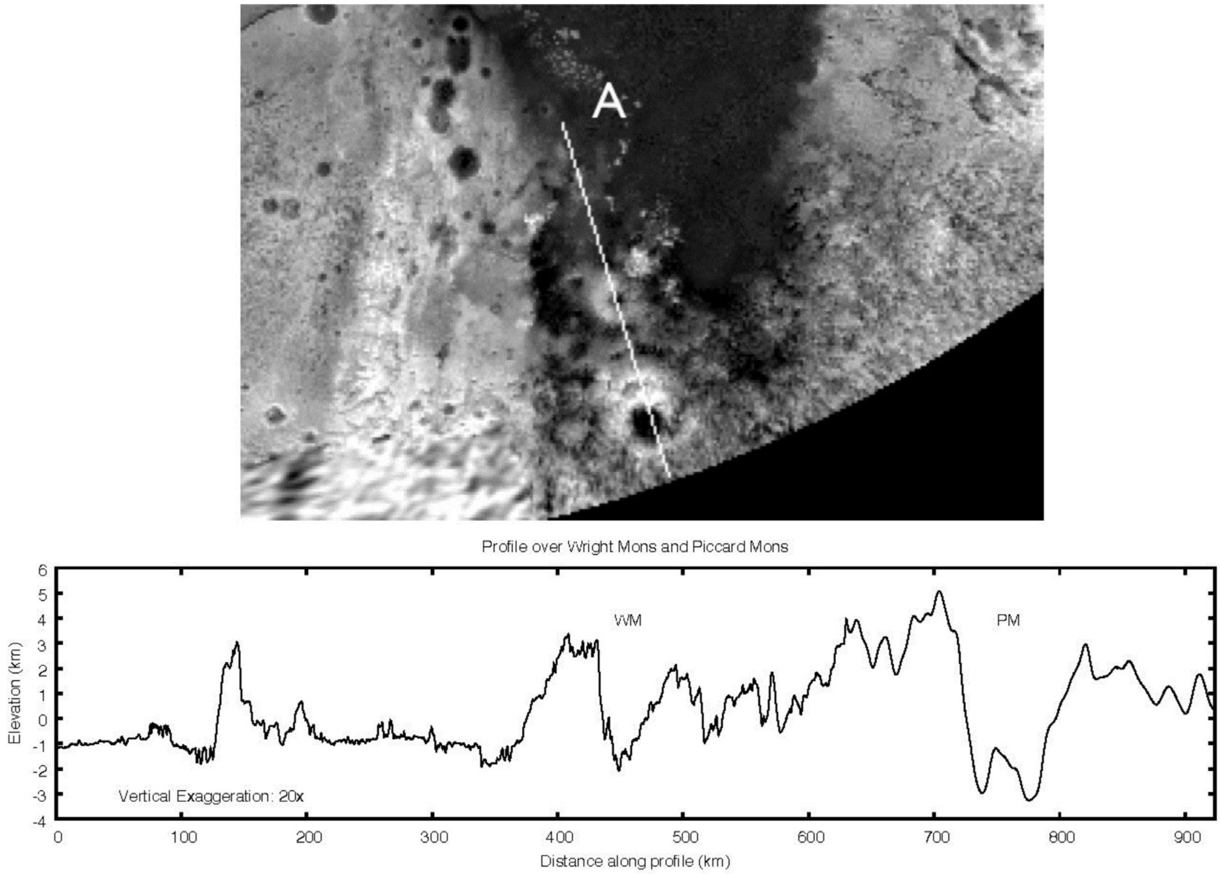

Fig. 30. Profile across Hyecho Palus, highlighting the edifices Wright Mons (WM) and Piccard Mons (PM). See inset map for locations.

flanking rims and several smaller overlapping or nested arcuate ridges and circular structures. Two large nested arcuate plateaus both ~5.5 ± 0.5 km high (above mean radius) or 5.0 ± 0.5 km (above the surrounding plains) form the northern flank of Piccard Mons complex (Fig. 32). These high ridges or plateaus have some of the knobby-mounded texture observed at Wright Mons but this seems to fade toward the south where it becomes craggier in appearance (Fig. 30). The southern "rim" scarp is lower, rising only ~1 km above surrounding terrains. The floor of the depression is ~5.8 ± 0.5 km deep with respect to mean Pluto radius, giving a maximum relief of ~11 km from northern rim crest to the floor of the depression, easily the greatest local relief in the DEM mapping area.

Two smaller quasi-circular depressions 45 –65 km across flank the central depression of Piccard Mons to the east and west. The eastern depression cuts the eastern wall scarp of the Piccard Mons central depression (Figs. 29 and 32). The floor of the central depression, as well as the western smaller depression (Fig. 32) features a set of sinuous narrow dark flow-like features (or possibly fractures). A few of these dark features appear to extend up the walls of the depression. Their sinuous merging patterns suggest these could be discrete lava or debris flows, but they appear to have limited relief.

In contrast to the contiguous ice sheet across Sputnik Planitia, which has uniformly low relief at these latitudes, the relief and surface textures of Hyecho Palus are quite variable and locally rugged (Fig. 30) with a mean elevation of ~1.2 km below mean radius but overall relief of at least 3 km (excluding the Wright and Piccard Mons edifices). Isolated lobes and detached outcrops of smooth bright material similar to SP occur within Hyecho Palus and at various topographic levels, especially in higher standing parts of northern Hyecho Palus. Most of the surface of Hyecho Palus is not covered by SP-like material, however, and features either knobby or fractured rolling plains or the mounded textures observed on the flanks of Wright and Piccard Mons. The lowest portions of Hyecho Palus occur along its western margin along the base of the bounding scarp, where rolling fractured and knobby units are depressed 3–4.5 km relative to Pluto mean radius. The plateau to the west is at ~1 km elevation, resulting in up to 5 km of local relief along the western scarp.

Numerous quasi-circular non-impact walled depressions 30–40 km wide are mapped within Hyecho Palus (Fig. 30). Some of these depressions form on asymmetric topographic edifices up to a few kilometers high and appear to be smaller versions of Piccard and Wright Mons. Several low rises 1-3-km high and 30–50 km across also occur within Hyecho Palus and have not been modified by these quasi-circular walled depressions, and possibly to the east (Fig. 3). Small-scale fracture networks also occur in the haze-lit zone across much of Hyecho Palus (Fig. 29). These features suggest that a series of related and complex resurfacing and tectono-volcanic events have occurred across the entire Hyecho Palus depressed plain (e.g., Singer et al., 2016).

5. Discussion and summary

5.1. Global topographic characteristics of Pluto

New Horizons has provided a spectacular reconnaissance data set for the Pluto system, including global integrated maps of morphology and visible and near-IR color of the illuminated surface (Figs. 1 and 3) as well as a topographic map for almost the entire hemisphere viewed on the day of the encounter in July 2015 (Fig. 6). The global base maps in four colors covering ~78% of the surface are essentially maps of normal reflectance (normalized to 15° phase angle) and include images that vary in resolution from ~30 to 0.315 km/pixel and include some areas between − 35° and − 56° latitude that were illumined only by

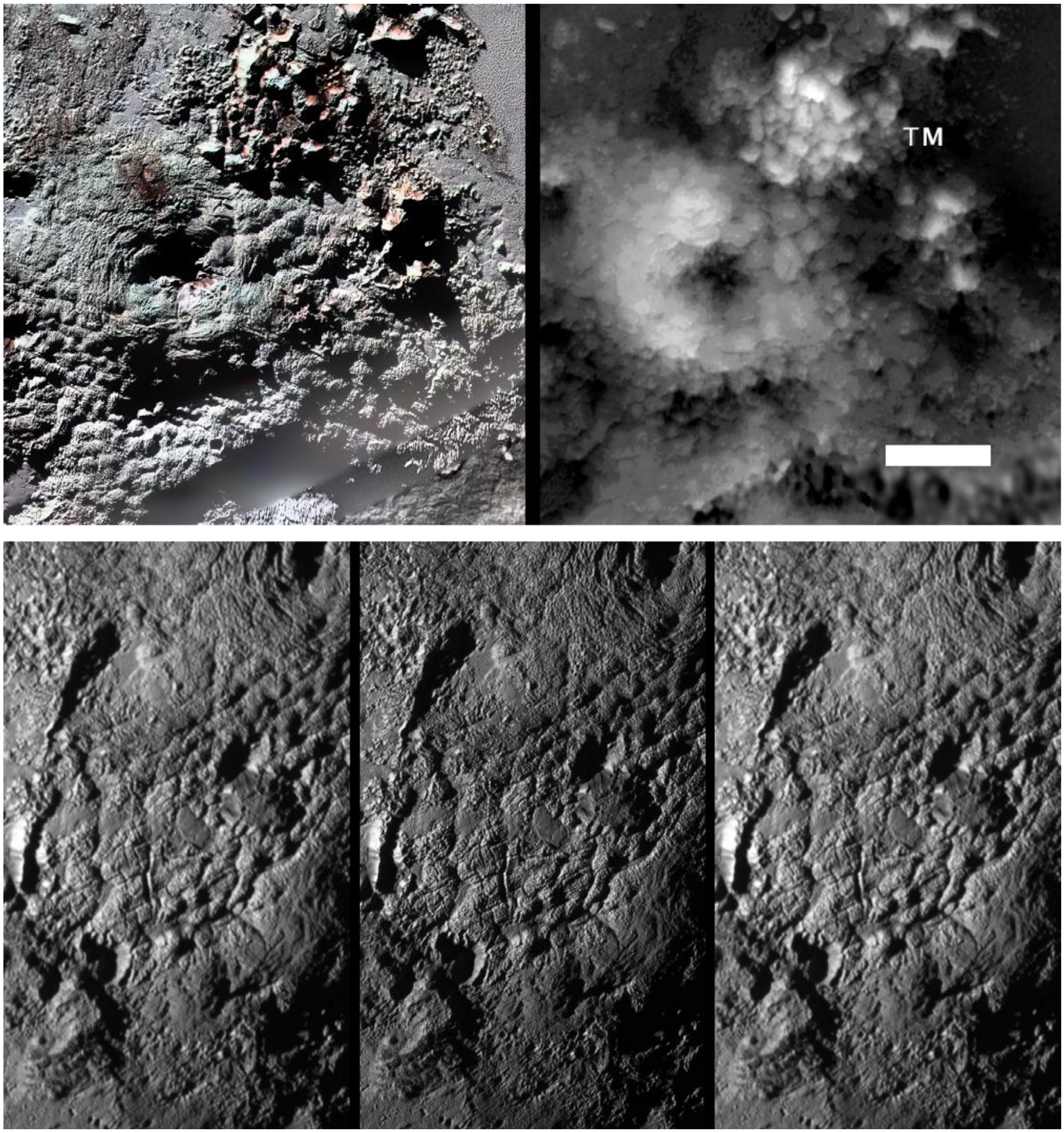

Fig. 31. (a) Annular massif of Wright Mons (center left) from global color mosaic (left) and DEM (right). Tenzing Montes (TM) are due east and northeast of Wright Mons. The Tenzing Montes peaks are the highest base-to-crest massifs known on Pluto (Table 3). Scene width is ~270 km across; relief shown is + 4 to − 4 km; scale bar is 50 km; centered at 21°S, 175°E. The color version is from the 4-color global mosaic (Fig. 1) and uses MVIC filters "blue", "red" and "CH_4," which provide the greatest color contrast. (For interpretation of the references to color in this figure legend, the reader is referred to the web version of this article.). (b) Stereo pair along southwest edge of Hyecho Palus showing knobby morphology and scarps with Hyecho Palus. At upper right is part of Wright Mons show in a, showing terrains immediately to the west. Image resolutions are 650 and 315 m/pixel. Note that orientation is different to align stereo pair for viewing. Figure format allows user to view in either wall-eyed mode (left-center) or cross-eyed mode (center-right). Red-blue anaglyph version of this figure is available in Supplementary Fig. 6. (For interpretation of the references to color in this figure legend, the reader is referred to the web version of this article.)

light scattered by atmospheric haze. These maps are distinct from but comparable to the albedo maps of Pluto derived by Buratti et al. (2017). Although the published topographic map (or DEM) only covers the encounter hemisphere (~42% of the total surface), it is of high quality except for a few areas where the DEM is somewhat noisier (e.g., Cthulhu Macula and parts of Sputnik Planitia). Some residual concerns remain with regard to absolute elevations with respect to the global mean radius currently estimated at 1188.3 ± 1.6 km (Nimmo et al., 2017), mainly due to weakly constrained geometric distortions related to the necessary use of line scan images. Hence, comparison of relative elevations of different terrains should be taken as provisional, until confirmed.

Pluto is rich in geologic (Moore et al., 2016) and topographic diversity, and is dominated by several major features that either disrupt or replace the smooth and eroded plains that cover the majority of the mapped surface. The extended topographic mapping of ~42% of Pluto allows us to characterize its global relief and the topographic characteristics of the major geologic terrain types or provinces. Major features (Fig. 9) included high-standing bladed terrain plateaus (forming a 600-km-wide unit), a broad 600-km-wide and 2–3 km high dome at the north pole, the annular 4–8 km high candidate volcanic edifices Wright and Piccard Montes and the complex low plain in which they formed, the > 3200 km long north-south ridge-trough system along the 152–155° meridian, and ~2.0 km deep 1200-to-2000-km-wide Sputnik Planitia depression (and enclosed ice sheet), a putative ancient impact basin.

The hypsogram of Pluto's topography (Fig. 33) in the DEM mapping area is strongly bimodal, a unique feature reminiscent of Earth and

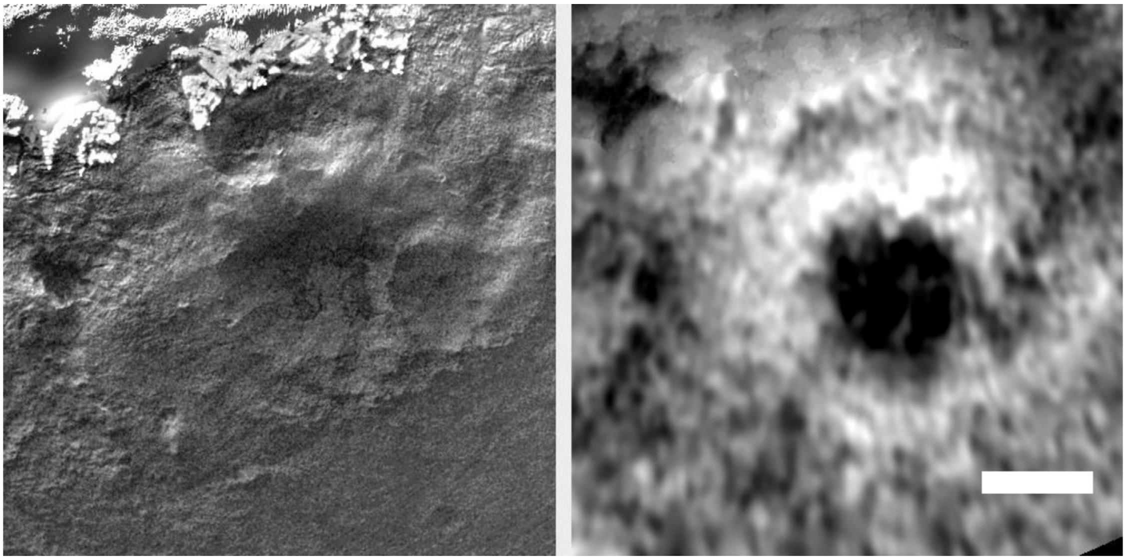

Fig. 32. Composite annular structure Piccard Mons (center) from global color mosaic (left) and DEM (right). All of this area was imaged while illuminated by light scattered from atmospheric haze, except the bright sunlit massifs at top. Note dark ribbon-like features on the floor of Piccard Mons and the small dark-floored circular rimmed depression at left. Scene width is ∼240 km across; relief shown is + 4 to − 4 km; scale bar is 50 km; centered at 36°S, 175°E.

Mars. The two peaks are at − 0.01 km elevation, which represents the mean of all terrain types (except SP), and at − 2.0 km, the mean elevation of Sputnik Planitia relative to Pluto mean. (Note that these values are subject to change by as much as 500 m pending ongoing re-evaluation of the geodetic shape of Pluto.) The hypsogram of Sputnik Planitia is quite narrow and symmetric. The topography of all non-SP terrains is dominated by the broad moderately cratered plains east and west of SP and is also fairly symmetric with relatively though less narrow peak, consistent with the impression from the DEM that most of Pluto's surface has only a few regional-scale deviations in relief greater than a few kilometers, such as the polar dome (Fig. 12) and bladed terrains (Fig. 14).

We isolate the major terrains on Pluto for comparison (Fig. 33; Table 4). The hypsograms for the plains east and west of SP are very

Table 4
Topographic characteristics of terrain types on Pluto.

Terrain	*Area*	*Mean*	*Std. dev.*	*Variance*	*Skew*	*Median*	*Mode*
Pluto (all)	8.11	−0.02	1.29	1.67	0.01	−0.03	−0.05
- Sputnik Planitia	0.79	−2.08	0.27	0.07	−0.17	−2.06	−2.05
- East Plains	1.29	−0.05	0.75	0.55	−0.21	0.005	0.22
- West Plains	2.51	0.10	0.71	0.51	0.19	0.06	−0.15
- Glacial Highlands	0.31	0.72	0.89	0.78	−0.34	0.82	0.88
- Bladed Terrain	0.26	2.45	1.17	1.38	−0.51	2.65	3.07

All values in 10^6 km^2 or km. Glacial Highlands correspond to eastern Tombaugh Regio adjacent to Sputnik Planitia.

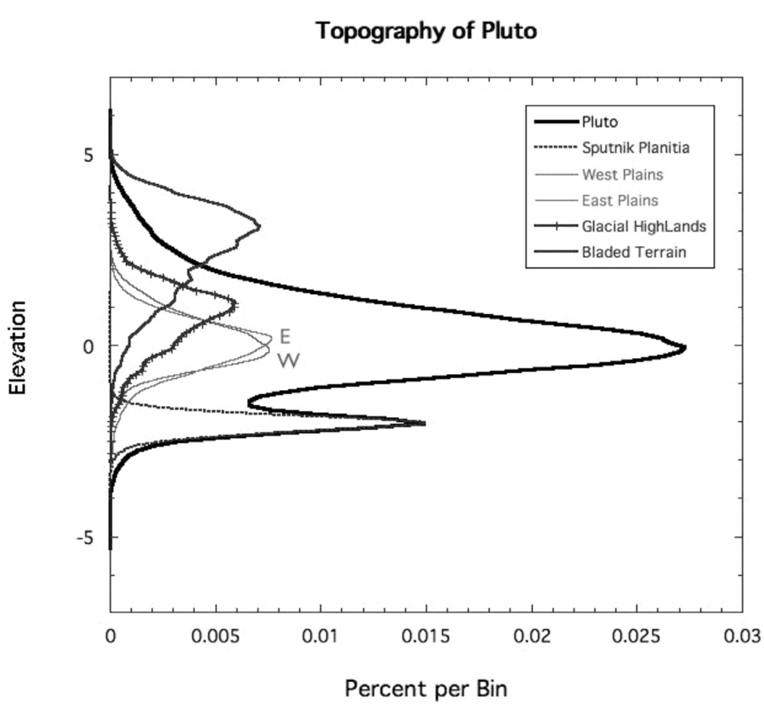

Fig. 33. Hypsogram of topography on Pluto, as measured for ∼45% of the total surface based on integrated DEM shown in Fig 6. Secondary peak at − 2 km is dominated by the depressed terrains of the Sputnik Planitia. We note that the relative elevations of Sputnik Planitia relative to the mean surface reported here is provisional pending ongoing evaluation of the geodetic figure of Pluto.

similar despite their different geologic histories (the western plains dominated by moderate cratering, the eastern by irregular walled depressions and channel scouring as discussed above). Subtle differences in the shapes of the hypsograms may reflect these differences but general similarity in topography suggest that these two plains units evolved from similar initial states. The glaciated terrains of eastern Tombaugh Regio adjacent to southeastern SP are distinctly different and have a mean elevation of ~0.72 km above Pluto mean (Fig. 33; Table 4), with some features as high as 2 km and as low as − 1 km. Whether the slightly asymmetric shape of the hypsogram could betray the effects of glacial scouring of higher elevations is an open question.

The highest terrains on Pluto, as a class, are the "bladed terrains" best exposed near 7°, 232° E at Tartarus Dorsa (Fig. 14). The Tartarus Dorsa have a mean elevation of ~2.5 km but crest at 4-to-5 km above adjacent moderately cratered plains units. Confirmed exposures of bladed terrains (Moore et al., 2018) are restricted to the equatorial band between − 20° and 25° latitude, and 220 to 250°E longitude. Their global extent is unknown but additional outcrops are suspected elsewhere along this equatorial band based on color signatures and isolated limb profiles in the low-resolution mapping areas (Moore et al., 2018). Bladed terrains are conspicuously absent within the equatorial Cthulhu Macula dark feature, which stretches from 15° to 165° longitude (Fig. 6). Though a major topographic and geologic feature, even if the putative exposures of bladed terrains are included, these units do not dominate the global topographic signature of Pluto due to their relatively small surface area. The hypsogram of bladed terrains has a significant skew towards lower elevations, related to both the arched profiles of the terrain units and the inclusion of isolated outliers of low plains in the sampling area.

It is likely that the strength of the SP-basin-related peak at − 2.0 km in the hypsogram (Fig. 3) is overemphasized by the incomplete distribution of DEM data and would be smaller if global data were available. No other large circular depressions except 250-km-wide Burney occur within the DEM coverage area (Fig. 6). The global base map, even at the lower resolutions on the approach hemisphere (Figs. 1 and 2), reveals no large bright deposits similar to Sputnik Planitia within the illuminated areas of Pluto. We provisionally infer from this that no large depressions similar in scale to SP occur elsewhere in the illuminated areas, at least within the latitudinal band within which the SP basin occurs where similar bright deposits would likely form (Binzel et al., 2017; Bertrand et al., 2018; Forget et al., 2017). Nonetheless, the SP topographic basin covers ~1,120,000 km^2, or ~6.3% of the total surface, representing a significant fraction of the topographic signature of Pluto.

The total range in relief observed on Pluto is ~11 km from highest peak to lowest depression (for well-resolved features). The highest elevations with respect to the mean Pluto radius are associated with two large areas: bladed terrains as described above, and the 2–4 km high partially eroded plateau forming the southernmost observed portions of the north-south ridge-trough system. The highest individual geologic features are the conical or blocky mountains (Figs. 3, 8, 9 and 29) that form clusters or ranges along the western margins of Sputnik Planitia (e.g., Moore et al., 2016). Chief among these are, from north-to-south, the Al-Idrisi, Zheng He, Hillary and Tenzing Montes ranges (e.g., Fig. 9). The highest individual mountains rise as high as ~5.5 to ~6.2 km above their local base (Table 3). Collectively, these isolated massifs cover no more than a few percent of the observed surface and do not contribute significantly to the global signature. Nor are they the highest in absolute elevation as their bases within the SP depression are usually well below the mean Pluto surface. Additional positive relief features include two irregular massifs of unknown origin that are part of the polar northern extension of the great north-south ridge-trough system (Fig. 15), located near 66°, 159° E, and at 80°, 283° E. Relief across these features from massif peaks to trough floor is ~4 km. Separately, the northern rim of Piccard Mons rises ~5.5 km above local terrains, with a circular center depression ~5.5 km deep for a total relief of ~11 km. These structures, as well as the isolated massif on the northwest margin of Hyecho Palus (Table 2; Fig. 29), have the greatest local relief at small scales on the mapped portions of the planet.

Despite their great height and steep slopes, some of which is unseen below the surface of the ice sheet, the massifs along western Sputnik Planitia are not quite the highest features in terms of absolute elevation as their apparent bases are typically 2–3 km below the mean radius. With the close second of the massif on the northwest margin of Hyecho Palus, which stands ~4.75 km high as the highest individual mountain relative to mean surface (Fig. 29), the distinction of the highest standing surfaces remains with the plateaus of Tartarus Dorsa (Fig. 14).

The deepest terrains on Pluto occur in three areas. The trough immediately west of the arcuate band of massifs of which al-Idrisi Montes are a part, and which form the northwestern margin of SP (Fig. 18), is uniformly ~3.5 km deep relative to the best mean Pluto radius, locally reaching − 3.8 km in some spots. The western portions of Hyecho Palus associated with Wright Mons have similar low elevations, as does the surface of the SP ice sheet at its southern most exposure near − 21°, 185° E (Fig. 20). Whether any of these 3 locations is technically lower than the others is currently within the uncertainty of measurement. The low areas along the western and southern margins of SP are also possibly original or remnant surfaces of the original topographic depression that are not currently (and may never have been) covered by the nitrogen-methane-CO ice sheet of SP. The floor of a 42–km-wide crater at 10°, 155° E reaches − 4 km, and the floor to rim depth in the center of Piccard Mons (Fig. 31) reaches down to approximately 4 ± 1.0 km below mean radius, and these may be the deepest single features known on Pluto.

Finally, the significant local relief on Pluto is telling. Moore et al. (2016) and Grundy et al. (2016) inferred from the heights of the mountains that the outer shell of Pluto is likely dominated by a rheologically stiff material most likely water ice. The 4–6 km high mountains along western Sputnik Planitia, the 4–8 km high annular massifs Wright and Piccard Mons, and the preservation of the recent 2–3 km deep trough walls in the western plains (Fig. 10; and vertical displacements of up to 1.4 km across them) all confirm that the icy shell of Pluto is relatively stiff and able to support vertical loads locally of substantial magnitude (~ < 1 MPa). Similarly, the relief present on Pluto, including the deep relief across Sputnik Planitia as well as across structures such as Virgil Fossae, suggests that Pluto also has not experienced a major heat pulse sufficient to erase these large-scale features, and that weak ices such as nitrogen or methane do not dominate the deeper layers sufficiently to weaken them. These observations and the indications of water ice spectral signatures along the walls of Virgil Fossae (Grundy et al., 2016; Cook et al., 2018) confirm that water ice is likely the dominant crustal material across most of Pluto (Moore et al., 2016; Grundy et al., 2016).

Despite the locally high relief observed, 68% (or 1 standard deviation) of Pluto's topography lies within ~1.3 km of the mean surface. Most of these terrains within the main hypsogram peak are characterized by erosional or impact related processes, as documented by Howard et al. (2017b), White et al. (2017) and others. On the Earth and Titan similar hypsograms may reveal the action of regional and local geological processes such as glacial erosion (see Lorenz et al., 2013); whether such processes can be inferred from the Pluto hypsogram is a question for future work. The "global" hypsogram of Titan is even narrower than on Pluto, with a standard deviation (~68% RMS) of ~0.25 km, which is comparable to the smaller Sputnik Planitia ice sheet. The lack of deep topography on Titan certainly reflects the paucity of large impact craters, but how much the interpolation of the Titan data set affects such statistical representations is not yet clear. We lack global topographic data for the large icy Galilean satellites but limb profiles (Nimmo et al., 2007) and unpublished data from Schenk (2014) and Schenk et al. (2014) indicate that essentially all the topographic data from individual mapping sites covering 10–20% of Europa and Ganymede fall within ± 1 km of the local mean surfaces, suggesting that the hypsograms of these two bodies are likely to be similarly narrow. Topographic data for Triton is similarly limited but limb profiles (Thomas, 2000) and unpublished stereogrammetry DEMs all indicate relief within ± 1 km of the global mean for the equatorial terrains we have coverage.

Most physical processes influencing topography depend on wavelength: for instance, both elastic support and viscous relaxation are strongly wavelength-dependent. Because hypsograms do not include any wavelength information, interpreting them is not straightforward. In addition, Triton, Europa and Titan all lack large impact basins, further complicating comparison with Pluto. Nonetheless, the apparently unrelaxed basin Sputnik Planitia strongly suggests that Pluto's shell is capable of supporting large stresses, at least locally, and was probably thick and cold when Sputnik Planitia formed (Kamata and Nimmo, 2014). Conversely, the low amplitude of topography on the widespread plains units outside Sputnik Planitia likely reflect either an absence of large, disruptive impact or tectonic events, and/or efficient resurfacing such as might have occurred via pervasive volcanism, erosion or elevated heat flow in the distant past.

5.2. Occultation radii measurements of Pluto

The only independent non-image-based measurement of topography currently available for Pluto is from the radio occultation observations obtained at two antipodal points on the surface (Hinson et al., 2017). The first point, at − 17°, 193.5°E, occurs on the southeastern margin of the Sputnik Planitia topographic basin, which Hinson et al. (2017) estimate at 1186.5 km, the second in poorly resolved terrains at 15°, 15.7°E, at an elevation of 1192.4 km, or a difference of 5.9 km. Direct comparison between these values and the DEM requires detailed analysis that is not a priority for this work, but some basic comparisons can be made. The footprint of the radio occultation measurements is given to first order by 2(2*1188.3*h)^0.5, where h is the variability in topography in the footprint. For reasonable values of h, the footprints are likely to be 130–150 km long. For the first point (Fig. 34), we estimate the elevation to be ~1187.0, within half a kilometer of the radio result. We caution, however, that the two data sets are not necessarily tied to the same center of figure; the relative difference in elevation of the two points is more relevant. We do not have any stereo topography near point 2, but this region is inferred from geology and color mapping (e.g., Moore et al., 2018) to be in the northern section of a large patch of bladed terrain, which are plateaus elevated 2–5 km above surrounding

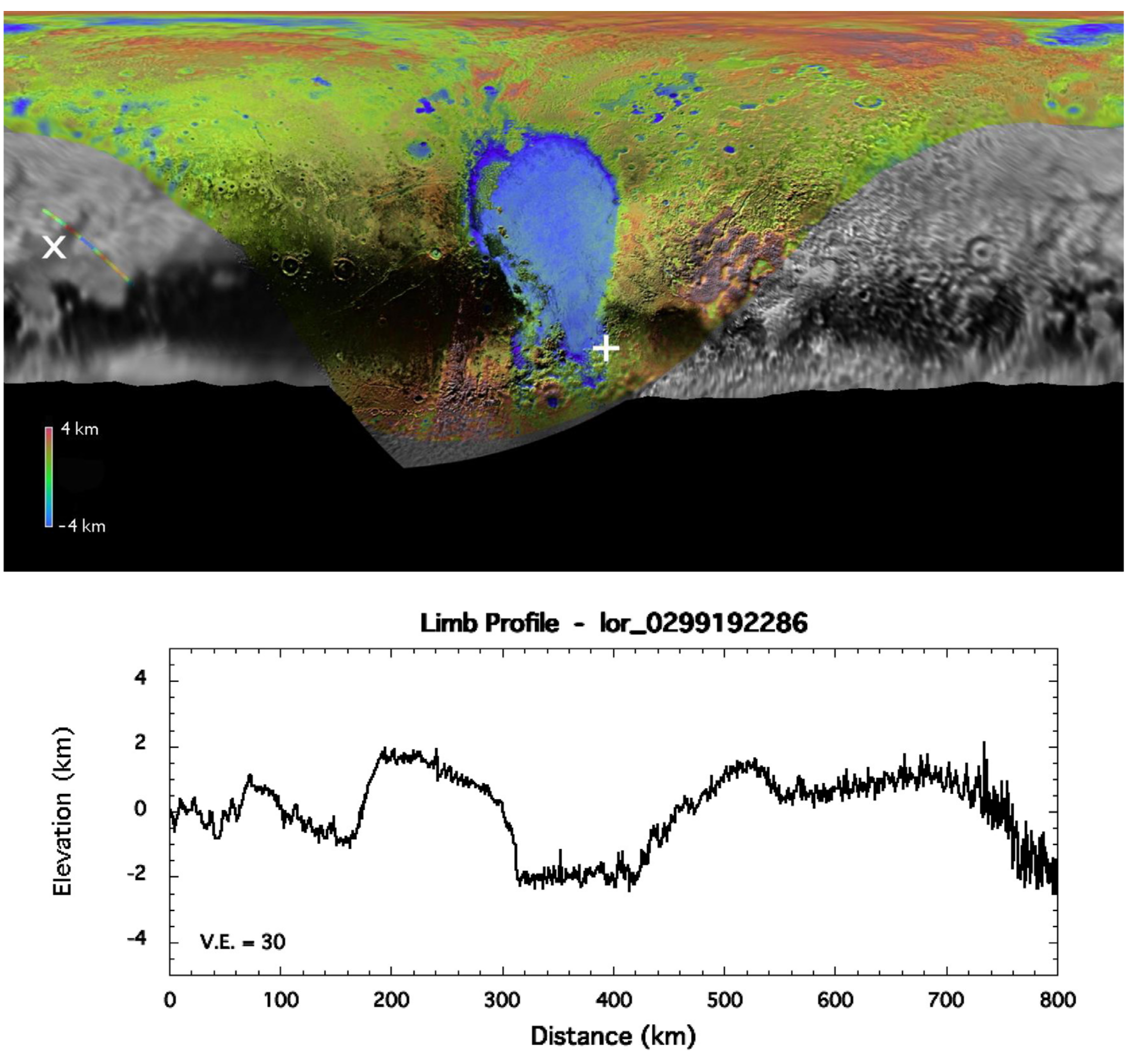

Fig. 34. (a) Global DEM of Pluto highlighting the locations of the two occultation points (Hinson et al., 2017), and a topographic profile nearby. " + " is the entry point, "X" is the egress point. Adjacent to the X is shown a limb profile trace indicating that the irregular grey patch on which the X sits is elevated several kilometer, confirming that the egress point is elevated. The color version shows the color-coded DEM merged with the global base map. (b) Topographic profile from limb observation in LORRI frame 0,299,192,286, highlighting several 4-km-high plateaus similar to the plateaus of bladed terrain. Profile trace is shown in a. See text for discussion.

terrains in resolved data. We take the mapped area of bladed terrain southeast of Sputnik Planitia as a proxy for the second occultation point. We find 'mean' elevation values between 2.5 and 3.2 km, depending on how and where the terrain is sampled (Fig. 34; Table 4). If we assume that higher terrains in the footprint will influence the radio results more than the lower terrains, due to the severe projection effects on the limb, we get a minimum elevation difference of ∼4.5 km between the two occultation points. This is consistent with the radio occultation results, given the lack of direct measurements in the DEM at point 2, and the high degree of relief likely at both points. This conclusion is confirmed by a single limb profile track very close to the egress point, which, although not yet tied to the center of figure, shows that the irregular greyish patch on which the egress point occurs is indeed high standing by 3–4 km (Fig. 34).

5.3. Origins of the major topographic features of Pluto

Stratigraphically, the flat lying though cratered and pitted plains west and east of Sputnik Planitia appear oldest, followed by the formation of the giant SP basin itself, all of which are partially eroded to varying degrees. The great circle north-south ridge-trough system along the western edge of the SP basin is also very ancient, based on its similar history of erosion. The ice sheet within SP clearly post-dates the ridge-trough system, but the age of this global-scale great circle tectonic system with respect to the putative SP impact formation event is less clear. Some of the troughs can be clearly defined up to the edge of the ice sheet, suggesting that the impact event occurred first, followed by fracturing. Of course, the fracture system could have been in place before the large impact, and tectonic deformation continued afterward. The formation of massifs along the western margins of SP but not the eastern side (e.g., Fig. 9) is curious but may be related to the occurrence of the North-South ridge-trough system also along the western margins. If SP is a giant impact, as seems likely (e.g., Moore et al., 2016), the trough system may have been a zone of weakness, leading to the breakup of large blocks preferentially on this side during the impact event. If so, then the trough system predates the formation of SP, with additional post-impact strain reflected in the features that cross the elevated rim.

The 600-km-wide 2-km-high polar dome (Fig. 15) is also deeply eroded and could predate the trough system (although post-fracturing domal uplift followed by deep erosion of the newly elevated terrains is also allowed). While the mass anomaly of SP basin dominants Pluto and likely induced its current geographic orientation (e.g., McKinnon et al., 2016; Keane et al., 2016), the location of the dome at one of the current poles (the other was in darkness) is provocative and suggests thickening of the crust, or some form of internal mass redistribution in response to polar conditions. If the dome is a positive mass anomaly, one might expect polar wander to move the dome to the equator, which is not observed, but if dome material is under dense (as in an atmospheric deposit) it could be a negative mass anomaly and movement to the current rotational pole would be plausible. On average, the poles receive more solar insolation due to Pluto's high obliquity (e.g., Binzel et al., 2017; Bertrand et al., 2018; Forget et al., 2017; Earle et al., 2018) but are brighter and it is not clear whether the poles are cold, which could produce a thickening of the polar ice shell (e.g., Ojakangas and Stevenson, 1989). Subsurface laccolithic intrusion, an ancient shield volcano, or dynamic uplift over internal upwellings is possible though not necessarily plausible mechanisms for producing a large dome on Pluto. As only one dome is observed, testing hypotheses is more difficult. More plausible is that this eroded dome represents the remains of an accumulation of ices at this pole. The morphology of the dome surface is both striated and smooth, which could be consistent with a deposit of less consolidated material. The moderate degree of cratering on the dome suggests it is rather old, but why this feature should have stayed in a polar location if polar wander occurred (McKinnon et al., 2016; Keane et al., 2016) is unclear unless shell rotation was fixed about the current axis. Whatever its origins, the formation of this dome potentially places important constraints on Pluto's evolution.

Moore et al. (2016) suggested that Wright and Piccard Mons are possible volcanic edifices, involving extrusion of ice phases onto the surface. In addition to the very low crater counts across all of Hyecho Palus (Singer et al., 2016; Robbins et al., 2017), requiring recent resurfacing, the global map and topography data support this interpretation. Numerous small fractures and small domes are scattered across the floor of Hyecho Palus (Fig. 32). The depressed plains of Hyecho Palus of which Wright and Piccard Montes are major features are essentially crater free (Singer et al., 2016), as are the elevated plateaus of bladed terrains, consistent with the interpretation of geologically recent resurfacing in these areas (Stern et al., 2015; Moore et al., 2016).

Evidence for discrete volcanic flow on the Hyecho Palus plains is cryptic. The surfaces of these large edifices and large areas of the surrounding depressed plain are characterized by innumerable overlapping and abutting smaller mounds 5–10 km across (Fig. 31), a morphology with few if any direct analogs on planetary surfaces. The apparent uniformity of the sizes of these abutting mounds is also remarkable. The surfaces of these mounds are rugged, with numerous smaller knobs ∼1-km-across covering their crests. One possible interpretation of these morphologies is construction by extrusion and accumulation of numerous smaller extrusions of viscous icy material, followed by central vent collapse, mass wasting, or perhaps differential outward flow due to volume restrictions at the point sources of Wright and Piccard Mons. The innumerable overlapping 10–15 km wide knobs forming the bulk of Wright Mons bring to mind overlapping viscous domes usually associated with dacite and andesite composite volcanism on Earth. Examples include late stage coalescing dome formation on Mt. St. Helens (e.g., Swanson et al., 1987), Soufriere (e.g., Roobol and Smith, 1998), and the well-studied resurgent domes across Valles Caldera (e.g., Heiken, et al., 1990). The terrestrial domes are typically on the order of 1–5 km across and up to 1 km high, and usually topographically confined within a walled caldera, which may be analogous to the formation of these mounds within Hyecho Palus. The exact mechanism is unlikely to be identical but the extrusion and overlap of numerous viscous domes could explain the mounded textures of these terrains. These features require detailed mapping and are explored in other works (e.g., Moore et al., 2016; Singer et al., 2016).

One of the biggest surprises from the topographic map of Pluto is the discovery of a great circle ridge-trough system spanning the observed elevation map (Fig. 25). Global-scale great circle tectonic systems are unusual in planetary environments. In planform, if not morphologically, the hoop-like ridge-trough system on Pluto most resembles Ithaca Chasma on Tethys and the equatorial Divalia Fossae troughs on Vesta. Ithaca Chasma extends as a well-defined trough comprised of sub-parallel well-preserved fault scarps around 3/4 of Tethys' circumference (Giese et al., 2007; Schenk et al., 2018b). Divalia Fossae form a broadly similar parallel deep graben system formed nearly circumferential to the 500-km-wide Rheasilvia megabasin on Vesta (e.g. Buczkowski et al., 2012). The Pluto system is significantly eroded and variable in relief with prominent depressed and elevated sections, whereas the Tethys and Vesta troughs are mostly deep double-walled structures and are well preserved. The Vesta trough system likely formed in response to the passage of seismic shocks through the oblate body of Vesta (Ivanov and Melosh, 2013; Bowling et al., 2013), but the origin of Ithaca Chasma is still debated. It may be a relict of global expansion (Moore and Ahern, 1983) but Moore and Ahern and Schenk et al. (2018b) also suggest it formed as a giant extensional fault system triggered by the large 400-km-wide Odysseus impact event to which it is nearly circumferential. Although topographic and morphologic mapping of Pluto not yet complete, sufficient resolution was obtained to determine that no large impact features occur at either of the two poles of the great circle forming the ridge-trough system (Fig. 25), suggesting that a large impact is not the likely cause of their formation.

The ridge-trough system is currently oriented nearly 90° to the equator, but reorientation of Pluto via true polar wander has been suggested as a result of the mass anomaly associated with the SP depression (Nimmo et al., 2016; Keane et al., 2016). The much younger fracture systems flanking SP (Figs. 10 and 12), have been associated with putative reorientation stresses (Nimmo et al., 2016; Keane et al., 2016), and thus the older ridge-trough system (and many of Pluto's features) could have originally formed in a different orientation, including possibly along the paleoequator. The elevated Tartarus Dorsa plateaus are located very near the pole to the great circle formed by the ridge-trough system (Fig. 33), suggesting they could be polar deposits now moved to the equator, though there are no such deposits at the other pole (located in the center of Cthulhu Macula) and the location of Tartarus Dorsa at the paleopole of the ridge-trough system may be a coincidence.

The stratigraphic sequence of the large basin and trough system is ambiguous. The persistence of the system up to the edge of the SP ice sheet and the lack of any preferred orientation relative to it suggest that the ridge-trough system postdate the SP basin, but a scenario in which the system predates the PS basin but activity continued after basin formation is not ruled out. Such a large impact could have launched considerable debris into circum-Pluto space, some of which could have reaccreted onto Pluto's equatorial regions after impact. The system could thus be a highly evolved Plutonian analog to the ring-reaccretion origin for the great-circle Iapetus ridge (Ip, 2006). If formed before SP, however, then the ridge-trough system could have formed in this way only if related to reaccretion of debris from the Pluto-Charon giant impact event. Whether the dynamic conditions following the Charon-forming impact can explain the observed morphologies is unclear. Some of the elongate depressions along its length could be related to formation in this way, such as low-angle impacts of large fragments.

An endogenic origin of the ridge-trough system is probably more likely. Internal heating or cooling could induce lithospheric stresses, though the system appears to contain both extensional and compressional elements. Typically, however, these stresses do not form a single great circle structure but rather form distributed failure patterns throughout the lithosphere (i.e., Collins et al., 2010). Additional related structures of similar age are not observed on Pluto, and an endogenic mechanism to focus stresses in such a narrow region is not obvious. Further, we conjecture that the gigantic SP basin structure would locally focus stresses in a radial or concentric fashion, but the tectonic system appears to be not influenced by its proximity to the basin, again arguing for formation before the SP depression. Thus the origin of this complex global tectonic feature remains cryptic.

An additional clue to the origin of the ridge-trough system is the differing topographic and morphologic characteristics of the moderately cratered plains to the west and east of the north-south trough system (Fig. 25). To the west the plains are relatively flat and undisturbed except for random craters and a few late-stage graben (Fig. 10); to the east they are more deeply pitted or glacially eroded (Figs. 11 and 12). Why an ancient global tectonic system should serve as a boundary between two major terrain types is unknown, but it suggests that either the composition or erosional history of the two terrains has been different or the ridge-trough system forms on structural boundary between them. If Pluto has undergone polar wander (e.g., Keane et al., 2016), then none of these terrains are in their original locations, which should be considered in evaluating their origins.

The topographic surface of the Sputnik Planitia ice sheet is essentially flat within the limits of the current topographic map (though additional work remains to be done (Schenk et al., 2018c). The surface of the ice sheet changes character with latitude, transitioning toward the north from having a modest raised edge along the rugged rim of a few hundred meters to having a depressed marginal moat of similar magnitude. The transition happens at roughly 25° latitude on the eastern side (the raised margins corresponding to the area of contact with the high albedo eastern Tombaugh Regio glaciated areas), but at roughly 10–12° on the western side where active glaciation is less pronounced (though its past effects are still in evidence as gullies and scouring). These patterns are consistent with climatic models (e.g., Bertrand et al., 2018; Forget et al., 2017; Earle et al., 2018) indicating preferred deposition in the central and southern sections and erosion in the northern section of Sputnik Planitia.

Similarly, the arched rim of the SP basin also changes character depending on location and the nature of the adjacent terrains. To the northeast the rim is deeply scoured by innumerable gullies, presumably of glacial origin. The southeast rim is cut by numerous glacier-like flows emanating from the glaciate highlands of eastern Tombaugh Regio. The western edge of the SP ice sheet is also the site of some of the deepest relief on Pluto, locally as much as 3.5 km. The deepest parts appear to lack the smooth ices seen in the main ice sheet, and lateral flow of the ice sheet may have been inhibited here by the numerous and closely spaced angular massifs that make up the mountain ranges of western Sputnik Planitia.

Another important insight from the global reflectance, color and topographic mapping of Pluto (Figs. 1–3) is that the colors and albedo of Pluto are controlled by elevation in many area but that there are exceptions. For example, the crests of high mountain ranges at York and Enrique Montes (Figs. 26 and 27) are covered by bright methane ices or frosts, as are the upper elevations of the north polar dome (Fig. 15). On the other hand, the dark equatorial band between ~16° and − 20° latitude and evident in the global mosaic (Fig. 1) has a complex relationship to topography. The best resolved section of this feature is the elongate Cthulhu Macula feature, observed at 315 m pixel scales and in color and stereo. The northern boundary of this dark equatorial band is diffuse and does not correlate with any major change in surface morphology or topography (Figs. 1 and 10), consistent with control of albedo by latitude (e.g., Bertrand et al., 2018; Forget et al., 2017; Binzel et al., 2017). This wide equatorial dark band is sharply bounded on its eastern extremity by the depressed Sputnik Planitia bright plains, and on its western extremity (at ~30° longitude) by irregularly shaped brighter deposits inferred to be bladed terrain units elevated several kilometers (e.g., Moore et al., 2018), all indicating control by topography. East of Sputnik Planitia, where we would expect a continuation of the dark equatorial band, we observe dark material between − 20° and − 5° latitude but north of − 5° latitude the bright glaciated plains of eastern Tombaugh Regio which are elevated ~750 m above the plains units and the elevated plateaus of Tartarus Dorsa, again indicating topographic control of the dark surficial deposits. Thus, the dark equatorial deposits are primarily related to latitude on a global scale but within this band are restricted in their formation to a relatively narrow elevation range locally by both depressed and elevated features, giving the interrupted albedo pattern we observe today (Fig. 1). Pluto's dark equatorial band would likely be continuous in nature and driven mostly by latitudinally controlled processes such as solar insolation (e.g., Protopapa et al., 2017; Schmitt et al., 2017), if it were not interrupted in several locations by changes in elevation and ice deposition.

The first reconnaissance of a large Kuiper–Edgeworth Belt object and of a large icy body in solar orbit not formed under the influence of a large primary body is now complete. The morphology and topography of Pluto is complex and can be divided into provinces of distinctive characteristics, the origins of which are only partly understood. The ancient basin-forming event at Sputnik Planitia dominates Pluto topographically and has likely influenced its subsequent history, including the formation of a volatile ice sheet in the floor of the basin and later polar wander. A globe-circling tectonic feature both marks a dichotomy in the surface characteristics of Pluto and a major tectonic episode of unknown origins. Further, color and reflectance are variable with both latitude and with altitude. The annular massifs of Wright and Piccard Mons as well as the depressed plain in which they form represent a significant episode of resurfacing late in Pluto's history. These new maps provide important constraints on Pluto's history that will require years to unravel and suggest that exploration of other large icy bodies that populate the Kuiper-Edgeworth Belt may reveal similarly complex bodies as well.

Acknowledgments

We thank Brian Fessler and the IT staff at the Lunar and Planetary Institute, Houston, for their programing and computer support in deriving these maps. We also thank the New Horizons navigation, sequencing, and science teams for their spectacularly successful design and execution of these challenging observations. This work was supported by NASA's New Horizons project.

Supplementary materials

Supplementary material associated with this article can be found, in the online version, at doi:10.1016/j.icarus.2018.06.008.

References

Archival, B., 2011a. Report of the IAU working group on cartographic coordinates and rotational elements: 2009. Celest. Mech. Dynam. Astros. 109, 101–135.
Archival, B., 2011b. Erratum to: Report of the IAU working group on cartographic coordinates and rotational elements: 2006 & 2009. Cel. Mech. Dyn. Ast. 109, 401–403.
Barnett, D., Nimmo, F., 2002. Strength of faults on Mars from MOLA topography. Icarus 157, 34–42.
Bertrand, T., et al., 2018. The nitrogen cycles on Pluto over astronomical timescales. Icarus 309, 277–296.
Beyer, R.A., Schenk, P., Moore, J., 2013. The ninth planet's third dimension. In: Proceedings of Pluto Workshop. JHU Applied Physics Lab, Laurel, MD.
Binzel, R., et al., 2017. Climate zones on Pluto and Charon. Icarus 287, 30–36.
Bowling, T., Johnson, B., Melosh, H.J., 2013. Formation of equatorial graben following the rheasilvia impact on asteroid 4 vesta. In: Proceedings of the 44th Lunar and Planetary Science Conference, abstr. 1719.
Brown, C.D., Phillips, R.J., 1999. Flexural rift flank uplift at the Rio Grande rift, New Mexico. Tectonics 18, 1275–1291.
Buczkowski, D.L., et al., 2012. Large-scale troughs on Vesta: a signature of planetary tectonics. *Geophys. Res. Lett.* 39, L18205. http://dx.doi.org/10.1029/2012GL052959.
Buratti, B., et al., 2017Buratti. Gloable albedos of Pluto and Charon from LORRI New Horizons observations. Icarus 287, 207–217.
Cheng, A.F., et al., 2008. Long-range reconnaissance imager on New Horizons. Space Sci. Rev. 140, 189–215. http://dx.doi.org/10.1007/s11214-007-9271-6.
Collins, G., McKinnon, W., Moore, J., Nimmo, F., Pappalardo, R., et al., 2010. Tectonics of the outer planet satellites. In: Schultz, R.A., Watters, T.R. (Eds.), Planetary Tectonics. Cambridge University Press, Cambridge, pp. 264–350.
Cook, A., Oberst, J., Roatsch, T., Jaumann, R., Acton, C., 1996. Clementine imagery: selenographic coverage for cartographic and scientific use. Planet. Space Sci. 44, 1135–1148.
Cook, J., et al., 2018. The distribution of H_2O, CH_3OH, and hydrocarbon-ices on Pluto: analysis of New Horizons spectral images. Icarus (Submitted for publication).
Earle, A.M., et al., 2018. Albedo matters: Understanding runaway albedo variations on Pluto. Icarus 303, 1–9.
Forget, F., Bertrand, T., Vangvichith, M., Leconte, J., Millour, E., Lellouch, E., 2017. A poist-New Horizons global climate model of Pluto including the N_2, CH_4 and CO cycles. Icarus 287, 54–71.
Grundy, W.M., et al., 2016. Surface compositions across Pluto and Charon. Science 351, 1283.
Giese, B., Wagner, R., Neukum, G., Helfenstein, P., Thomas, P.C., 2007. Tethys: lithospheric thickness and heat flux from flexurally supported topography at Ithaca Chasma. Geophys. Res. Lett. 34, L21203. http://dx.doi.org/10.1029/2007GL031467.
Heiken, G., et al., 1990. The valles/toledo caldera complex, jemez volcanic field, New Mexico. Annu. Rev. Earth Planet Sci. 18, 27–53 1990.
Hinson, D., et al., 2017. Radio occultation measurements of Pluto's neutral atmosphere with New Horizons. Icarus 290 (0), 96–111.
Howard, A., et al., 2017a. Present and past glaciation on Pluto. Icarus 287, 287–300.
Howard, A., et al., 2017b. Pluto: pits and mantles on uplands north and east of Sputnik Planitia. Icarus 293, 218–230.
Ip, W.-H., 2006. On a ring origin of the equatorial ridge of Iapetus. Geophys. Res. Lett. 33, L16203. http://dx.doi.org/10.1029/2005GL025386.
Ivanov, B.A., Melosh, H.J., 2013. Two-dimensional numerical modeling of the Rheasilvia impact formation. J. Geophys. Res. Planets 118. http://dx.doi.org/10.1002/jgre.20108.
Kamata, S., Nimmo, F., 2014. Impact basin relaxation as a probe for the thermal history of Pluto. J. Geophys. Res. 119. http://dx.doi.org/10.1002/2014JE004679.
Keane, J., Matsuyama, I., Kamata, S., Steckloff, J., 2016. Reorientation and faulting of Pluto due to volatile loading within Sputnik Planitia. Nature 540, 90–93.
Lorenz, R., 10 others, 2013. A global topographic map of Titan. Icarus 225, 367–377.
Lucy, L.B., 1974. An iterative technique for the rectification of observed distributions. Astron. J. 79, 745. http://dx.doi.org/10.1086/111605.
McEwen, A., Soderblom, L., 1984. Pixels, not pictures: imaging of Io. Planet. Rep. 4 (1).
McEwen, A., 1991. Photometric functions for Photoclinometry and other applications. Icarus 92, 298–311.
McKinnon, W.B., 1984. On the origin of Triton and Pluto. Nature 311, 355–358.
McKinnon, W.B., et al., 2016. Convection in a volatile nitrogen-ice-rich layer drives Pluto's geological vigour. Nature 534, 82–85.
Moore, J., Ahern, M., 1983. Geomorphology of Tethys. J. Geophys. Res. 83, A577–A584.
Moore, J.M., et al., 2016. The geology of Pluto and Charon through the eyes of New Horizons. Science 351, 1284–1293. http://dx.doi.org/10.1126/science.aad7055. aad7055.
Moore, J., et al., 2017. Sublimation as a landform-shaping process on Pluto. Icarus 287, 320–333.
Moore, J., et al., 2018. Bladed terrain on Pluto: possible origins and evolution. Icarus 300, 129–144.
Nimmo, F., et al., 2007. The global shape of Europa: constraints on lateral shell thickness variations. Icarus 191, 183–192.
Nimmo, F., Hamilton, D., McKinnon, W., Schenk, P., Binzel, R., et al., 2016. Reorientation of Sputnik Planitia implies a subsurface ocean on Pluto. Nature 540, 94–96.
Nimmo, F., et al., 2017. Mean radius and shape of Pluto and Charon from New Horizons images. Icaru 287, 12–29.
Ojakangas, G., Stevenson, D., 1989. Thermal state of in ice shell on Europa. Icarus 81, 220–241.
Protopapa, S., et al., 2017. Pluto's global surface composition through pixel-by-pixel Hapke modeling of New Horizons Ralph/LEISA data. Icarus 287, 218–228.
Preusker, F., et al., 2016. Dawn at ceres – shape model and rotational state. In: Proceedings of the 47th Lunar and Planetary Science Conference, abstr. 1903.
Reuter, D.C., et al., 2008. Ralph: a visible/infrared imager for the New Horizons Pluto/Kuiper belt mission. Space Sci. Rev. 140, 129–154. http://dx.doi.org/10.1007/s11214-008-9375-7.
Richardson, W.H., 1972. Bayesian-based iterative method of image restoration. J. Opt. Soc. Am. 62, 55–59.
Robbins, S., et al., 2017. Craters of the Pluto-Charon system. Icarus 287, 187–206.
Roobol, M.J., Smith, A.L., 1998. Pyroclastic stratigraphy of the Soufriere Hills Volcano, Montserrat – implications for the present eruption. Geophys. Res. Lett. 28, 3393–3396.
Schenk, P., 2014, Mapping the Topography of Europa: The Galileo-Clipper Story, AAS, DPS meeting #46, id.418.08.
Schenk, P.M., Bulmer, M.H., 1998. Origin of mountains on Io by thrust faulting and large-scale mass movements. Science 279, 1514–1518.
Schenk, P.M., Pappalardo, R.T., 2004. Topographic variations in chaos on Europa: implications for diapiric formation. Geophys. Res. Lett. 31, L16703.
Schenk, P., 2009. Slope characteristics of Europa: constraints for landers and radar sounding. Geophys. Res. Lett. 36 CiteID L15204.
Schenk, P., McKinnon, W., 2009. One-hundred-km-scale basins on Enceladus: evidence for an active ice shell. Geophys. Res. Lett. 36 CiteID L16202.
Schenk, P., McKinnon, W.B., Singer, K.N., Moore, J.M., 2014. Current State of Topographic Mapping of Ganymede: Squeezing the Most from JUICE, EOS, abstract #P34C-01.
Schenk, P., et al., 2018a. Canyons, craters and volcanism: global cartography and topography of charon from New Horizons. Icarus (In press).
Schenk, P., White, O., Byrne, P., Moore, J., 2018b. Saturn's other icy moons: geologically complex worlds in their own right. Enceladus and the Icy Moons of Saturn. University of Arizona Press In press.
Schenk, P., et al., 2018c. High-resolution topography of Pluto and Charon: getting down to details. In: Proceedings of the 49th Lunar and Planetary Science Conference, abstr. 2300.
Schmidt, B., Blankenship, D., Patterson, G., Schenk, P., 2011. Active formation of 'chaos terrain' over shallow subsurface water on Europa. Nature 479, 502–505.
Schmitt, B., et al., 2017. Physical state and distribution of materials at the surface of Pluto from New Horizons LEISA imaging spectrometer. Icarus 287, 229–260.
Singer, K., et al., 2016. Pluto's putative cryovolcanic constructs. In: Proceedings of Planetary Mappers Meeting, 1920, #7017.
Singe, K., et al., 2017. Chaotic mountain blocks in Pluto's sputnik planitia. In: Proceedings of the 49th AAS/DPS Meeting Abstract, id221.01, iposter url: https://bit.ly/2Fdj1M6.
Singer, K., et al., 2018. Impact craters on Pluto and Charon and Evidence for a Deficit of small Kuiper Belt Objects, (Submitted for publication).
Stern, S.A., et al., 2015. The Pluto system: Initial results from its exploration by New Horizons. Science 350http://dx.doi.org/10.1126/science.aad1815. aad1815.
Swanson, D., et al., 1987. Growth of the lava Dome at Mt. St. Helens, Washington (USA), 1981–1983. The Emplacement of Silicic Domes and Lava Flows. Geological Society of America GSA Special Paper 212.
Thomas, P., 2000. The shape of Triton from limb profiles. Icarus 148, 587–588.
U.S. Geological Survey, 2017. Integrated Software for Imagers and Spectrometers (ISIS). http://isis.astrogeology.usgs.gov.
Weaver, H.A., Gibson, W.C., Tapley, M.B., Young, L.A., Stern, S.A, 2008. Overview of the New Horizons science payload. Space Sci. Rev. 140, 75–91.
White, O.L., Schenk, P.M., Nimmo, F., Hoogenboom, T., 2014. A new stereo topographic map of Io: implications for geology from global to local scales. J. Geophys. Res. Planets 119, 1276–1301. http://dx.doi.org/10.1002/2013JE004591.
White, O., et al., 2017. Geological mapping of Sputnik Planitia on Pluto. Icarus 287, 261–286.
Young, L.A., et al., 2008. New horizons: anticipated scientific investigations of the Pluto system. Space Sci. Rev. 140, 93–127. http://dx.doi.org/10.1007/s11214-008-9462-9.
Young, L., et al., 2017. N2 in Pluto's Northern Lowlands. EPSC2017-139.
Zangari, A., 2015. A meta-analysis of coordinate systems and bibliography of their use on Pluto from Charon's discovery to the present day. Icarus 246, 93–145.